A Short-Range Test of Newton's Gravitational Inverse-Square Law

Daniel J. Kapner

A dissertation submitted in partial fulfillment
of the requirements for the degree of

Doctor of Philosophy

University of Washington

2005

Program Authorized to Offer Degree: Department of Physics

ProQuest Information and Learning Company
300 North Zeeb Road
P.O. Box 1346
Ann Arbor, MI 48106-1346

University of Washington
Graduate School

This is to certify that I have examined this copy of a doctoral dissertation by

Daniel J. Kapner

and have found that it is complete and satisfactory in all respects,
and that any and all revisions required by the final
examining committee have been made.

Chair of Supervisory Committee:

Eric G. Adelberger

Reading Committee:

Eric G. Adelberger

Jens H. Gundlach

Blayne R. Heckel

Date: 6/28/05

Signature

Date 6/28/05

University of Washington

Abstract

A Short-Range Test of Newton's Gravitational Inverse-Square Law

by Daniel J. Kapner

Chair of Supervisory Committee:

Professor Eric G. Adelberger
Department of Physics

Recent attempts at unifying the descriptions of gravity and quantum mechanics predict that Newton's Gravitational Inverse-Square Law will fail below some distance scale, possibly as large as 1 mm. Recent measurements of the Dark Energy content of the universe could also imply short-range modifications to gravity.

Our previous tests [1] detected no deviation from the Inverse-Square Law, set new experimental limits on possible short-range violations, and constrained a gravity-strength Yukawa interaction to have a length scale below 197 μm at the 95% confidence level. This dissertation describes an improved next-generation of those tests using a new detector and attractor, each of 21-fold azimuthal symmetry. We tested the inverse-square law at separations down to 65 μm; we can now exclude gravity-strength Yukawa interactions to have a length scale below 79 μm at the 95% confidence level. We observed an apparent deviation from the inverse-square law at the shortest separations; we do not know the origin of this anomaly, nor do we know if it is a gravitational effect. Nevertheless, if this anomaly is parameterized as an additional Yukawa potential, has a characteristic length scale below 50 μm at the 68% confidence level with strength at least 5 times that of gravity. This dissertation is a complete description of this experiment.

TABLE OF CONTENTS

LIST OF FIGURES

LIST OF TABLES

ACKNOWLEDGMENTS

I could not have done the work described here without the support of the Eöt-Wash group. Eric Adelberger, Blayne Heckel, and C.D. Hoyle spent countless hours working on this experiment, its predecessors, and its offspring. It was a pleasure to learn from their experience, patience, and creativity. I also thank Jens Gundlach, Erik Swanson, Ted Cook, Todd Wagner, Tom Butler, Matt Feig, Rogan Carr, Rob Kyle, and Chiara Losh for the many contributions they have made to this work.

I thank my parents for their constant love and support. I thank Rebecca Lavigne for her love and for her patience during the course of this work.

Chapter 1

THEORETICAL AND EXPERIMENTAL BACKGROUND

I am indebted to References [2] and [3] for covering much of this material in their extensive reviews of these topics.

1.1 Theoretical Motivations

An investigation of the Inverse-Square Law (ISL) at short distances can address a variety of interesting scenarios at the forefront of theoretical and experimental research. The combination of the Standard Model (SM) and general relativity (GR) accurately describe phenomena from sub-atomic to cosmological scales. Nonetheless, these two theories are incomplete for the same reason that there *are* two theories : the SM can not produce a renormalizable theory of gravity and GR predicts *nothing* about the complex structure of matter that we observe, only how matter and space-time interact. The two theories operate at very disparate energy scales. Elegance and simplicity drive us to search for one unified theory to explain all known phenomena with one theoretical framework; this pursuit has led to the development of "M-theory", where the traditional concept of point particles are replaced by one-dimensional vibrating strings and n-dimensional "branes". While there is, as yet, no experimental signature of M-theory - its effects are generally thought to reside at the incredibly small Planck length, $R_P = \sqrt{G\hbar/c^3} = 1.6 \times 10^{-35}$ m or the corresponding energy scale $M_P = \hbar c/R_P = 10^{19}$GeV - recent work has opened the possibility of such signatures arising in short-distance gravity. Meanwhile, measurements of the last decade of distant supernovae and the cosmic microwave background ([4][5][6]) have produced a remarkable inventory of our universe's energy content. A mere 5% of this energy is in the form of baryons, while about 25% is in the form of Dark Matter and the remaining 70%

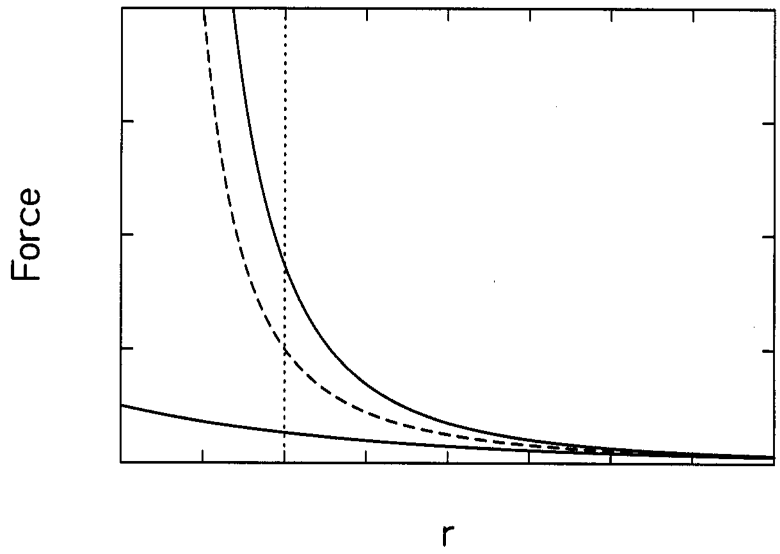

Figure 1.1: A qualitative signature of a Yukawa interaction. The dashed line shows the typical $1/r^2$ force between point objects, while the solid lines show the effects of adding Yukawa terms with the strengths $\alpha = \pm 1$. The dotted line is where $r = \lambda$.

is in the form of Dark Energy. Currently, little is known about this Dark Sector, except that its gravitational effects play a dominant role in the evolution of our universe. New short-distance gravitational interactions could elucidate this greatest of current mysteries.

The standard parameterization of a violation of the ISL used in experimental tests adds to the Newtonian gravitational potential a Yukawa term with strength α and range λ:

$$V(r) = \frac{Gm_1m_2}{r}\left[1 + \alpha e^{(-r/\lambda)}\right]; \tag{1.1}$$

this form will be used unless otherwise noted. Figure 1.1 shows the qualitative effect of a Yukawa term on the force between two point objects.

1.1.1 Large Extra Dimensions and The Gauge Hierarchy Problem

This experiment is one of a series [1] that was initially sparked by the proposal in Reference [7] that the extra dimensions of M-theory could be much larger than the Planck length and, as such, solve what is known as the gauge-hierarchy problem (GHP). The GHP is the recognition that the Planck scale ($M_P \sim 10^{19}$GeV) is vastly greater than the electroweak scale ($M_{EW} \sim 10^3$GeV).

Most extensions of the SM assume an as-yet-unobserved symmetry known as supersymmetry, which requires that for every boson(fermion) there exists a partner fermion(boson). This symmetry helps explain the presumed mass ($\sim$ 100GeV) of the Higgs boson, the field responsible for electroweak symmetry breaking which establishes the mass hierarchy of fermions and gauge fields. The sum of terms contributing to the calculation of this mass can run up to a scale Λ_{SM+} which is characteristic of the SM extension. One assumption is that $\Lambda_{SM+} \sim 10^{16}$GeV, the energy scale where the electric, weak and strong coupling constants coalesce. That a series of terms on the order of Λ_{SM+} sum to something on the order of 100 GeV is dubbed "unnatural" or so highly coincidental that the fact probably reveals a gap in our understanding. To get around this unnatural occurrence, the partners in a supersymmetric pair contribute to the Higgs mass with opposite signs, which allows such a low mass to arise from the sum of such large numbers. Within a few years, CERN's Large Hadron Collider should begin probing well into 10^3 GeV energy scale, which will reveal the Higgs, if it exists, and should also directly probe the scale of supersymmetry. While supersymmetry is appealing in that it resolves one hierarchy problem, it does nothing to address the enormous disparity between M_P and M_{EW}.

In the model of Reference [7], some of the extra dimensions of M-theory are allowed to have a macroscopic size; SM physics is constrained to a 3-dimensional slice (3-brane) of the higher dimensional theory, while gravity is free to propagate in the extra dimensions. Gravity, then, only *appears* weak (i.e M_P only *appears* large) on our 3-brane of the higher-dimensional space; its true energy content is spread over more dimensions than we (the SM) are aware. Since the form of the ISL is a consequence of our three spatial dimensions, measuring gravity at distances below the size of these large extra dimensions, R_*, would reveal $F \propto r^{-(2+n)}$ where n is the number of large extra dimensions. The effects of these dimensions would also be apparent when $r \geq R_*$ [3] as a Yukawa-form violation where

$$\lambda = R_* \quad \text{and} \quad \alpha = 8n/3 \tag{1.2}$$

and

$$R_* = \left(\frac{M_P}{M_*}\right)^{2/n} \left(\frac{\hbar}{2\pi c M_*}\right) \tag{1.3}$$

where M_* is the desired unification scale and M_P is the Planck mass. If the weak scale sets the scale of unification at $M_* \sim 10^3$ GeV, then, for n=2, one would expect to see a signal with strength $\sim$ 5 times gravity's at a range of 1 mm. Our initial results [1] have since pushed the unification scale in this particular scenario above 1.7 TeV. Reference [3] reviews some astrophysical constraints that require $R_* \ll 1$ μm when one assumes $M_* = 10^3$ GeV. With $n = 1$, R_* is of astronomical size and is constrained by solar system tests of GR [2]. For $n > 2$ the distances of interest are below 1nm, and these scenarios are still allowed by current direct searches in collider experiments [8].

The constraints above are for an extra-dimension manifold where the large extra dimensions are of toroidal geometry. There are other M-theory scenarios ([9],[10]) where the metric is not flat throughout the extra dimensions, but warped. In these models, the size of the extra dimensions can range from the very small to infinite but the curvature in these dimensions is responsible for addressing the GHP, either by a separation between our brane and the graviton brane (for small dimensions) or by the confinement of the graviton to a small range of the dimension (for infinite sized dimensions.) In either case, the signature of the ISL changing power as we directly probe the size of extra dimension is no longer accessible and such theories will only be addressed by collider experiments.

1.1.2 The Cosmological Constant Problem

A problem even greater than the GHP is the Cosmological Constant Problem (CCP) (see Reference [11] for a nice review.) Much as one needs to fine-tune the terms in the GHP so that the Higgs mass remains small, one must tune the terms summing to the expected vacuum energy to an even higher degree to match our observations. For a theory with a given cutoff scale k_{max} one expects the zero-point energies of that theory's fields to have a vacuum energy density $\Omega_\Lambda \sim \hbar c k_{max}^4$. Several apparently fundamental energy scales are known. As mentioned in relation to the GHP, the electroweak scale lies at about 10^3 GeV; a similar quantity for QCD, $M_{QCD} \sim 0.3$ GeV. In addition, the Planck mass and the scale of grand unification of the strong and the electroweak lie at 10^{19} GeV and 10^{16} GeV respectively. The contributions to the vacuum energy density from these scales range from $\Omega_\Lambda \sim 10^{36}\mathrm{erg/cm^3}$ for $k_{max} = M_{QCD}(c/\hbar)$ to $\Omega_\Lambda \sim 10^{110}\mathrm{erg/cm^3}$ for $k_{max} = M_P(c/\hbar)$. Meanwhile studies of distant Type Ia supernovae and of the cosmic microwave background anisotropies have shown us that the *actual* dark energy density is

$$\Omega_\Lambda \sim 6 \times 10^{-9}\mathrm{erg/cm^3}. \tag{1.4}$$

which is

$$\Omega_\Lambda \sim 0.7\ \Omega_{crit} \tag{1.5}$$

where

$$\Omega_{crit} = 3H_0^2/(8\pi G) = 8.8 \times 10^{-9}\mathrm{erg/cm^3} \tag{1.6}$$

is the critical density for the universe and

$$H_0 = 72\ \mathrm{km\ s^{-1}Mpc^{-1}} \tag{1.7}$$

is the WMAP value for the Hubble constant. A simpler way to view the CCP is just to note that $M_\Lambda = 8 \times 10^{-12}$ GeV, the observed scale of the dark energy, is 11 orders of magnitude smaller than any other known physical energy scale (except for the neutrino masses.)

We know that these vacuum excitations are real phenomena - the macroscopic manifestation of the Casimir force is well tested - so either there is an unnatural cancelation in the sum leading up to Equation 1.4, or we do not understand how vacuum excitations couple to gravity.

If the energy scale of Ω_Λ does not correspond to one of known physics, perhaps it is telling us of unknown physics. Reference [12] argues that this new energy scale, M_Λ, corresponds to a distance scale of $\sim 100\ \mu$m, and that since it is an entity known to us only through its gravitational interaction, it is natural to assume it has gravitational strength coupling. If such an effect exists, one would expect to see it in a direct probe of the ISL at this range.

A more concrete proposal for a violation of the ISL due to the Cosmological Constant is the idea of a "fat" graviton [13]. In this model, the graviton is an extended state of size $\lambda_g \equiv 1/\Lambda_{grav}$, where Λ_{grav} is some new energy scale. The features of this model are that the

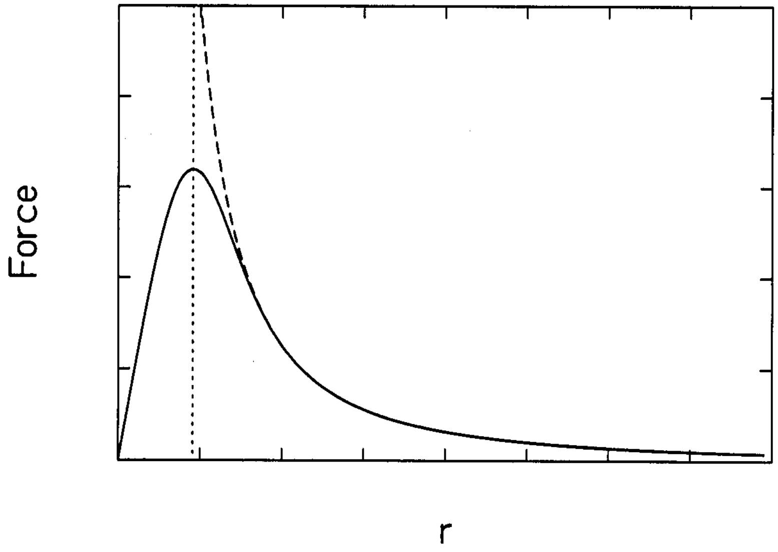

Figure 1.2: A qualitative signature of the "fat" graviton. The dashed line shows the typical $1/r^2$ force between point objects, while the extended size of the graviton modifies this interaction as shown in the solid line. The dotted line is where $r = \lambda_g$. As opposed to Figure 1.1, the modified force → 0 as $r \rightarrow 0$.

graviton can take a global view of Standard Model(SM) processes, suppressing couplings to vacuum excitations ("hard" processes where $\Lambda_{SM} \gg \Lambda_{grav}$) while still respecting the self-interaction processes that give composite objects mass. Since the graviton can not couple to short-distance SM loops, these loops do not contribute to the actual Ω_Λ, that part of the vacuum which gravitates. But, the graviton's vacuum excitations must themselves still gravitate, since they are, by definition, soft. Thus the lower limit on λ_g comes from Equation 1.4, by noting that if the vacuum energy is due solely to the vacuum excitations of the graviton itself, then $\Omega_\Lambda \sim O(\Lambda^4_{grav}/16\pi^2)$ which gives the limiting case

$$\lambda_g \geq 20\ \mu\text{m}. \tag{1.8}$$

The qualitative effects of this model are shown in Figure 1.2. Reference [13] does not provide a quantitative description of the expected gravitational force law. We note, however, the requirement that the force transitions smoothly from $F(r > \lambda_g) \propto 1/r^2$ to $F(r = 0) = 0$ is satisfied if

$$F(r) = -G\frac{m_1 m_2}{r^2}\left[1 - e^{-(r/\lambda_g)^3}\right] \tag{1.9}$$

where the only difference from the qualitative picture of Figure 1.2 is that the modified force law peaks at $r \sim 0.91\ \lambda_g$ instead of $r = \lambda_g$.

As our calculation methods (see Section 4.2) use the potential rather than the force, the fat graviton additional potential is

$$V_{FG}(r) = Gm_1m_2 \int dr \frac{e^{-(r/\lambda_g)^3}}{r^2} = -Gm_1m_2 \left(\frac{e^{-\frac{r^3}{\lambda_g{}^3}}}{r} + \frac{P(\frac{2}{3}, \frac{r^3}{\lambda_g{}^3})}{\lambda_g} \right) \tag{1.10}$$

where $P(a, x)$ is the incomplete gamma function. Note that, as opposed to a Yukawa coupling, the strength of this additional potential is not arbitrary, but constrained to have the value in Equation 1.9 to achieve the behavior shown in Figure 1.2.

1.1.3 Other New Exchange Forces

Moduli Mediated Forces

The ISL-violating signature of large extra dimensions of Reference [7] follows from the geometry of the higher-dimensional M-theory space. But M-theory also incorporates several new scalar bosons that may mediate macroscopic forces and thus show up as a violation of the ISL. The exchange of scalar bosons between like charges - mass, in this case - leads to an attractive interaction. The radion is one such scalar that stabilizes the size of the extra spatial dimensions of M-theory [14]. The strength of the radion's coupling to matter depends on the number of extra dimensions, n, for $n \geq 2$

$$\alpha_{rad} = \frac{n}{n+2} \tag{1.11}$$

while its range (mass) is determined by the unknown scale of the underlying string theory, M_*. The range of the radion's coupling to matter is

$$\lambda \approx 2.4 \left[\frac{\text{TeV}}{M_* c^2}\right]^2 \text{ mm.} \tag{1.12}$$

If 1 TeV$\leq M_* \leq$ 10 TeV, then 10^{-3} m $> \lambda_{rad} > 10^{-5}$ m.

The radion is just one of many "moduli" in M-theories that determine the geometry of the extra dimensions and dictate the effective parameters of our lower-dimensional SM. These moduli generally appear in models as massless scalar fields with gravitational-strength coupling, but, since these fields have not been detected in Equivalence Principle tests, the M-theorist must devise some mechanism to give these scalars mass, thus limiting their range.

A proposal related to the radion [15] is that low-energy supersymmetry-breaking gives the moduli masses $m_\phi \propto F/M_S$, where F is the scale where supersymmetry is broken and M_S is the string scale (assumed to be 5×10^{17}GeV.) These moduli then couple to SM quanta like quarks or gluons. Reference [16] sets as a bounding case $F \sim 2000$ TeV, at which point the lightest supersymmetric partner would be massive enough to overclose the universe. Both the scale and coupling of these moduli depend on F and earlier, more specific, predictions for their coupling to the gluons and quarks are shown in Figure 1.4; these latest predictions cover most of the shown parameter space in Figure 1.4;

Yet another modulus, the dilaton, determines the coupling constants in M-theory. A light dilaton could couple to SM particles with strengths between $\alpha \sim 1$ and $\alpha \sim 1000$ depending on the value of the strong coupling constant at the string scale [17]. The lower bounds on the mass of such a light dilaton is $\sim 7 \times 10^{-5}$eV, (or an upper bound of $\sim$ 3mm in its Compton wavelength.) Thus, experiments that measure the ISL below 3 mm further constrain this lower limit.

Gauge Bosons

The scenario of large extra dimensions can also allow for vector gauge bosons to propagate in the bulk, not confined to our SM brane [18]. The couplings of these bulk gauge bosons on our brane are diluted from their true couplings, much like gravity, but can still mediate forces more than 10^6 times stronger than gravity with meV-range masses. The exchange of vector bosons leads to a repulsive interaction between like charges, and, in this model, have the interesting potential to fill the void of a gauge field for the symmetries of baryon and lepton number.

Multi-particle Exchange Forces

Violations of the ISL can also take the form of a power-law potential,

$$V(r) = -\frac{Gm}{r}\left[1 + \beta_k \left(\frac{1\text{mm}}{r}\right)^{k-1}\right]. \tag{1.13}$$

These violations arise from the exchange of two massless particles. The integer in the exponent is determined by the type of exchange particles, either scalars, pseudoscalars, axions, or a neutrino-antineutrino pair, while the strength, β is determined by the type of coupling [3].

In the case where two massive pseudoscalars have γ_5 coupling, there is a long-range, spin-independent potential

$$V(r) = -\frac{Gm}{r}\left[1 + \gamma\frac{K_1(2r/\lambda)}{\lambda r^2}\right]. \tag{1.14}$$

where $K_1(x)$ is a modified Bessel function [19].

1.2 Experimental History

Newton was able to deduce his universal law of gravitation by supposing that the moon's orbit was maintained by the same force that drew objects to the earth's surface. That he was roughly correct can be thought of as a test of the ISL. That is, the ISL is not grossly violated at length scales between the earth's radius and the moon's orbit ($\sim 10^6$ to 10^8 meters). Einstein's General Relativity (GR) describes gravity as the interaction between energy and spacetime; in the non-relativistic limit of low mass and momentum, GR reduces to Newtonian gravity. For tests where relativistic effects are important, constraints on Yukawa interactions are understood as constraints on a violation of GR.

Today, the ISL has been tested over a much larger range of distances, from microscopic to astronomical scales. As Figures 1.3 and 1.4 indicate, there are no observed discrepancies from the ISL. A great variety of experimental techniques have been used to set the constraints of Figure 1.3 and one can easily understand the rough shape these limits. The exponential fall-off of the Yukawa interaction necessitates that two test masses be separated by a distance $d \sim \lambda$. Not only does this become more challenging at smaller d, but only

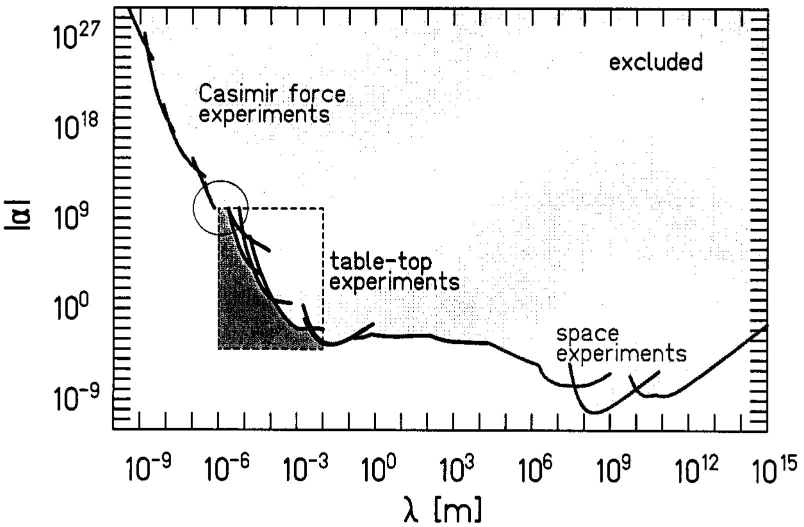

Figure 1.3: Constraints on the ISL-violating parameters α and λ. The circle indicates the discontinuity in the limits due to the difference between 95% and 68% limits. The outlined region is shown in greater detail in Figure 1.4.

the mass of the test body within $\sim \lambda$ of the other test body could significantly react to a Yukawa interaction. Above ranges of a few cm, we are hindered by our ability to manufacture or characterize source masses, and thus our limits plateau until we reach ranges where artifical satellites or the natural objects in the solar system provide us with test masses whose motions we can observe. This section reviews the experimental tests that set the most stringent constraints.

1.2.1 Constraints Below 10 μm

Below 10 μm, our tests of the inverse-square law are mainly inferred from measurements of the Casimir force. Casimir pointed out in 1948 (see [20] for a comprehensive review) that between two conducting surfaces, only certain modes of electromagnetic excitation meet the boundary conditions of the system and are allowed. But, free space has power at all frequencies of the electromagnetic spectrum. That is, the vacuum has an energy density.

Thus, if a region between two conducting plates excludes certain modes, then the plates will experience a pressure from the differential energy density between the inner and outer regions of their geometry. This pressure exerts a force on the two plates, producing the Casimir Force. The Casimir Force can be resolved at distances smaller than 10 μm. One can extract limits on ISL violations by parameterizing any deviation beyond the expected Casimir effect as a Yukawa violation. Collider experiments test even shorter distances for specific scenarios like the large extra dimensions, where one would observe missing energy escaping into an extra dimension, but a direct test of the ISL with colliders would be hindered by the weakness of gravity relative to the scattering forces and also the tiny masses of the test particles.

van der Waals

An early set of limits from tests of the van der Waals force set the shortest limits on the ISL [2]in the range 1nm $\leq \lambda \leq$ 3nm for $\alpha \sim 10^{26}$. These experiments are similar to "Ederth" described below, but used a dielectric surface rather than a metal one.

Ederth

Reference [21] used a template-stripping method where mica sheets were gold-coated, glued gold-side-down onto cylindrical sections (radius 10mm), and then immersed in a solvent to remove the mica. A hydrophilic hydrocarbon monolayer was applied to prevent adsorption of contaminants onto the surface, and also to prevent the two gold surfaces from cold-welding upon contact. This procedure produced a very smooth, uncontaminated surface ($\leq$0.4nm rms rougness over 1μm^2). Using two such cylinders as the test surfaces in a crossed formation, the experiment measured the Casimir force at a separation of 20nm by placing one of the cylindrical sections on a piezoelectric bimorph and measuring the charge from this bimorph as the position of the other cylinder was varied. Reference [22] analyzed this experiment to extract constraints on ISL-violations and sets limits in the range 2nm $\leq \lambda \leq$ 20nm for α down to $\sim 10^{20}$.

Mohideen

A second experiment [23] used an atomic force microscope to measure the force between a $\sim 200\mu$m diameter gold-coated polystyrene sphere and a flat surface. The sphere was attached to the end of a long thin cantilever. When a force acts on the sphere, the cantilever flexes and a pair of photodiodes detect the angle of deflection from a laser that reflects off the back of the cantilever. The flat plate was actuated with a piezoelectric, the force was calibrated electrically, and the relative distances read with an interferometer. This experiment was able to measure the Casimir force down to 62nm with about 1% precision. The ISL-violating limits from this experiment were extracted in Reference [24]. This experiment sets limits in the range $8\text{nm} \leq \lambda \leq 300\text{nm}$ for α between 10^{13} and 10^{20}.

Lamoreaux

One recent measurement [25] used a torsion balance to measure the Casimir force from 0.6 to 6 μm. A small gold-coated optical flat was mounted on one arm of a torsion balance and served as one of the conducting surfaces. The second surface was a gold-coated spherical lens mounted on a piezoelectric actuator. The relative separation of the two surfaces was measured with an interferometer while the absolute separation was inferred from the observed residual electrical attraction between the two plates whose presence was due to contact potentials : the electric and Casimir forces fall off differently with height. All forces on the balance were compensated electrically on the opposite balance arm. The voltage required to maintain zero deflection was used to determine the absolute and relative forces on the balance. This experiment was able to probe the Casimir force with about 5% accuracy. Reference [26] extracted limits for ISL violations from Reference [25]. This experiment sets limits in the range $100\text{nm} \leq \lambda \leq 10\mu\text{m}$ for α down to $\sim 10^9$.

Neutrons

Ultracold neutrons have also been used to probe this ultrashort regime [27]. Here, neutrons in the tail of the ultracold neutrons energy distribution are selected for energies in the peV range with velocities $\sim$ 2cm/s. These neutrons are directed into a cavity consisting of two horizontal plates. The upper plate is a neutron absorber while the lower plate is a neutron mirror. The neutrons propagate between the two plates. If they strike the absorber, they are absorbed or scattered out of the experiment, while if they strike the mirror, they are almost perfectly reflected. The neutrons are in the gravitational potential of the earth and thus have gravitational bound states. By adjusting the separation between the mirror and absorber and counting the transmitted neutrons, this experiment was able to resolve these gravitational bound states. If there were new short-range physics, the additional potential in the vicinity of the mirror would alter the bound states, thus changing the transmission as a function of separation. This experiment sets limits in the range $1\mu\text{m} \leq \lambda \leq 10\mu\text{m}$. These constraints are currently less stringent than those of [25] but it is claimed that a future experiment with greater statistics could improve these limits by 3 orders of magnitude in α. In any event, the diversity of physics testing this regime makes the constraints all the more robust.

1.2.2 μm to cm Ranges

The work described here was designed to improve experimental limits below 1mm. Figure 1.4 shows the experimental limits published before the results of this work as well as some of the theoretical predictions discussed earlier. The limits in this regime are gathered from either micromechanical high-frequency oscillators or low-frequency torsion oscillators. Except for the "Moscow" and "Irvine" works, the experiments in this range are relatively recent endeavors following the publication of Reference [7].

Stanford

The experiment of Reference [28] placed a 1.4 μg gold rectangular prism on the end of 250 μm long cantilever. Beneath the cantilever, an alternating set of gold and silicon bars was oscillated laterally such that the test mass would experience a time-varying force as a result of the density variation in the alternating bars. The deflection of the cantilever was measured using a fiber-optic interferometer. The attractor and detector masses were isolated electrically by a 3μm thick SiN shield which had 200nm of gold evaporated on both

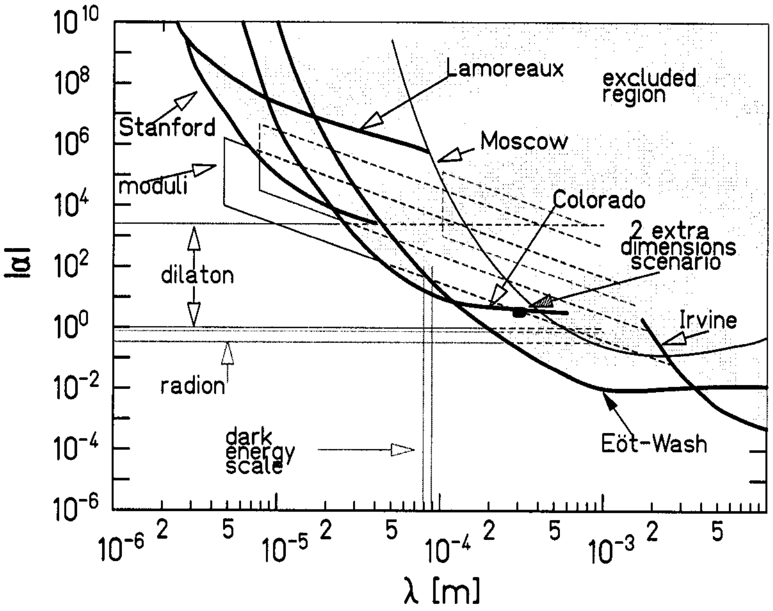

Figure 1.4: Previous constraints on Yukawa parameters α and λ.

sides. The attractor mass array was driven such that the Newtonian response to the density variation would occur on the resonance of the cantilever. To reduce the thermal noise, this experiment was cooled to liquid helium temperatures. The experiment resolved a signal on resonance, but the phase of this signal did not change as the equilibrium displacement of the attractor mass was varied, as one would expect from a signal related to the density variation. Shield motion could be responsible for an electrical or Casimir effect that explains this behavior. Nonetheless, the experiment was able to set significant limits on a signal that did change with the equilibrium displacement of the attractor mass array in the range $3\mu\text{m} \leq \lambda \leq 50\mu\text{m}$

Colorado

The experiment of Reference [29] also used a high frequency oscillator, but its torsional rather than cantilever mode was exploited for the measurement. A thin tungsten plane was constructed such that two rectangles were connected via a thin section. This detector possessed a torsion mode where the rectangles counter-rotated about the axis of the thin section. The attractor mass was a cantilever whose resonance was tuned to drive the counter-rotating mode of the detector plane. This cantilever was positioned below the detector plane (separated by a conducting shield) and on one side of the outer rectangle. The motion of the detector was measured with a capacitive sensor on the inner rectangle, while the attractor was driven with a piezoelectric transducer. This experiment resolved no signal and was able to place limits in the range $20\mu\text{m} \leq \lambda \leq 500\mu\text{m}$.

Eöt-Wash

The experiment of Reference [1] was the predecessor to the one described in this work and of a similar design. It was able to set limits in the range $20\mu\text{m} \leq \lambda \leq 4\text{mm}$.

Irvine

Reference [30] describes a pair of torsion balance tests, one to test ranges from 2 to 5cm and the other to test up to 105cm. By taking advantage of the fact that the gravitational potential from an infinitely long hollow cylinder is uniform inside the cylinder, the experiment was able to test the ISL in a near-null setup (it was only near-null due to the finite size of the cylinder and the test mass.) The cylinder diameter was $\sim$ 5cm while the separation between the test mass and the cylinder wall was $\sim$ 2cm. The test mass hung from one arm of a torsion balance while the other arm was actuated by electric force plates to counter the balance twist, which was monitored with an optical lever. The 5 to 105cm experiment compared the torque on a torsion balance arm between a mass at a distance of 5cm and a pair of masses at 105cm. These experiments found no deviation from the ISL, countered some earlier claims to that effect, and still set the best limits on α between 4mm and nearly 1 meter with the best constraint (for *all* ranges below 10km!) requiring $|\alpha| \leq 10^{-4}$ at $\lambda \sim 2\text{cm}$.

Moscow

Reference [31] is another torsion balance test where a two-armed balance had small spheres attached to either end. A third sphere was moved between positions 3 and 5 mm away from one end of the balance at regular intervals and the amplitude of the resulting angular oscillation was compared to a Newtonian prediction. This experiment saw no evidence for a violation of the ISL, and its limits have since been improved upon by several other experiments. Yet, until 2001, this experiment set the best limits between 100μm and a few mm and still allowed the possibility of a gravity-strength force with a range of a few 100 μm.

1.2.3 Ranges from 1 meter to 10km

Lake

Reference [32] compared the weights of two masses separated vertically by ~100 meters. The masses were weighed next to a water reservoir with one mass below the level of the reservoir and one above, so that the weight of the water gave opposite contributions to the two weights. The weight difference was tracked as the reservoir level varied by up to 43 meters to determine Newton's G. Because their value agreed well with other G measurements at ranges as small as a few cm the experiment set limits on ISL violations (which can also be thought of as testing the constancy of G over different ranges.) This experiment limits $\alpha \lesssim 2 \times 10^{-3}$ between a few centimeters and tens of meters.

Tower

Reference [33] combines the results from several different measurements of g with gravimeters at varying heights in radio towers up to 600 meters. These experiments required a detailed survey of g within a radius of several kilometers of the tower and that wind speeds at the measurement height were ≤ 5 km/hr. These measurements set limits between roughly 100 meters and 10 kilometers.

1.2.4 Astronomical Tests

Beyond a few kilometers our best constraints on α come from measuring the orbits of satellites around the Earth and planets around the Sun. The satellite measurements are generally made by ranging - emitting a light pulse from the ground and measuring the time it takes for the reflection of the pulse to return, while the planetary measurements are made by radar ranging and standard astronomical techniques.

LAGEOS

The LAGEOS satellites are two spheres, several hundred kilograms in mass, whose surfaces are covered with retroreflectors [2]. These satellites were launched into orbits around the Earth to measure its gravitational field and the precession of its axis of rotation. By measuring the acceleration towards the center of the Earth at different radii, one can compare the measurements to extract limits on ISL violations. This technique gives limits when comparing the LAGEOS orbits to ground-based measurements as well as comparing LAGEOS to the moon's orbit. These comparisons provide constraints from tens of kilometers to tens of thousands of kilometers.

Lunar Laser Ranging

A more stringent limit on the ISL can be had from lunar laser ranging. Three Apollo missions and one Soviet Luna mission left retroreflectors on the surface of the moon. By measuring the precession of the moon's orbit, one can test general relativity and extract limits on an ISL-violation for ranges comparable to the moon's orbital radius. This method measures the moon's orbit to ~ 1 centimeter (tests in the near-future will reduce this by a factor of ten [3]), and produces the most stringent constraint on ISL violations at $\lambda \sim 10^8$ meters requiring $|\alpha| \leq 10^{-10}$.

Planetary Radar Ranging

One can also extract constraints on ISL-violations by radar-ranging directly to planetary surfaces or by ranging to artificial satellites orbiting those planets to determine their orbital precession rates. This has been done for the inner planets as well as Jupiter and combined, these measurements best constrain ISL violations around 1 AU (1.5×10^{11}meters).

1.2.5 Larger Scales

Many different observations have led to the conclusion that there is a substantial amount of dark matter and dark energy in the universe; the energy density of dark energy $\Omega_\Lambda \sim 0.7\Omega_{crit}$, the energy density of dark matter $\Omega_{DM} \sim 0.25\Omega_{crit}$, while the baryons, photons, neutrinos and all other SM components account for the other 5% of Ω_{crit}. The evidence for this dark sector is entirely gleaned from gravitational phenomena. Evidence for dark matter comes from the rotation curves of galaxies, and from gravitational lensing around luminous structures. The dark energy is revealed to us through measurements of distant Type Ia supernovae and studies of the cosmic microwave background anisotropies. These phenomena are explained very well by GR with the given dark sector contributions, but it is tempting to explain these observations by modifying the ISL at large distances, rather than assume that 95% of the universe is a mystery to us. One way to constrain such speculation is by studying the formation of large-scale structure. Reference [34] constrains $|\alpha| \leq 1$ on scales between 10^{22} and 10^{23} meters by comparing data from the Sloan Digital Sky Survey to models of large-scale structure formation with Yukawa type interactions. Clearly, there is a large gap in our current knowledge on scales between the solar system size and the size of galactic clusters.

Chapter 2

APPARATUS

The apparatus described here was derived from a previous torsion balance experiment of the Eöt-Wash group, [35]. Wherever applicable, I have referred to that description.

2.1 General Principles

Our goal was to measure the gravitational interaction between test masses as the separation between those masses varied. Our measurement device was a torsion pendulum that supported a thin, dense, detector ring with two concentric arrays of 21 holes each,where the plane of the ring was aligned perpendicular to the torsion fiber. These arrays of holes gave the detector ring a discrete polar symmetry of m=21, where m is an integer such that each $\frac{2\pi}{m}$ radian section of the ring is identical, as used in spherical harmonics. An attractor ring of an identical $m = 21$ symmetry rotated beneath the detector array.

The density difference between the ring material and the density of the holes (zero) created a gravitational potential at any point above the attractor ring that varied harmonically with the azimuthal angle, ϕ, as well as with radial and vertical displacement, $\vec{r}$,

$$V(\phi, \vec{r}) = \sum_{m}^{N} A_m(\vec{r}) \sin(m\phi) \tag{2.1}$$

where the sum is over m =21, 42 and 63 and accounts for the fact that V is not a purely sinusoidal function of ϕ. We rotated the attractor ring such that $\phi(t) = \omega_1 t$ and the spatially-varying $V(\phi)$ became a time-varying $V(t)$,

$$V(t, \vec{r}) = \sum_{m}^{N} A_m(\vec{r}) \sin(m\omega_1 t) \tag{2.2}$$

as seen from the detector's frame. That is, when the holes of the attractor and detector rings were aligned, the configuration was at a potential energy minimum, and when they were rotated out of phase by $\frac{2\pi}{42}$ the configuration was at a potential energy maximum. We chose ω_1 so that the gravitational signal frequencies $\omega_m \equiv m\omega_1$ were near the natural frequency of our torsion pendulum, Ω. The detector ring then experienced a torque,

$$N(t) = -\frac{\partial}{\partial t} \oint_{V_d} V(t, \vec{r}) d^3r \tag{2.3}$$

where the integral is over the volume of the detector ring. The pendulum responded to this torque with an angular deflection, $\theta(t)$, at the same frequencies ω_m. We discuss the calculation of the harmonic amplitudes of $N(t)$ in Chapter 4 and the conversion of the observed angular amplitudes into torques in Section 3.3.

The amplitude of these angular oscillations at frequencies ω_m varied with the vertical (s in Figure 2.1) and axial separation of the detector and attractor rings. After we aligned the axes of the attractor and detector rings, we measured these amplitudes as s varied from several millimeters down to 65μm, and compared these signals to our Newtonian model.

This experiment searched for a new-physics signal above a resolved Newtonian background. The gravitational interaction of interest was small relative to potential electrostatic interactions between the two pieces, so we interposed a conducting membrane between our detector and attractor rings. To reduce the Newtonian background, we mounted a second attractor ring directly below the first with a relative phase of $\frac{2\pi}{42}$ so that the Newtonian signal at frequency ω_{21} was canceled by about a factor of 50. As the gravitational signal was a complicated function of the detector and attractor geometry, we relied on our ability to machine, measure and align the different components of the experiment.

We continuously calibrated our angular scale to torque by placing three small spheres on the pendulum body. Three large brass spheres rotated outside of the vacuum vessel at a radial separation of $\sim$ 15 cm where Newton's G is well known and where the violations of the ISL are known to be small. The gravitational torque between these two sets of spheres, N_{cal} is easy to calculate and, by measuring the amplitude of the calibration signal (itself set at some specific frequency, ω_{cal}) at the same time as our short-range signals, we were able to consistently convert angular amplitudes into torque.

The following sections describe in detail our apparatus, focusing on the relevant dimensional characterizations, alignments and calibration.

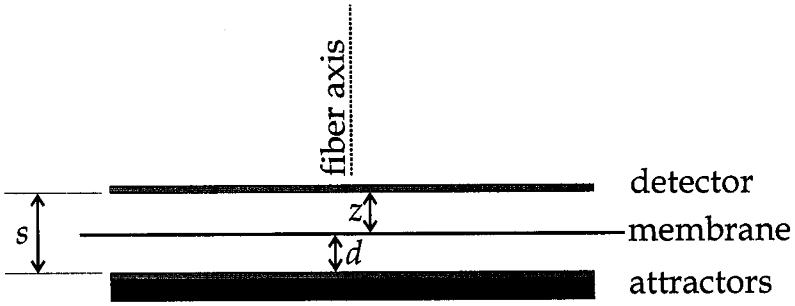

Figure 2.1: A side view of the vertical separation between the detector and attractor rings. The vertical separation, s, is comprised of the attractor-membrane separation, d, the thickness of the conducting membrane and the detector-membrane separation z.

2.2 Detector and Attractor Rings

Our test masses were the missing masses of arrays of holes machined into three thin rings, shown schematically in Figure 2.2. The raw material for each ring was a commercially-available sputtering target (ESPI. Ashland, Oregon) . The detector and upper attractor rings were molybdenum, while the lower attractor ring was tantalum. We chose these materials for their high density and machinability. Our goals in the fabrication of these rings were

- uniform thicknesses and smooth surfaces of the rings.
- a high precision in the placement and radii of the holes
- the prevention of any magnetic contamination of our rings
- the ability to directly measure the missing mass of the holes

The first of these two requirements allowed us to model the rings more easily. The deviations from ideal dimensions were on the order of a few μm. As discussed in detail in Section 5.3, these deviations were small enough to allow us to use the average measured dimensions in our model and avoid an extremely complex model. The third requirement assured us that there would be no spurious magnetic coupling between our attractor and detector rings

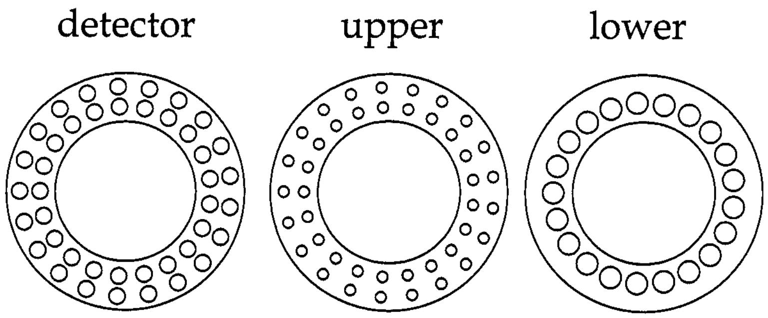

Figure 2.2: A top-view of the detector and attractor rings. The dimensions are given in Table 2.1

or between the detector ring and the environment. The final requirement allowed us to precisely measure the missing masses which gave us three key experimental parameters, $\overline{m}_d$, $\overline{m}_u$ and $\overline{m}_l$, the average missing masses in the holes of the detector, upper attractor and lower attractor rings respectively.

Experience from previous measurements had shown us that molybdenum was torn at the 100 μm level with conventional tooling and that the resulting pieces were likely to have small bits of the tooling embedded in them. These peculiarities were unacceptable in that they resulted in rough, difficult-to-characterize surfaces with potentially-disastrous magnetic contamination. For the rings of this experiment, we employed an Electric Discharge Machine (EDM) (Chamilles Technologies Robofil 300), which, in addition to creating a much smoother finish on the molybdenum pieces, utilized a computer-controlled feed table that allowed an absolute precision of ≈ 3 μm. The EDM performed similarly with the tantalum, which we had not attempted to machine previously. We met our fabrication goals through the following sequence of steps.

- Each sputtering target was lapped by a commercial lapping company to the desired thickness. (Acralap Inc. Carson, CA)

- Each target was placed in a 10% HCl solution for 5 to 10 minutes to remove any ferromagnetic surface contamination resulting from the lapping.

- The rings were then machined from the targets. For the I.D. of the rings (and, eventually for the holes) it was necessary to use a conventional drill to create a hole through which the EDM wire could be threaded. The final cuts were made with the EDM so that any chips of tooling would be removed during the EDM cutting.
- The rings were weighed.
- The arrays of holes were cut in the rings.
- The rings were weighed again.

After machining, we measured the dimensions of the rings on a coordinate measuring machine (CMM) (Browne&Sharpe 765 runnning PC-DMIS software.) To ensure the calibration of the CMM, the measurements were made along with a measurement of a NIST-traceable ring gauge, whose radius was known to better than 0.25μm. The measurements of the hole radii and the hole-array radii were made by measuring the point of contact of the CMM probe on the surface of the holes. Each hole was sampled six times at three different depths and the errors on the mean of these 126 measurements (63 for the lower attractor) were 0.2, 0.2, and 0.5 μm for the detector, upper, and lower rings respectively. The observed repeatability of the CMM was 0.75μ m, so the combined error of the three average hole radii were taken to be 0.8, 0.8, and 0.85 μm. We took as the radii of the hole arrays the radii of best-fit circles to the measured centers of the holes. Figures 2.3 and 2.4 show the measured scatter in hole position placement around a best-fit circle for each array. The measurements of the ring thicknesses were also made with the CMM. These measurements had the same repeatability as the hole measurements and the errors listed in Table 2.1 for the average thicknesses also combine the repeatability and the error on the mean of a large number of points.

To measure the missing masses, we weighed the detector and top attractor rings on a digital analytic balance (Sartorius Model LA 310 S, resolution 100 μg), whose calibration was checked against comparable calibration weights whose masses were known to better than 20 μg. We weighed the lower attractor ring before this balance was purchased, and instead

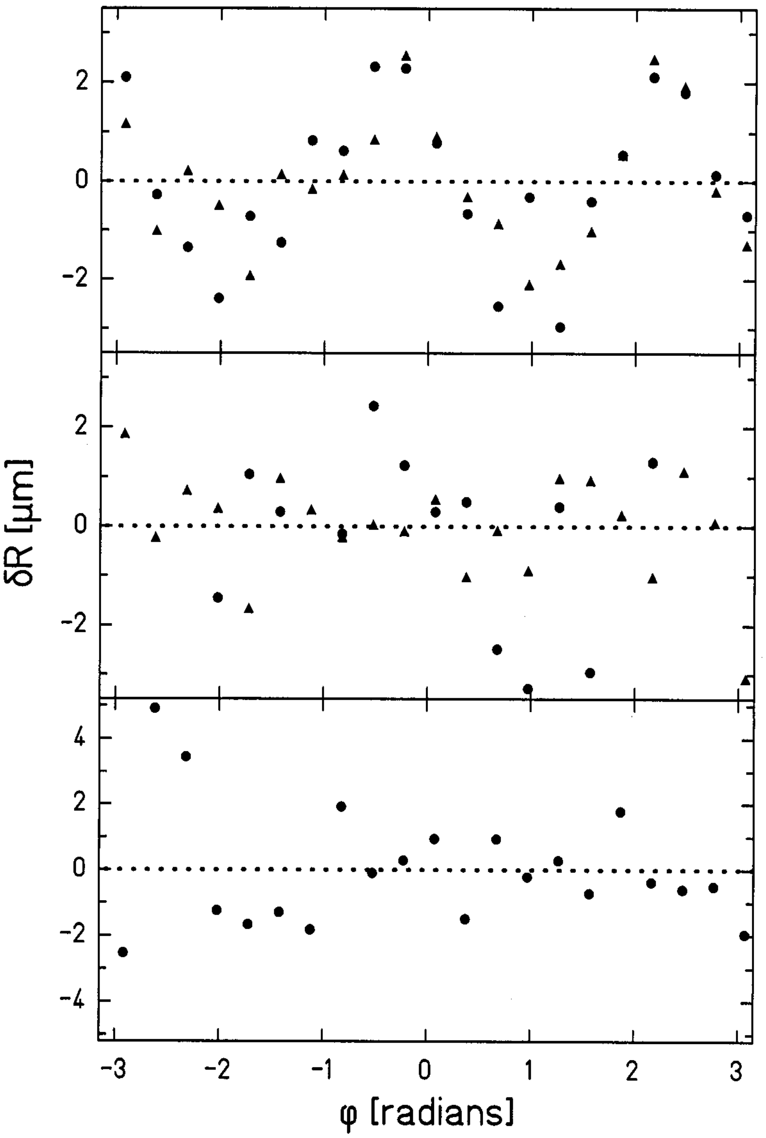

Figure 2.3: The radial deviation of our hole positions from the best-fit circles plotted versus angle around the rings. The top, middle, and lower plots are for the detector, upper attractor and lower attractor respectively. The circles represent deviations of hole positions in the inner arrays, while the triangles represent deviations in the outer arrays. The nominal precisions of the EDM that created the part and the CMM that measured the part was $\sim 2\ \mu$m.

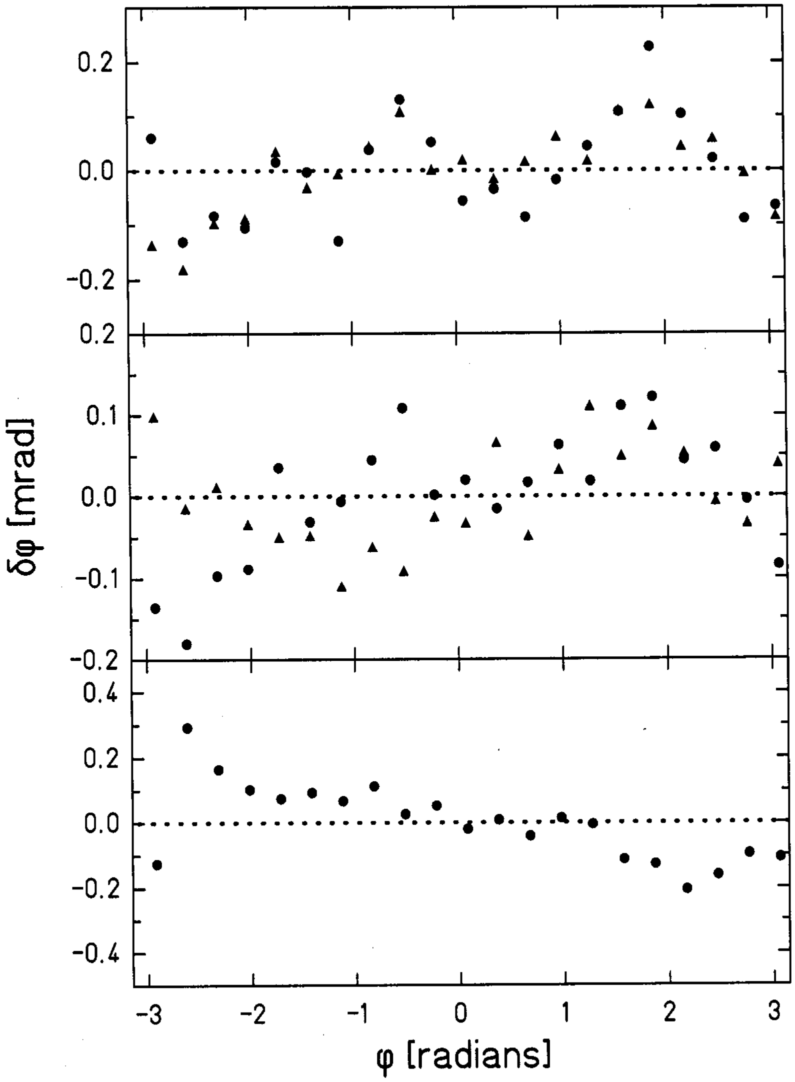

Figure 2.4: The angular deviation of our hole positions from nominal angles on the best-fit circle. The top, middle, and lower plots are for the detector, upper attractor and lower attractor respectively. The circles represent deviations of hole positions in the inner arrays, while the triangles represent deviations in the outer arrays.

Table 2.1: Measurements of the active-mass rings. O.R. and I.R. are the outer and inner radii of a ring, $\overline{h}$ is its average thickness, R_1 and R_2 are the best-fit radii of the hole patterns, $\overline{r}$ is the average hole radius, and $\overline{m}$ is the average hole mass. The error of the last significant digit is shown in parentheses for the radii and the masses, which are used as fit parameters. The errors of R_1 and R_2 are discussed in Section 5.3.5. Linear dimensions are in millimeters and masses are in grams.

Ring	O.R.	I.R.	$\overline{h}$	R_1	R_2	$\overline{r}$	$\overline{m}$
detector	35.14	21.08	0.9993(9)	25.1695	31.1694	2.3813(8)	0.18329(8)
upper	35.14	20.75	0.9968(9)	25.1687	31.1690	1.5866(8)	0.081634(3)
lower	35.14	21.08	3.0323(9)	26.8860	N/A	3.1720(9)	1.6026(3)

weighed it on an equal-arm balance. The weights used in the equal-arm measurement were later weighed on the digital balance. The error on the average missing mass per hole listed in Table 2.1 combined the error on the mean of a few repeated measurements along with the resolution of the balance. The balance display always agreed with the known mass of the calibration mass. Table 2.1 lists the *average* missing mass, but we measured the *total* missing mass, so the errors are smaller by a factor of 42, 42, and 21 than the actual measurement error for the detector, upper, and lower rings respectively.

Figure 2.2 shows a diagram of the three rings and Table 2.1 summarizes the measured characteristics of the three rings.

2.3 Torsion Pendulum

Our torsion pendulum was a light aluminum frame which hung from our torsion fiber and served as a mount for the detector ring and the reflecting mirrors. This frame incorporated a mechanism for adjusting the angle of the detector ring relative to the fiber axis, and supported one set of spheres used in our calibration.

2.3.1 The Torsion Fiber

Our torsion fiber was a 20 μm diameter, $\approx$ 80 cm long, uncoated tungsten fiber, whereas Ref. [35] used a gold-coated tungsten fiber. The quality factor, Q, of an oscillator indicates the amount of dissipation (and thus noise, see Section 5.1) which the oscillator suffers. We found a typical Q of the gold-coated fiber was $\approx$ 1500 while an uncoated fiber gave $Q \approx 3000$. This simple change reduced our noise by about a factor of 2 in power. The fiber had a breaking strength comparable to a $\approx$ 100 g load. We did not want to stretch the fiber to an inelastic point, so we limited our pendulum mass to be < 40 g. The ends of the fiber were crimped into small copper tubes that were glued into 4-40 copper screws.

The torsional spring constant of the fiber, κ depends on the material and dimensions of the fiber,

$$\kappa = \frac{M_s \pi r^4}{2L} \tag{2.4}$$

where M_s is the shear modulus of the material (150 GPa for tungsten), r is the radius of the fiber, and L is the length of the fiber. Using the nominal values for our fiber, $\kappa \sim 3 \frac{\text{fNm}}{\mu\text{radian}}$. κ is related to the pendulum's moment of inertia, I, and the natural angular frequency, Ω by

$$\kappa = I\Omega^2 \tag{2.5}$$

From a detailed model of the entire pendulum (nominal dimensions and densities), we calculate that $I \sim 1.93 \times 10^{-5}$ kg m^2 and we measure $\Omega \sim 2\pi/(495 \text{ seconds})$, giving $\kappa \sim 3.11 \frac{\text{fNm}}{\mu\text{radian}}$, in good agreement with our expectations. As discussed later, our calibration technique relied only on the value of Ω and the masses and locations of our calibration spheres; we did not *really* need to know κ, but it was helpful to calculate it for design purposes.

Our measurements exploited the torsion mode of our pendulum, but the pendulum has several other modes that pose potential problems. These modes are the simple-pendulum *swing* mode, the double-pendulum *wobble* mode and the linear-spring *bounce* mode, shown schematically in figure 2.5. When the detector ring was very near the conducting membrane, its motion in these other degrees of freedom could have allowed the detector ring to hit the conducting membrane. A single hit could have given the pendulum enough angular amplitude so that its motion was no longer on the scale of our detector and our data would have ended prematurely. A typical "subcut" of data (see Section 3.3 for more on data taking) lasted about 33 minutes, while $\sim$ 25 ($\geq$12 hours) of these subcuts were needed to

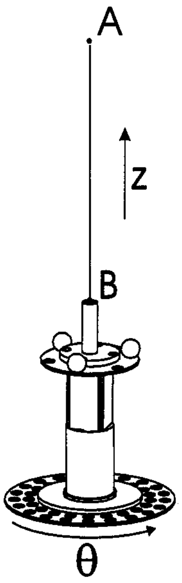

Figure 2.5: The modes of our torsion pendulum. θ indicates the torsion mode with $f \approx 0.002$ Hz. The bounce mode is a stretching of the fiber in the z direction with $f \approx 8$ Hz. The swing mode, or, the simple pendulum mode, rotates about point A at $f \approx 0.5$ Hz. The wobble mode is the double-pendulum mode, where the rotations about points A and B have opposite directions, at $f \approx 2$ Hz. The length and diameter of the fiber are not shown to scale.

reach our target resolution of 0.003 fNm. Once the pendulum was out of the range of our detector, it took between 10 minutes and one hour to damp its motion; as this maneuver was not automated, periodic disturbances of this kind significantly increased the time needed to achieve good statistics on our closest data points.

2.3.2 The Pendulum Frame

We used a pendulum frame where the $m = 4$ moments were minimized to allow a more accurate absolute and relative calibration as described in Section 2.4. This frame was approximately cylindrical to prevent any unwanted coupling to the rotating attractor or calibration turntable. The pendulum frame was made of four separate pieces. The uppermost piece was an aluminum post with a small flange at its base. The fiber screw threaded into the top of the post, while the base flange had clearance holes for four 1-72 beveled socket-

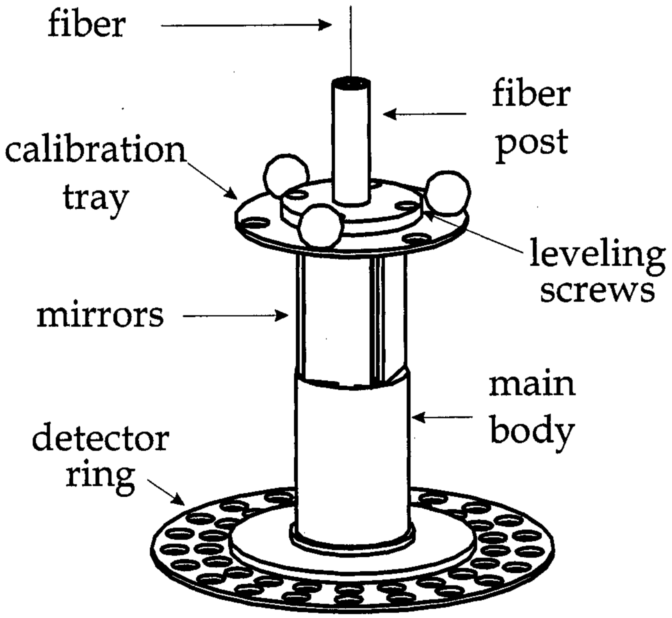

Figure 2.6: The pendulum frame and detector ring. The calibration tray and spheres, as described in Section 2.4, are shown.

cap titanium screws that threaded into a similar flange at the top of the main pendulum body. These screws sandwiched the four pieces together : between the fiber attachment post and the main body were a thin aluminum calibration tray that held our calibration spheres and a BeCu wave washer that was critical in the alignment of the detector ring. The main body had a mounting point for the detector ring, and four gold-coated mirrors 0.1 cm thick x 1.25 cm wide x 2.5 cm high were mounted as shown in Figure 2.6.

We wanted to level the detector ring so that its axis was parallel (if not axially aligned also) with the fiber axis. If these two axes were significantly misaligned, a torque from the attractor would not induce just a twist angle in the pendulum, but motion around some other axis. We redesigned our leveling scheme to preserve the cylindrical symmetry of our pendulum body. Our pendulum immediately preceding this one was leveled by translating small copper ballast screws to shift the pendulum's center-of-mass (COM) relative to the fiber suspension point, which changed the angle of the detector ring relative to the fiber. This method was unappealing in that, to level the detector ring, these screws might have

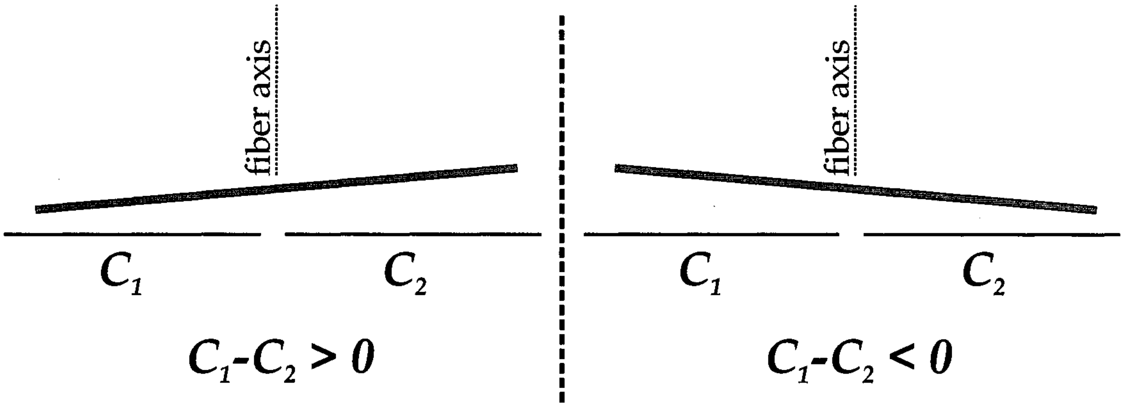

Figure 2.7: The leveling scheme for the pendulum. Only the fiber and detector ring are shown above two capacitor plates. The signal $C_1 - C_2$ changes sign from the left frame to the right frame as the pendulum twists by 180 degrees.

to be translated into a very asymmetric formation. These screws were two sets of opposed screws oriented perpendicularly to each other and the fiber axis. This asymmetric alignment of the screws had a small $m = 4$ symmetry. As described in Section 2.4, an $m = 4$ symmetry on the pendulum body interferes with our alignment of the calibration turntable relative to the pendulum calibration spheres.

To replace this system, we reverted to an even earlier method where we translated the fiber suspension point above the COM rather than the COM itself. One can easily see the appeal of this system. Consider a pendulum whose COM, M is a distance l below a suspension point and a distance δ away from the fiber axis (via some design flaw.) The pendulum then hangs at some angle, $\gamma \sim \delta/l$ from the designed vertical. To set $\gamma = 0$, one must move a small ballast mass, m, a distance $\sim \delta\sqrt{M/m}$, while moving the suspension point requires a motion of only $\sim \delta$. We implemented this leveling scheme by tweaking the small screws that held the four pieces of the pendulum body together. Tightening one of these screws compressed the wave washer and slightly angled the fiber post relative to the rest of the pendulum body, moving the suspension point relative to the COM. We leveled the pendulum by suspending it above two copper plates with a gap between them roughly aligned with the fiber axis (Figure 2.7.) As the pendulum twisted on the fiber, we measured the difference in capacitance between the two plates and looked for the part of this signal which varied with pendulum rotation; the pendulum served as the common second plate for the two capacitors. We calibrated this measurement by placing a small, 0.1 g brass nut on the edge of the detector ring, which produced a known tilt of 1.2 mrad. By tuning the four screws, we adjusted the angular misalignment between the detector ring axis and the fiber axis to be ≤ 80 μrad.

2.3.3 Fiber Positioning and Suspension

To test the ISL effectively, we varied both the vertical and axial separation between our detector and attractor rings. The fiber positioning hardware was the same as described in [35], allowing motion in X, Y, Z, and θ. We used a new controller for these stepper motors, the Newport Corporation's ESP 7000. We permanently mounted a digital indicator, Mitutoyo model 543-262 with a resolution of 1μm, to each axis and these were read into our data acquisition system at the start and end of each run through a Midwest Flex Systems FP-4M gauge interface.

These actuators controlled the position of a vertical 8 mm diameter shaft. A magnetic eddy current damper was attached to the bottom of the shaft, and the fiber was suspended from this damper as described in [35]. We added an additional copper bellows to the existing one to reduce the bounce frequency of the pendulum. This shifted the bounce resonance farther below an observed building resonance of $\approx$ 12Hz.

2.4 Calibration Turntable

The calibration turntable provided a well-known gravitational calibration torque on the pendulum calibration spheres. By making sure that the relative positions of the pendulum and calibration table never changed - i.e. when the pendulum moved, we moved the turntable - we were able to correct our data for any position-dependent effects in our optics, for instance a mirror curvature that varied with height; this was our *relative* calibration. Because we could calculate this torque to some precision, we used the angular deflection of the pendulum at the calibration frequency to convert all angular deflections into torques;

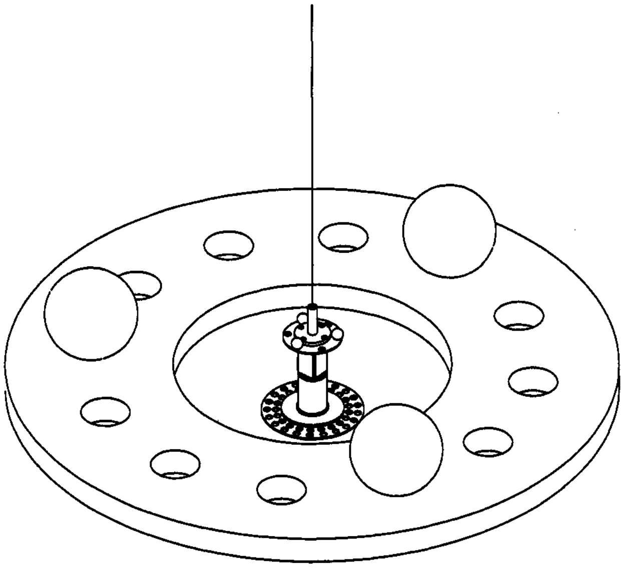

Figure 2.8: The pendulum and calibration spheres. Just the platter of the turntable is shown. The vacuum vessel and magnetic shielding that separate the pendulum from the turntable are not shown.

this was our *absolute* calibration.

The turntable was a 0.75" thick aluminum platter with 12, 1.321" diameter holes spaced evenly on a circle of diameter 12.000". By design, neither the 12 holes in this platter, nor the pendulum body nor the detector ring had an $m = 3$ gravitational moment, so that the torque between the three small calibration spheres on the pendulum and three large brass spheres placed on the platter was solely responsible for a signal at frequency ω_{cal}, three times the rotation frequency of the platter. A schematic of the calibration spheres around the pendulum is shown in Figure 2.8.

The turntable was large enough to fit around the bottom vacuum vessel and was turned by a sprocket-and-chain drive with the same model stepper motor that drove the short-range attractor. The turntable had $\approx \pm 5$ mm of horizontal motion along linear slide bearings, while there was ± 25 mm of vertical travel along three sections of threaded rod. The position of the turntable was indicated by five, 0.001 in. resolution dial indicators, one for each of the two horizontal directions, and one for each leg of the vertical translation.

Table 2.2: Measured values and uncertainties for the calculation of our calibration torque.

Quantity	Value	Uncertainty	Torque Uncertainty
G	6.6742×10^{-11} m^{3}kg^{-1}s^{-2}	0.001×10^{-11} m^{3}kg^{-1}s^{-2}	1.3×10^{-3} fNm
m	7.3448×10^{-4} kg	2×10^{-8} kg	2.3×10^{-4} fNm
M	1.136845 kg	1.7×10^{-6} kg	1.3×10^{-5} fNm
r	1.715×10^{-2} m	1.3×10^{-5} m	2.0×10^{-2} fNm
R	1.5240×10^{-1} m	1.3×10^{-5} m	2.9×10^{-3} fNm
ζ_0	0.0 mm	0.1 mm	2×10^{-5} fNm
δ_0	0.0 mm	0.16 mm	1.5×10^{-5} fNm
N_{cal}	8.835 fNm	0.003 fNm (statistical)	0.020 fNm

2.4.1 Calibration Torque Calculation

The gravitational torque between the two sets of spheres is easy to calculate, as one can treat the spheres as point masses. For concentric sets of 3 spheres, the torque at a given relative angle, ϕ, and relative vertical displacement, ζ, is

$$N(\phi, z) = 3GMmrR\sum_{i=0}^{2}\frac{\sin(\phi + i\frac{2\pi}{3})}{(r^2 + R^2 + z^2 - 2rR\cos(\phi + i\frac{2\pi}{3}))^{3/2}} \tag{2.6}$$

where M and m are the average masses of the calibration and pendulum spheres respectively and R and r are the distances of the calibration and pendulum spheres from the rotation axis and fiber axis respectively. We measured the fundamental harmonic of this torque that occurred at the third harmonic of the platter rotation frequency, N_{cal}, which can easily be calculated,

$$N_{cal}(\zeta) = \frac{1}{\pi}\int_0^{2\pi} d\phi N(\phi, \zeta)\sin(3\phi). \tag{2.7}$$

The masses, radii, and G are measured quantities: we measured m on our digital analytic balance; M was measured by a commercial calibration company (Northwest Calibration Systems Inc., Seattle, WA); R was measured with large calipers on the outsides of the large spheres accounting for the radii of the sphere; r was taken as the nominal dimension with the error taken as the resolution of the mill on which it was made - this quantity dominates our error budget and will be measured at the end of our current data run on our coordinate measuring machine to 10 times better precision. We calculated the contribution of these measurement uncertainties to the uncertainty in our calibration torque,

$$\delta N_{cal}^2 = (\frac{\partial N_{cal}}{\partial \xi})^2 \delta\xi^2 \tag{2.8}$$

where ξ is any one of these measured parameters. Table 2.2 shows the contribution of these errors to the calculated value of N_{cal} as well as the contributed uncertainties from the turntable centering as discussed below.

2.4.2 Calibration Centering

The analysis of the preceding section *assumed* that the two sets of spheres were coaxial and vertically aligned. One can generalize the calculation above to account for axial displacements between the two sets of spheres. The torque N_{cal} is relatively insensitive to axial, δ, or vertical, ζ, displacements of a few millimeters; $\delta N_{cal}/N_{cal} = 1.1 \times 10^{-3}$ over a 4 mm change of δ from center, δ_0. Because our turntable fit around our bottom vacuum can, we were constrained to $\approx$ 8mm of motion in δ. This insensitivity made precise axial alignment unimportant, but also difficult; we wanted to align the two sets better than measuring N_{cal} could tell us.

To improve the alignment in δ, we added two more spheres to our turntable in diametrically opposed holes. With the two sets axially aligned, we would nominally see no torque at 2 or 4 times the rotation frequency of the calibration table. But, as shown in Reference [36], displacing an inner mass multipole q_{lm} induces new moments $q_{l+1,m\pm1}$. The translated q_{33} of the pendulum spheres induced new moments about the turntable axis of q_{42} and q_{44} which then coupled to the corresponding moments of our two calibration spheres. We chose to monitor the $m = 4$ signal from our centering data, as the $m = 2$ moments of our pendulum were more sensitive to machining imperfections. Equation 10 of Reference [36] shows that the displacement is linear in the axial offset, δ. We centered the system by measuring the in- and out-of-phase components of angular displacement at the 4th harmonic of the calibration turntable and moved the calibration turntable so that this torque was minimized. Figure 2.9 shows the data from this procedure, with the centered signal measured as 3.8±2.3 nrad.

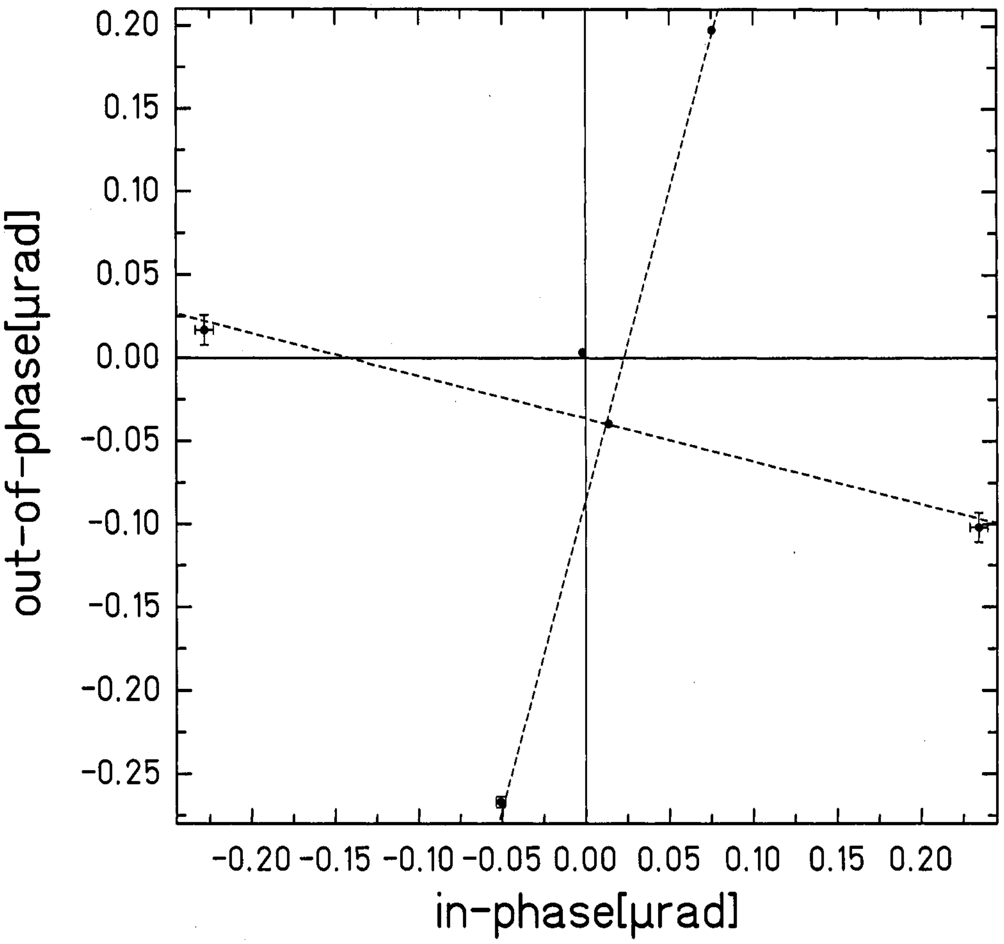

Figure 2.9: Data from our centering procedure for the calibration turntable. Shown is the measured in- and out-of- phase components of the 4th harmonic. The dashed lines show the best-fit line to the torque as it varied with motions of roughly ±3.5 mm along the x and y axes of the turntable. The measurement near (0,0) was taken after the other five measurements revealed the direction of the offset. For those points where the error bars are not visible, the errors are smaller than the size of the points. The final, centered point is within 160 μm of center.

The pendulum body had a small inherent $m = 4$ moment, which could have produced a 5 nrad angular amplitude in these measurements. We concluded that, in the worst case, we are $\approx$ 11 nrad of amplitude away from the true center, which, with the observed slope of $\approx$ 70 nrad/mm, limits our axial misalignment to be $\leq$ 160μm, which corresponds to an uncertainty in N_{cal} of $\leq 1.5 \times 10^{-5}$ fNm.

Once we were certain of the alignment of the fiber and turntable axes, we centered the two sets of spheres vertically. Because we wanted to use our calibration torque to correct for position-dependent effects in our optics, we ensured that all of our calibration centering data were taken with the pendulum in one particular position by moving the turntable to different relative positions around the stationary pendulum. The range of motion in the ζ-axis was greater than in the x-y axes, and we were able to directly observe the ζ-dependence of N_{cal}.

N_{cal} is symmetric in ζ about the $x-y$ plane of the pendulum spheres. Figure 2.10 shows the results of fitting our ζ-centering data to a fit with three parameters : κ, the torque scale for this position; ζ_0, the position of the center of the pendulum spheres in coordinates of the turntable's ζ axis; and δ_0 to account for any slight dependence on the shape of this function with horizontal offset. This was an excellent fit to this data showed $\zeta_0 = 26.23 \pm 0.07$ mm. Our "centered" run was at $\zeta = 26.21$ mm, so we assign an uncertainty in our ζ alignment of 100μm, which corresponds to an uncertainty in N_{cal} of 2×10^{-5} fNm.

2.5 Attractor Mount, Conducting Membrane, and Pendulum Housing

This experiment was insensitive to long-term mechanical and temperature drifts because our signals occurred at definite frequencies, ω_n and ω_{cal} in the mHz range. Setting the signal frequency at some high multiple of the fundamental rotation frequency also helped reduce any systematic associated with the rotation of the attractor assembly. Nonetheless, the rotating attractor posed much challenge as it was mechanically coupled to the vacuum vessel and thus to the optics and indirectly to the pendulum. The major components of the attractor drive mechanism are shown schematically in Figure 2.11 and discussed below.

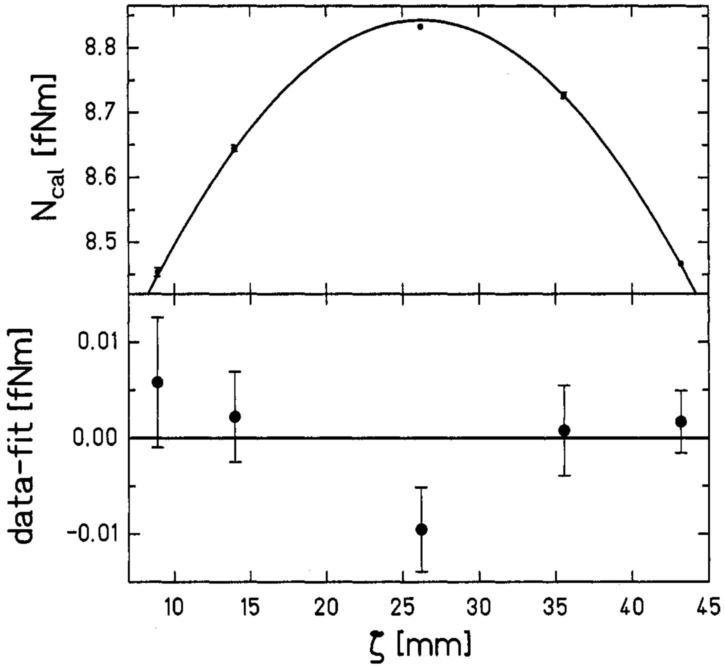

Figure 2.10: Data from our centering procedure for the calibration turntable. The top panel shows the data and fit of N_{cal} as we varied ζ. The residuals are shown in the bottom panel. The final, centered point is within 20 ± 70 μm of the fitted center.

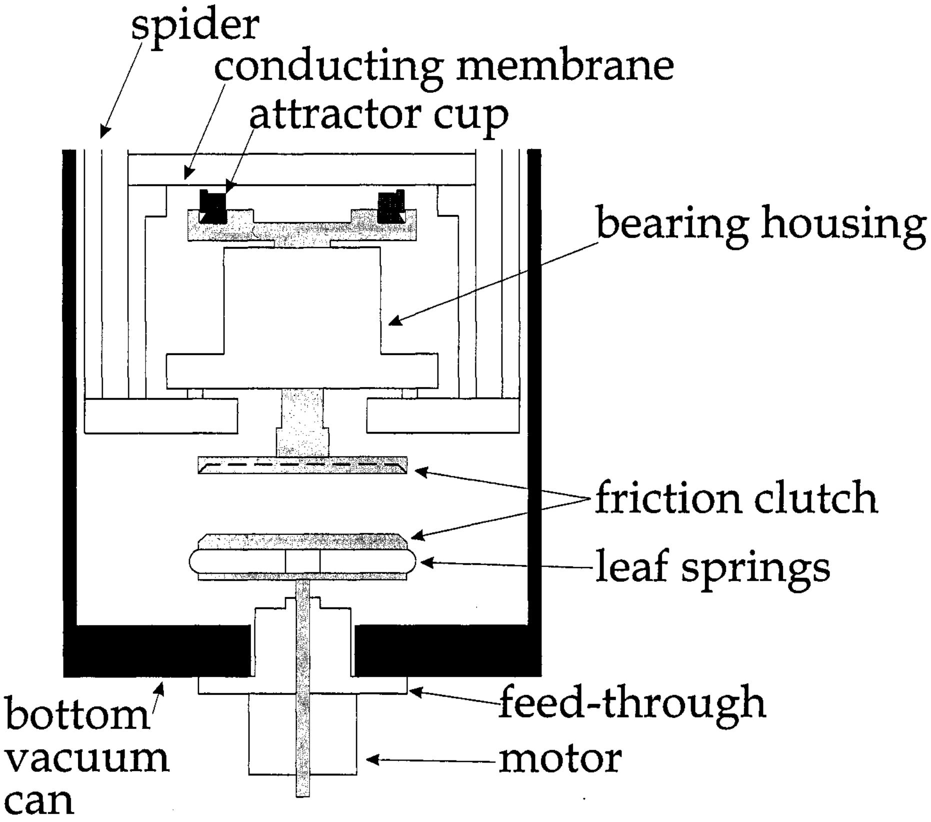

Figure 2.11: A cut-away view of our rotating attractor assembly. The spider is hanging from the upper vacuum can (not shown) and the bottom vacuum can is shown lowered so that the friction clutch is not engaged.

2.5.1 Motor, Vacuum Feed-Through, and Friction Clutch

The motor and vacuum feed-through were as described in [35], with some improvements. A second bearing was added to the rotary vacuum feed-through, so that any wobble or side-to-side motion of the shaft was removed, reducing the amount of mechanical feed-through from the motor into our optics. Eliminating these motions also improved the integrity of our rotary O-ring vacuum seal, reducing the frequency of pressure spikes. The motor was attached to this constrained shaft via a flexible coupler so that any inherent misalignment in the motor or its mount did not cause mechanical stress. The motor was still mounted to the bottom of the lower half of the vacuum vessel, but had intermediate rubber feet that served as vibration and thermal isolation from the rest of the vessel. In doing so, we were able to remove water cooling lines to the motor which presented interference problems with our calibration turntable. With this improvement, we could also remove the motor without breaking the vacuum. We added an additional layer of magnetic shielding around the motor, to reduce any possible magnetic coupling to the pendulum.

The friction clutch was as described in [35] except that we replaced coil springs which pushed the two sides of the clutch together, while allowing for slight misalignments, with leaf springs to make the clutch stiffer torsionally. The upper plate of the friction clutch had a small tab on it that passed between an LED and a photodetector once per revolution of the attractor, to provide us with an angular index mark.

2.5.2 Bearing and Attractor Mount

In contrast to previous iterations, we used a larger, 15mm diameter, titanium shaft as the shaft of the rotating assembly. We heat-shrunk a titanium disk onto this precision ground shaft and then, by mounting the shaft directly into a lathe, machined the platter such that its faces were perpendicular to the shaft axis. The larger diameter of the shaft improved the uncertainty of this lathe mounting. Angular-contact bearings, with ceramic balls and non-magnetic Stellite races were mounted opposite each other in a common bore through a stainless steel housing to prevent any possible misalignments of the two bearings. The loading on the bearing assembly could be adjusted; different loadings showed a tradeoff between the wobble and rumble of the assembly and the angular stiffness, all of which we wanted to minimize. These bearings operated in vacuum with no lubrication, and so, an excess loading of the assembly could lead to a non-uniform rotation rate or, even worse, a seizing. But, a wobble or rumble could lead to a signal modulation that would be difficult to model. We adjusted the loading of the bearing assembly until the wobble and rumble of the titanium platter were at or below our 1μm indicator resolution. With this loading, the assembly rotated smoothly, without any risk of seizing.

We held the attractor rings in a copper ring with a small bead of Torr-Seal epoxy. This copper ring fit into a recess in the titanium platter of the bearing assembly. This platter held small brass adjustment screws that allowed both vertical and axial adjustments of the copper cup to align the attractor ring to the rotation axis of the bearing. The only moving ferromagnetic parts of this assembly were the small stainless steel vacuum feed-through shaft and bearings, ≈ 15 cm below the pendulum and parts of the motor/reduction assembly, even farther below the feed-through.

2.5.3 Alignment of the Attractor Ring and the Bearing Rotation Axis

The bearing assembly described in Section 2.5.2 had no measurable wobble or rumble when tightened (at the 1μm level). We then had to ensure that the axis of rotation passed through the centers of the hole arrays in the attractor rings.

The two attractor rings were glued together while held in a precisely-machined alignment jig. The jig was made by first lapping two pieces of 0.5 in. thick aluminum, and then sandwiching them together to be machined simultaneously. The jig had three sets of three holes, machined by the same EDM which machined our active mass rings. The first set of holes matched the dimensions of the outer radius (R_2) of the upper attractor ring, but with three holes rather than 21. The second set matched the dimensions of the bottom attractor ring. The final set of holes were at a radius outside the O.R. of the two attractor rings, and served to index the two jig plates together. Once machined, the plates were separated. One jig plate had alignment pins placed in the first set of holes, while the other had pins placed in the second set. The two attractor rings could then be mounted onto the two jig plates separately and the third set of holes aligned the two plate/rings in the correct orientation. Because all sets of these alignment holes were made at the same time, we benefited from the full accuracy of the EDM (removing and remounting a piece sacrifices precision.) Measurements of this jig showed that the outer hole array of the top attractor and the array of the lower attractor would be concentric within 2.5μm. Once the two rings were held together in the jig, we applied a small bead of Torr-Seal on the outer edge where they met to hold them in place.

Once glued together, the two rings were glued into a copper cup which was then placed in the rotating titanium plate. Three brass screws determined the horizontal position of the copper cup in the titanium plate. Three more screws advanced on the copper cup from below. These two sets allowed for runout and "wobble" adjustments respectively, both of which were set to $\leq \pm 2.0\mu$m. Locking nuts were added so that the positioning did not slip and six dummy screws were added after these adjustments, so that the gravitational moments of the attractor holder were $m = 6$ and not $m = 3$. Because the pendulum had an accentuated $m = 3$ moment, we avoided that symmetry in our attractor assembly to prevent unwanted gravitational signals.

When we aligned the combined rings to the bearing axis, we indicated on the outer diameter of the upper attractor ring and adjusted until the runout, as the ring rotated in the bearing, was below 2μm. Inspection of the attractor rings with a measuring microscope and also a coordinate measuring machine showed that the outer diameters (O.D.) and the hole arrays were concentric within 8 ± 1 μm. Thus, we knew the hole arrays were concentric with the bearing axis within ≈ 10 μm. Section 5.3.6 describes the sensitivity of our signal to this alignment.

2.5.4 Alignment of the Attractor Ring and Bearing to the Membrane

Once the attractor was coaxial and wobble-free relative to the bearing axis, the entire assembly could be tilted - to make the attractor ring parallel to the screen - and translated - to vary the separation, d, between the ring and the screen. d was measured mechanically and capacitively and can be seen in Figure 2.1. The screen and attractor plates were set at an average separation of 192±2 (12±1) μm for the upper-attractor-only (both attractor) data runs.

2.5.5 The Conducting Membrane

A 10μm thick Be-Cu foil with a thin layer of gold on the pendulum-side electrically isolated the detector and attractor rings. (The raw material for the membrane was acquired from Goodfellow Corporation. We have also had recent success with material from Micro-Tek Associates Inc. Diamond Bar, CA.) We sputtered $\approx$ 1500 Å of gold onto the foil and then placed it between two lapped 0.45 inch thick aluminum rings. The rings were held together loosely with bolts, and the entire assembly was submerged in liquid nitrogen. Once cold, the bolts were tightened and the subsequent warm-up to room-temperature pulled the foil tight, due to the differential thermal expansion of Be-Cu and aluminum. Using a speaker and a function generator, we found the first resonance of the membrane to be $\approx$ 1.6 kHz.

We built a Fizeau interferometer so that we could observe the deformation of the membrane as it was during the experiment, with no direct contact between a reference flat and the membrane. The interferometer consisted of a HeNe laser, beam expander, collimating lens, beam splitter and optical flat that we mounted vertically on a $\approx$ 2 m high aluminum structure. The entire attractor and membrane assembly was placed at the base of this structure. The optical flat was mounted on both a gimbal and a translation stage to adjust its relative alignment to the membrane. Through the beam splitter, we obtained an image of the membrane with interference fringes superimposed on it. The fringes arose from the interference of the laser reflections from the membrane and the optical flat. The optical flat was known to be flat to $\frac{\lambda}{10}$ and thus any deviation from parallel fringes (due to an angle between the flat and membrane) indicated surface deformation of the membrane. The deviation from parallel lines was less than 2 fringes and thus the membrane varied $\leq 2\mu$m over its $\approx$ 53cm^2 of exposed area.

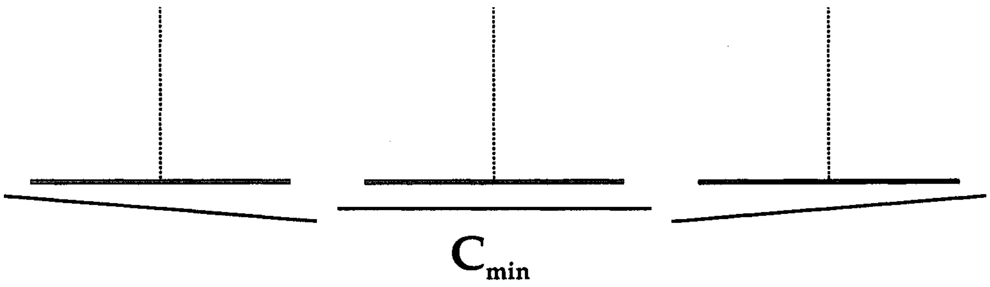

Figure 2.12: A schematic of the method used to align the membrane and detector ring. We measured the capacitance as a function of apparatus tilt and found the minimum to set the two pieces parallel.

2.5.6 Alignment of the Attractor/membrane to the Detector Ring

After the attractor-membrane assembly was aligned, it was mounted into the apparatus beneath the now-horizontal pendulum ring. The pendulum was lowered until a sizable capacitance (> 100 pF) was measured between the pendulum and membrane. Then, by turning the leveling screws of the entire apparatus, we measured the capacitance as a function of tilt. An apparatus tilt changed the angle of the attractor-screen relative to the pendulum. The capacitance is an even function vs. the angle between two plates, and the minimum should occur where the two plates are parallel. Figure 2.12 shows a schematic of this leveling scheme, while Figure 2.13 shows data from one of these measurements. The pendulum and screen were leveled to < 20 (16) μradians, and the attractor and detector rings were then parallel to better than 130 (70) μradians for the upper-attractor-only (both attractor) data runs.

2.5.7 Pendulum Housing

A cylindrical magnetic shield covered the entire bearing assembly and membrane rings and had a small lip that let the cylinder seat on top of the membrane rings. A second gold-plated magnetic shield formed a nearly complete Faraday cage around the pendulum. There was a small hole in the side for the laser to enter and leave and a small hole on top for the fiber and thermal shroud. The upper magnetic shield replaced an earlier version that was solely

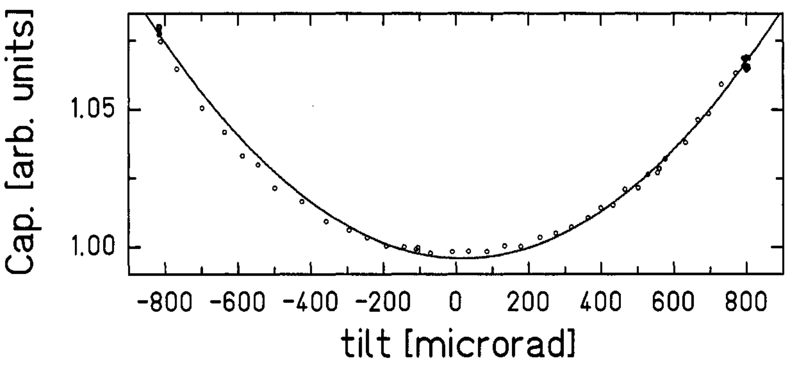

Figure 2.13: Data from the procedure shown in Figure 2.12. The tilt was monitored with a Applied Geomechanics tilt sensor, as described in [35].

electrostatic.

2.6 Determining the Vertical Separation Between the Detector Ring and Conducting Membrane

The vertical separation between the pendulum and the attractor rings was an extremely important parameter in our experiment. This separation was composed of the distance between the attractor and the screen, d, the thickness of the screen, t_s, and the separation between the pendulum ring and the screen, z. These contributions are shown schematically in Figure 2.1. As mentioned in Section 2.5.4, d was measured both mechanically and capacitively, while t_s was measured mechanically. Determining z was more involved.

Our $\pm 1\mu$m readout on the z micrometer of the pendulum suspension was sufficient resolution for telling us *relative* displacements between different data runs, but it told us nothing of the *absolute* position relative to the membrane. To determine the position of the membrane, z_0, we measured the capacitance between the membrane and pendulum vs. micrometer reading with a Stanford LCR meter, model SR720. By comparing there measurements with a finite-element calculation, we could determine z_0. Our finite-element calculation was performed in the program FEMLAB, and took account of the geometry of

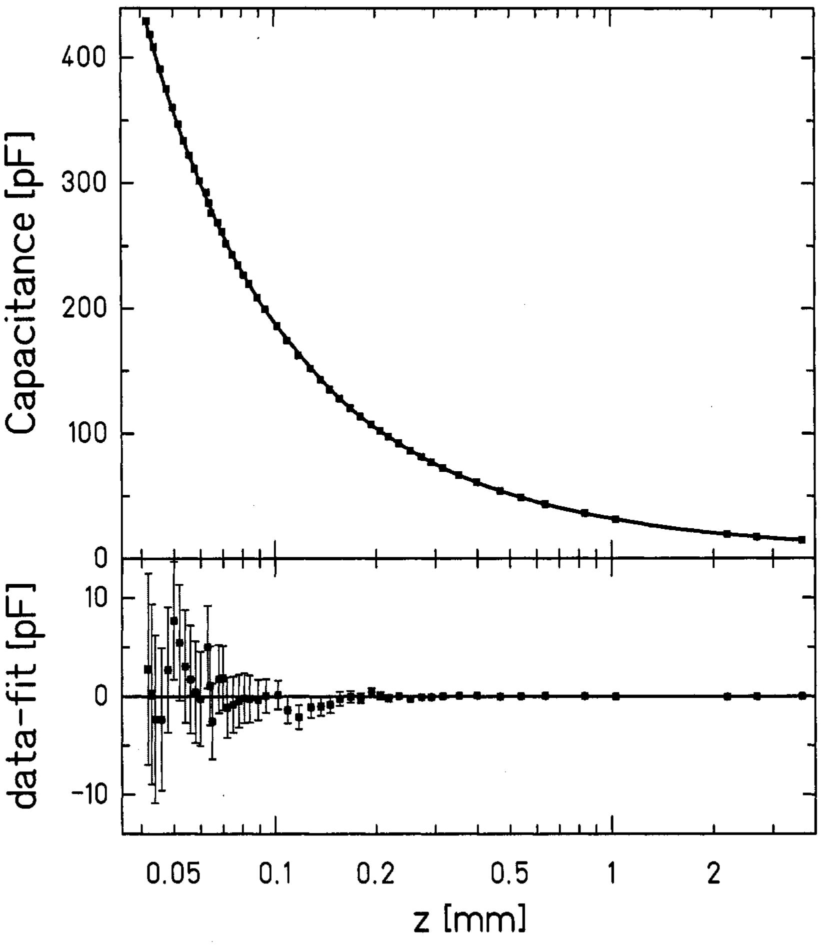

Figure 2.14: A fit to our measured capacitance between the pendulum and the conducting membrane as a function of micrometer reading. The solid line is a finite element calculation and the residuals are shown below. There are actually two sets of error bars in the residuals : the first set, which is smaller than the size of the points, comes from the error on the capacitance measurement; the second set, which are more obvious, comes from the resolution of our micrometer and increased with the slope of the capacitance curve.

the pendulum and the surrounding shield can. Figure 2.14 shows a fit to our measured capacitance with this calculation. From this fit, we could infer z and δz for a given C and δC. For data runs where C was small and not very sensitive to position, we measured a C at some close separation, z_c, and then recorded the difference in the z micrometer between this z_c and the actual z of the data run. The error inherent in this procedure was taken into account in the final uncertainty in s for each run. We could not just use the z-micrometer reading for these far-away runs, because we discovered that the fiber, or the small copper bellows from which it hung, was stretching by about 1 μm per day. For data runs where z was small, this fit was more sensitive than our micrometer in determining z.

Chapter 6 discusses how we accounted for these errors in our fit of the data set.

2.7 Data Acquisition and Experimental Sensors

Data in this experiment was recorded by the same 80286 computer with an Analogic LSDAS-16 interface card as used in [35]. Each of the 16 channels of this card had 16-bit analog to digital conversion that read the analog sensors of the apparatus. A data sample was typically recorded approximately every 4 seconds, and each sample was the average of 20 subsamples, taken approximately every 0.2 seconds. Section 3.3 describes the exact timing. This card supported some digital communication. One of these digital lines was used to interface with the temperature sensor multiplexer, which cycled up to 16 temperature sensors through a single analog-to-digital channel. One digital line was used to count the number of subsamples that had passed since the motor was last calibrated (where we defined the angle of rotation to be zero as the once-per-revolution index passed.) This counter let us reconstruct the angle of the attractor drive; section 5.3.1 discusses this angle in more detail.

The data acquisition software which controlled this Analogic interface card, a National Instruments PCI-GPIB card, and the COM ports of the 80286 was written in Microsoft Visual C++. The PCI-GPIB card was used to set the time constants and gains of the lock-in amplifiers used in recording the angle of the pendulum (see [35]) as well as the three function generators, Stanford Model DS345, whose TTL outputs served as the subsample clock, and the clocks for the attractor and turntable stepper motors. The three function generators shared a single time base. The COM ports communicated with the stepper motor controller and digital encoders of Section 2.3.3, as well as the LCR meter.

The pendulum twist was monitored with the same autocollimator and lock-in amplifiers of Reference [35].

The tilt, seismic, and temperature sensors were the same as [35], except that three additional temperatures sensors were added, to record the temperature of our system during bakeout.

The pressure was monitored by a Balzers-Pfeiffer PKR-230 compact full-range gauge, which was controlled by a Balzers-Pfeiffer TPG-251 total pressure controller whose analog output was read into one of our analog to digital inputs. This gauge was mounted directly onto the turbo pump, where the pressure was $\sim 5\times10^{-7}$ torr for the entire data set. A second gauge was mounted directly onto the apparatus. At our running pressure, the pressure at the apparatus was $\approx 10\times$ that at the turbo pump. Because the gauge on the apparatus seemed to increase the overall pressure, and to disturb the pendulum when switched on, we opted to only monitor the gauge on the pump itself.

2.8 Vacuum Vessel, Support Frame and Shielding

Our vacuum vessel was described in Reference [35]. Previous experiments were plagued with periodic spikes in the apparatus pressure, due to either a discharge within the ion pump or long-channel leaks within the apparatus. To eliminate the first possibility, we replaced our ion pump with a turbo-molecular pump (Balzers-Pfeiff TMU-065). We eliminated vibration from the turbo and the accompanying roughing pump (Balzer-Pfeiffer DUO-004B) as follows. The roughing pump sat on the lab floor and was connected via a long loose hose to the turbo, on a separate platform. The turbo was connected to a flexible vacuum bellows to a pipe that was clamped firmly to the cyclotron wall between two lead blocks. This pipe was then connected to another flexible hose that passed into the thermal enclosure and attached to the apparatus. We saw no increased noise with the new turbo system in place. The vacuum spikes were still prevalent and were eventually brought under control with close inspection of all O-ring surfaces for scratches and dirt and a remake of the vacuum feed-through as described in Section 2.5.1. We kept the turbo system as it was more convenient. After our switch to the turbo pump, Reference [37] found that ion pumps increase the amount of free charges in the vacuum, something we gladly avoided.

Chapter 3

DATA TAKING AND ANALYSIS

There were three types of data runs in this experiment. The *sweep runs* were used to assess and correct for nonlinearities in our photo-detector and optical path. The *alignment runs* were used to align the calibration spheres with the pendulum spheres. The *data runs* were the main measurements of this experiment, where we measured the torque on our pendulum as a function of separation from the rotating attractor.

3.1 Sweep Runs

Because we measured several harmonics of our torque signal, we wanted to correct for nonlinearities in our angular readout which could give us false power at higher harmonics. We stopped our attractors from rotating and let the pendulum swing freely with no applied torque, with enough amplitude to sweep across the same angular region of the detector where our data was taken. We used the linearity of our torsion oscillator to check and correct for non-linearity in our angular read-out. This correction, applied at each unique pendulum position, accounted for any mirror curvature or other properties of our optical path that might vary as the pendulum moved relative to the rest of the optical path.

We were confident that our oscillator was linear by considering the inherent nonlinearity in the fiber and the nonlinearity we expected from the gravitational gradients at the pendulum.

Reference [38] measured the inherent non-linearity of tungsten fibers, due to inelasticity, the source of our thermal noise. The equation of motion (neglecting viscous damping) of a non-linear torsion oscillator acquires an additional term

$$I\ddot{\theta} + \kappa\theta + \kappa_3\theta^3 = 0 \tag{3.1}$$

and the approximate solution is

$$\theta(t) \approx Ae^{i\Omega t} + \frac{\kappa_3}{32\kappa} A^3 e^{i3\Omega t}. \tag{3.2}$$

Reference [38] found that $|\frac{\kappa_3}{\kappa}| = 0.026\ \mathrm{rad}^{-2}$ for a tungsten fiber very similar to ours. During our sweep runs, a typical angular amplitude was tens of μradians. Even with an amplitude of 1×10^{-4} radians, the amplitude of the non-linear portion of the oscillation is $< 10^{-15}$ radians, six orders of magnitude below our angular resolution.

Local gravitational potentials could also produce a non-linear oscillation of our pendulum. The pendulum body was designed to have an accentuated $m = 3$ moment, and the detector ring had accentuated $m = 21,\ 42$, and 63 moments. During the sweep runs, our motors were not turning and these static attractors contributed to the restoring potential of our pendulum. These torques varied sinusoidally with angle,

$$N_m(\phi) = A_m \sin(m\phi + \gamma) \tag{3.3}$$

where ϕ is the relative angle between the detector and attractor, and γ is some arbitrary phase. While our attractors were rotating, ϕ was simply a measure of time, which induced angular oscillations of the pendulum. While the attractors were "parked", the variation of the torques over the pendulum's oscillation amplitude provided an additional potential well. We can expand Equation 3.3 for small angles ϕ

$$N_m(\phi) \approx A_m \sin(\gamma) + (A_m m \cos(\gamma))\,\phi - \left(\frac{A_m m^2}{2} \sin(\gamma)\right)\phi^2 + O\,[\phi^3]. \tag{3.4}$$

The first term of Equation 3.4 produced a shift in the equilibrium position of the pendulum, the second term contributed a symmetric restoring torque, analogous to the fiber's, and the third term was the first contributing nonlinear term.

Our signal amplitudes, A_m were all less than 10 fNm, so, using the nominal value, $\kappa = 3.11$ fNm/μrad, our equilibrium angle could be expected to vary, depending on the parked angle of the attractor, γ, by up to 3 μrad. A change of this scale was usually obscured by the drift of our equilibrium position with time. The symmetric term contributed at most (for m=63) a spring constant, $\kappa_G \leq 6.3 \times 10^{-4}$ fNm/μrad; this term could change the natural period of our oscillation ($\approx$500 seconds) by up to 0.05 seconds, a small effect. For an angular amplitude of 1×10^{-4}radians, larger than any in a *sweep* run, the third term would contribute an anomalous angular deviation of 6×10^{-2} nrad, well below our angular resolution of ≈ 1 nrad. We could safely park our gravitational attractors at arbitrary positions without affecting our *sweep* runs.

We did see a variation of our pendulum's equilibrium position with height, likely due to some localized electrostatic interaction with the conducting membrane. Unlike the gravitational potentials of the preceding paragraph, the electrostatic ones would not change when the attractors started rotating, thus our corrections for nonlinearities would also compensate these local potentials. We can get a rough idea of the scale of the local potentials by noting that the equilibrium position of the pendulum shifted by ≈ 175 μrad at separations closest to the conducting membrane, while the natural period was seen to change by ≈ 1.5 seconds. Using the first two terms of Equation 3.4, we can estimate $A_m \approx 500$ fNm and $A_m m \approx 2 \times 10^4$ fNm/rad. Using our overestimate of 10^{-4} radians of amplitude, gives $m \approx 2$. which says the electrostatic potential varies with characteristic angular scale of π, or a length scale of $\approx$ 10cm.

Given these considerations, we were confident that we could use the natural oscillation of our pendulum, with our attractors parked, to check and correct for nonlinearities in our readout or local electrostatic potentials. Our photodetector had two outputs, currents from either side of the detector. For an ideal system, the angle of deflection, $\theta = c_0 \frac{\Delta}{\Sigma}$, where Δ and Σ are the difference and sum of the two currents respectively, converted into voltages and amplified, and c_0 converts this ratio into angle. For a sweep run, the Δ and Σ signals from the detector were converted into an angle with the power series

$$\theta = c_0(\frac{\Delta}{\Sigma}) + c_1(\frac{\Delta}{\Sigma})^2 + c_2(\frac{\Delta}{\Sigma})^3 + c_3(\frac{\Delta}{\Sigma})^4 \tag{3.5}$$

where the c_i are some nominal values. We then fit θ to a damped sine wave, $\theta_0 = D(t) + A\sin(\Omega t)e^{-t/\tau}$, where $D(t)$ accounts for a slowly changing equilibrium position with time, and A, Ω, and τ are fit parameters. We then fit the residuals of this fit, $\theta_0 - \theta$ to a power series in θ, that is

$$\begin{aligned} \theta_0 - \theta &= a_0 + a_1\theta + a_2\theta^2 + a_3\theta^3 + a_4\theta^4 \\ \theta_0 &= a_0 + (1 + a_1)\theta + a_2\theta^2 + a_3\theta^3 + a_4\theta^4. \end{aligned} \tag{3.6}$$

Substituting Equation 3.5 into Equation 3.6 and grouping the terms with the same powers of $\frac{\Delta}{\Sigma}$ gives new values of c_i in terms of the original c_i and the coefficients a_i. We repeated this procedure several times, with updated c_i, to converge on the values of c_i that minimize the residuals to the fit. Figure 3.1 shows the effects of this procedure in the angular power spectral density. Once we determined the correct values of c_i, we used those same values to convert our Δ and Σ signals into angle for the data run at the same pendulum position.

3.2 Alignment Runs

Alignment runs were runs where only the calibration turntable was turning. We used these runs to center the calibration spheres vertically and axially on the pendulum spheres. We conducted all of these runs at the same pendulum position, so that the nonlinearities never varied. Once the calibration turntable was centered, we followed any pendulum movement in (x, y, z) with an identical calibration table movement, so that their relative position never varied. The calibration procedure is described in Section 2.4. The procedure for analyzing the calibration runs is identical to that described below for data runs, except that, in these runs, we analyzed our data relative to the rotation angle of the calibration turntable.

3.3 Data Runs

Data runs were the main component of our data set. Each data run was a measurement of the angular oscillations of the pendulum at a given position relative to the rotating attractor. The procedure for taking a data run was

1. Moved the pendulum to the desired position in (x, y, z), and centered its angular position, θ on the detector.

2. Measured the capacitance between the pendulum and the conducting membrane. For runs that were far from the membrane, we translated to a lower z_c, measured the capacitance, translated to the desired z and recorded the difference $z - z_c$.

3. Started the rotation of the attractor and the calibration turntable.

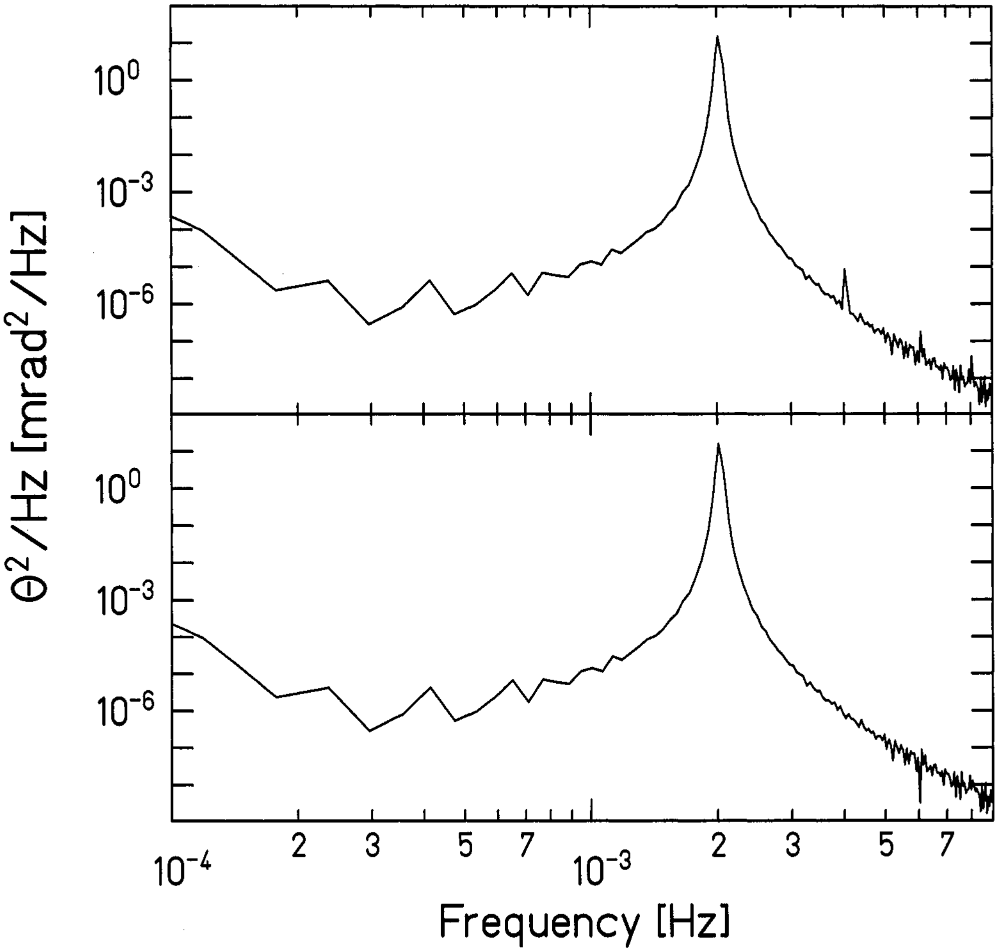

Figure 3.1: The power spectral density for one of our *sweep* runs with no linearity corrections (upper panel) and after using the linearity of the oscillator to correct for nonlinearities in the readout (lower panel). Note the false harmonics of the natural resonance in the upper panel.

4. Took data.

5. Measured the capacitance.

6. Stopped the rotation of the attractor and the calibration turntable.

7. Took a sweep run at the same (x, y, z).

8. Measured the capacitance.

During each data run, a data point was recorded 120 times during each free torsion oscillation ($\approx$ 4 sec per point), with each point representing an average of 20 evenly spaced subsamples in the preceding 4 second interval. The free torsion had a period of $\tau_0 \approx$ 500 seconds. We set the attractor rotation rate so that its period of rotation, $\tau_a = 28\tau_0$: a full revolution of the attractor took $\approx$ 4 hours. We set the period of rotation of the calibration turntable, $\tau_c = 3\tau_a/m_c$ where m_c was initially set to 49 and later to 35. We changed the rotation rate of the calibration turntable between run2005 and run2007, which were taken at the same pendulum position; one can see from Table 3.2 that these runs agreed very well. We referred to the different frequencies in our data set relative to the rotation frequency of our attractor, ω. The free torsion occurred at 28ω; our torque signals occurred at 21ω, 42ω, and 63ω; and the calibration signal occurred at $m_c\omega$.

We converted our Δ and Σ autocollimator signals into an angle using the linearity coefficients described in Section 3.1 and Equation 3.5. We filtered out the natural resonance of our pendulum with a notch filter, as described in [35]. We cut the filtered run into "subcuts" of time duration $\tau_a/7$, and fit θ to

$$\theta_{fit}(\phi) = \sum_m [b_m \sin(m\phi) + c_m \cos(m\phi)] + \sum_{n=0}^{n=3} d_n P_n \tag{3.7}$$

where the sum over m ran over $m = 21, 42, 63$, and m_c and the second term accounted for a drift in the equilibrium position of the pendulum during the subcut. Figure 3.2 shows a typical full revolution of the attractor (7 subcuts) and its residuals.

We rejected subcuts where the χ^2 of the fit to Equation 3.7 was anomalously large, as described in [35]. These bad fits were a result of some outside disturbance to our pendulum.

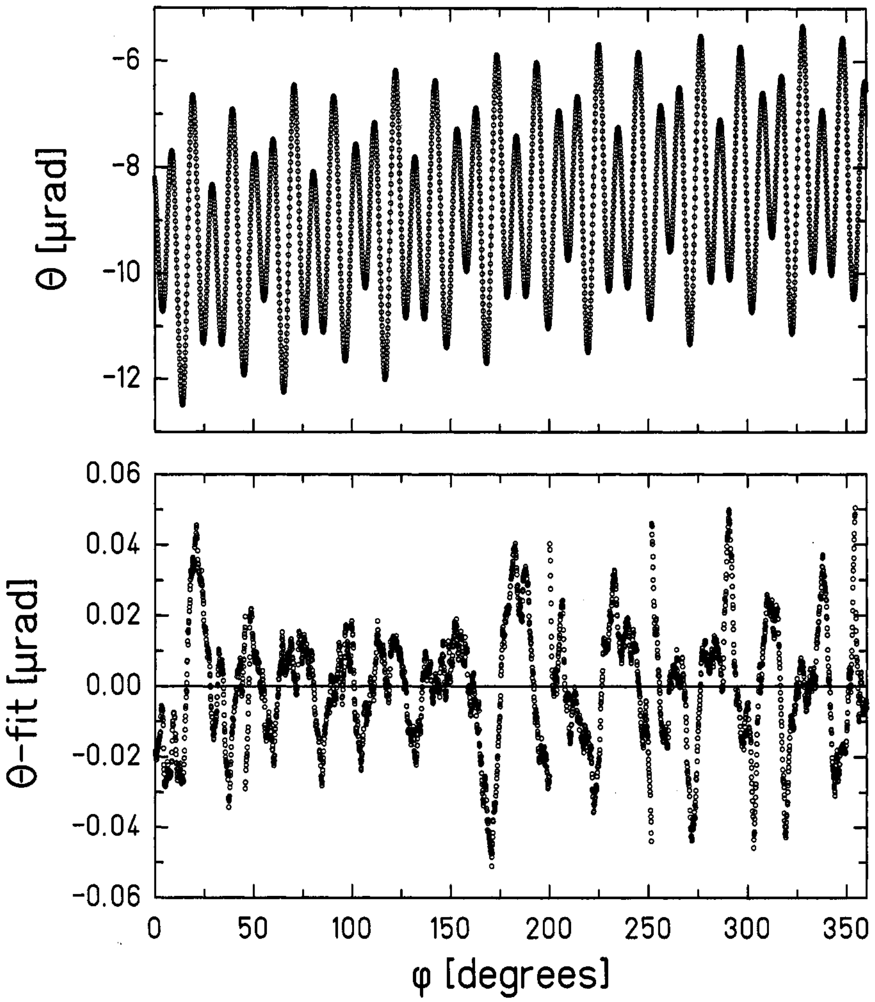

Figure 3.2: A sample segment of data from one full attractor revolution (7 subcuts of run1993). The data and fit are shown in the upper panel while the residuals are shown in the lower panel. This data has had the natural period of the pendulum filtered and has not been corrected for pendulum response, averaging, or lock-in filtering.

There were 1611 subcuts in our entire data set with 286 of those rejected. The rejections were concentrated where the pendulum was close to the conducting membrane: where $z <= 50$ μm 145 of the 379 subcuts were rejected.

We checked that our residuals at our three signal frequencies were Gaussian by calculating the normalized quantities

$$r_i = (a_i - \overline{a})/(\sqrt{N}\sigma_i) \tag{3.8}$$

where i indicates one particular subcut of a run, $a_i \pm \sigma_i$ is the measured in- or out-of-phase angular deflection of the pendulum for that subcut, $\overline{a} = (\sum_i^N a_i)/N$ is the mean value of that deflection for that entire run, and N is the number of subcuts in that run which survived our χ^2 rejection criteria. We binned all of these r_i for the three harmonics separately and fit them to Gaussians; the results are shown in Figure 3.3.

The remaining subcuts were averaged and corrected for the frequency response of our oscillator, the averaging of our data sampling, and the attenuation from time constants on our lock-in amplifiers. (All of these procedures are covered in detail in Reference [35].) After this analysis, we were left with b'_m and c'_m, the in- and out-of-phase components of an equivalent static angular deflection of our torsion pendulum for each signal frequency, and the statistical errors σ'_{b_m} and σ'_{c_m}, which are the errors of the means of our subcuts.

Finally, we converted each of these angular signals into torques by first calculating the equivalent static angular amplitude of the calibration signal and its corresponding error,

$$\begin{aligned} A_c &= \sqrt{b'^2 + c'^2} \\ \sigma_c &= \frac{1}{A_c}\sqrt{b'^2\sigma_b'^2 + c'^2\sigma_c'^2} \end{aligned} \tag{3.9}$$

where, for the sake of clarity, I have left off the subscripts indicating that the angles used here are those that occurred at $m_c\omega$, the frequency of the calibration signal. The angular

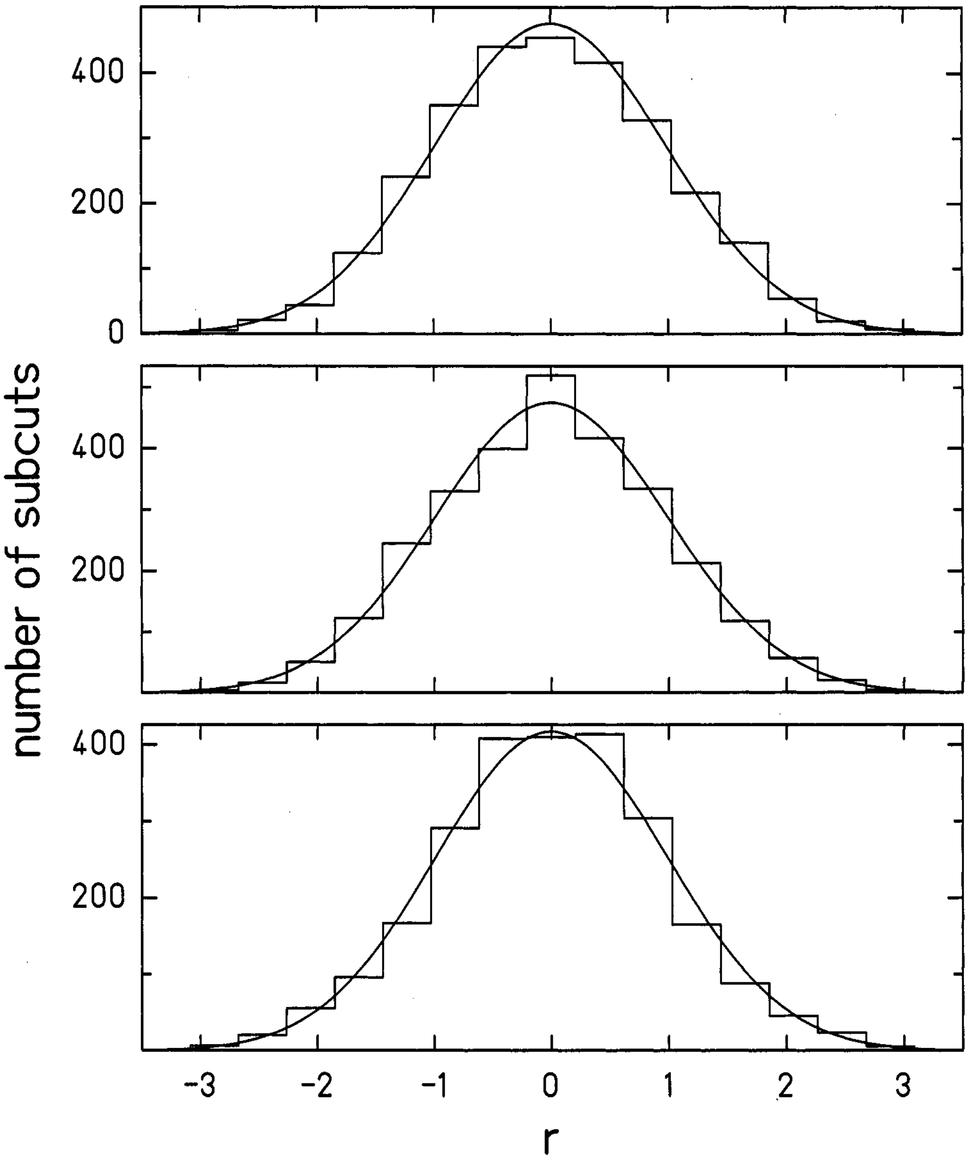

Figure 3.3: The normalized residuals (Equation 3.8) and Gaussian fits for both components of all subcuts included in our data set. The upper, middle and lower panels show r for the frequencies 21ω, 42ω, and 63ω. There were several runs where we ignored the 63ω signal, and those runs have not been included in the lower panel.

signals and errors at frequencies $m = 21,\ 42,$ and 63 were then converted into torques

$$\begin{aligned}
\beta_m &\equiv b'_m \frac{N_c}{A_c} \\
\gamma_m &\equiv c'_m \frac{N_c}{A_c} \\
\sigma_{\beta_m} &= \sqrt{(\beta_m \sigma_{b'_m}/b'_m)^2 + (\beta_m \sigma_c/A_c)^2} \\
\sigma_{\gamma_m} &= \sqrt{(\gamma_m \sigma_{b'_m}/b'_m)^2 + (\gamma_m \sigma_c/A_c)^2}.
\end{aligned} \tag{3.10}$$

where N_c is the calculated value for the calibration torque as discussed in Section 2.4.

We conducted a series of data runs (run1846 through run1914) with only the upper attractor; we took this data to independently constrain fit parameters relevant to the upper attractor plate. The two-attractor data runs began with run1993. The data runs spanned the time period May 6th through September 7th, 2004.

Table 3.1 lists the pendulum positions in all our data runs, while Table 3.2 lists the quantities β_m and γ_m for all the runs.

Table 3.1: Positions of data runs. x-mic and y-mic are the micrometer readings of the indicators on the x and y axes; z is the inferred height above the membrane from the capacitance measurements and σ_z is the error on that position. All units are in millimeters.

Run Name	x-mic	y-mic	z	σ_z
run1846	-0.497	1.456	2.840	0.005
run1848	-0.497	1.456	2.840	0.005
run1851	-0.496	1.456	2.840	0.005
run1855	-0.496	1.456	2.840	0.005
run1857	-0.496	0.005	2.840	0.005
run1859	-0.498	2.932	2.840	0.005
run1860	-1.694	1.450	2.840	0.005
run1862	-0.719	0.003	2.840	0.005
run1864	-0.496	1.456	1.882	0.002
run1866	-0.496	1.456	2.379	0.004
run1869	-0.496	1.456	2.876	0.001
run1871	-0.496	1.456	3.375	0.002

continued on following page

Table 3.1 continued.

Run Name	x-mic	y-mic	z	σ_z
run1873	-0.496	1.456	3.873	0.002
run1875	-0.496	1.456	3.873	0.002
run1876	-0.496	1.456	4.373	0.002
run1878	-0.496	1.456	5.374	0.002
run1881	-0.496	1.456	6.373	0.002
run1883	-0.496	1.456	8.373	0.002
run1885	-0.496	1.456	12.372	0.003
run1887	-0.496	1.456	2.383	0.002
run1890	-0.496	1.456	0.974	0.003
run1892	-0.496	1.456	0.974	0.003
run1909	-0.496	1.457	2.382	0.002
run1912	-0.495	1.457	0.768	0.002
run1914	-0.494	1.458	0.766	0.002
run1993	-0.272	-1.349	0.123	0.002
run1995	-0.270	-0.848	0.123	0.002
run1997	-0.274	0.859	0.123	0.002
run1999	-1.475	-0.153	0.124	0.001
run2001	-1.224	-0.151	0.124	0.002
run2003	0.535	-0.145	0.124	0.001
run2005	-0.418	-0.310	0.124	0.001
run2007	-0.418	-0.310	0.124	0.001
run2008	-0.418	-0.310	4.998	0.002
run2010	-0.418	-0.310	3.998	0.002
run2012	-0.418	-0.310	0.039	0.001
run2013	-0.418	-0.310	2.984	0.002
run2015	-0.418	-0.310	0.050	0.001
run2017	-0.418	-0.310	0.880	0.002
run2019	-0.418	-0.310	0.054	0.001
run2021	-0.418	-0.310	0.045	0.001
run2024	-0.418	-0.310	0.040	0.001
run2029	-0.418	-0.310	1.274	0.002
run2031	-0.418	-0.310	0.349	0.002
run2033	-0.418	-0.310	0.091	0.001
run2035	-0.418	-0.310	0.082	0.001
run2037	-0.419	-0.310	0.072	0.001
run2039	-0.419	-0.310	0.039	0.001

continued on following page

Table 3.1 continued.

Run Name	x-mic	y-mic	z	σ_z
run2041	-0.419	-0.310	0.038	0.001
run2042	-0.419	-0.310	1.965	0.001
run2044	-0.419	-0.310	0.210	0.001
run2046	-0.419	-0.310	0.550	0.001
run2048	-0.418	-0.309	8.450	0.001
run2050	-0.419	-0.310	0.044	0.001
run2052	-0.419	-0.310	0.042	0.001
run2054	-0.419	-0.310	0.062	0.001
run2056	-0.419	-0.310	0.048	0.001
run2061	-0.419	-0.310	0.042	0.001
run2062	-0.419	-0.310	0.043	0.001
run2065	-0.420	-0.310	0.042	0.001

Table 3.2: Torque measurements from our data set. The quantities in parentheses are the errors for the quantity to the immediate left. All units are in fNm.

Run Name	β_{21}	γ_{21}	β_{42}	γ_{42}	β_{63}	γ_{63}
run1846	7.287 (0.01)	-2.771 (0.017)	-0.031 (0.008)	-0.033 (0.006)	0.009 (0.007)	-0.011 (0.007)
run1848	7.307 (0.017)	-2.761 (0.024)	-0.028 (0.007)	-0.025 (0.011)	-0.022 (0.013)	0.002 (0.01)
run1851	7.286 (0.008)	-2.794 (0.012)	-0.031 (0.004)	-0.035 (0.004)	0.007 (0.005)	-0.005 (0.005)
run1855	7.301 (0.012)	-2.771 (0.017)	-0.029 (0.008)	-0.037 (0.01)	0.009 (0.006)	-0.002 (0.007)
run1857	5.255 (0.008)	-2.009 (0.011)	-0.011 (0.005)	-0.01 (0.005)	0 (0.005)	0.008 (0.005)
run1859	5.115 (0.036)	-1.925 (0.029)	0.003 (0.025)	-0.007 (0.016)	0.035 (0.025)	-0.022 (0.039)
run1860	5.816 (0.008)	-2.252 (0.011)	-0.021 (0.005)	-0.016 (0.006)	0.002 (0.005)	-0.011 (0.005)
run1862	5.218 (0.009)	-2.002 (0.011)	-0.008 (0.005)	-0.013 (0.005)	0.002 (0.005)	0.004 (0.006)
run1864	15.307 (0.023)	-5.844 (0.019)	-0.09 (0.007)	-0.12 (0.006)	-0.003 (0.006)	-0.009 (0.005)
run1866	10.426 (0.009)	-3.949 (0.017)	-0.062 (0.01)	-0.072 (0.005)	-0.003 (0.006)	-0.014 (0.005)
run1869	7.129 (0.02)	-2.706 (0.014)	-0.029 (0.007)	-0.025 (0.007)	0.003 (0.005)	0.009 (0.006)
run1871	4.83 (0.009)	-1.847 (0.012)	-0.01 (0.004)	-0.014 (0.006)	-0.011 (0.005)	0.003 (0.004)
run1873	3.324 (0.006)	-1.27 (0.009)	-0.022 (0.007)	-0.012 (0.006)	-0.009 (0.008)	-0.001 (0.005)
run1875	3.316 (0.006)	-1.269 (0.008)	-0.013 (0.005)	-0.021 (0.007)	0.004 (0.005)	-0.002 (0.005)
run1876	2.282 (0.006)	-0.867 (0.006)	0.004 (0.004)	-0.011 (0.004)	0.002 (0.004)	-0.002 (0.004)
run1878	1.082 (0.008)	-0.415 (0.008)	-0.005 (0.007)	-0.002 (0.006)	-0.005 (0.009)	0.001 (0.007)
run1881	0.519 (0.007)	-0.2 (0.008)	-0.004 (0.004)	-0.006 (0.006)	-0.008 (0.004)	-0.008 (0.005)
run1883	0.122 (0.008)	-0.046 (0.007)	-0.002 (0.005)	0.005 (0.005)	-0.001 (0.006)	0 (0.005)
run1885	0 (0.008)	-0.005 (0.008)	-0.002 (0.004)	0.011 (0.005)	0.001 (0.004)	-0.003 (0.006)
run1887	10.364 (0.012)	-3.947 (0.018)	-0.061 (0.006)	-0.06 (0.007)	0.003 (0.006)	-0.002 (0.007)
run1890	31.447 (0.023)	-11.945 (0.042)	-0.312 (0.012)	-0.37 (0.012)	0.031 (0.005)	-0.06 (0.005)
run1892	31.523 (0.024)	-11.967 (0.055)	-0.311 (0.014)	-0.348 (0.012)	0.033 (0.008)	-0.067 (0.006)
run1909	10.391 (0.011)	-3.968 (0.017)	-0.044 (0.006)	-0.062 (0.007)	0.005 (0.006)	-0.004 (0.006)
run1912	36.979 (0.032)	-14.103 (0.049)	-0.405 (0.012)	-0.446 (0.012)	0.051 (0.007)	-0.088 (0.009)
run1914	37.079 (0.037)	-13.998 (0.056)	-0.403 (0.017)	-0.458 (0.012)	0.05 (0.006)	-0.084 (0.005)
run1993	0.862 (0.011)	2.763 (0.007)	0.681 (0.006)	0.918 (0.007)	0.043 (0.008)	0.031 (0.009)
run1995	0.479 (0.008)	1.609 (0.006)	0.759 (0.005)	1.031 (0.004)	0.266 (0.008)	0.175 (0.007)
run1997	1.009 (0.011)	3.12 (0.008)	0.63 (0.005)	0.837 (0.004)	0.016 (0.005)	0.004 (0.005)
run1999	0.875 (0.009)	2.801 (0.006)	0.676 (0.007)	0.91 (0.005)	0.036 (0.007)	0.039 (0.007)
run2001	0.661 (0.01)	2.158 (0.008)	0.743 (0.007)	0.995 (0.005)	0.148 (0.007)	0.102 (0.007)
run2003	0.816 (0.012)	2.565 (0.008)	0.701 (0.007)	0.938 (0.005)	0.092 (0.006)	0.107 (0.006)
run2005	0.291 (0.007)	1.102 (0.007)	0.741 (0.006)	1.055 (0.005)	0.432 (0.005)	0.328 (0.006)
run2007	0.299 (0.005)	1.096 (0.006)	0.75 (0.006)	1.038 (0.004)	0.433 (0.007)	0.319 (0.006)

continued on following page

Table 3.2 continued.

Run Name	β_{21}	γ_{21}	β_{42}	γ_{42}	β_{63}	γ_{63}
run2008	0.044 (0.004)	0.142 (0.005)	0.005 (0.004)	0.001 (0.004)	-0.001 (0.006)	-0.007 (0.006)
run2010	0.112 (0.004)	0.334 (0.004)	0.008 (0.003)	0.009 (0.003)	0.001 (0.004)	-0.001 (0.004)
run2012	0.192 (0.034)	0.814 (0.022)	0.82 (0.027)	1.083 (0.027)	0.524 (0.023)	0.404 (0.024)
run2013	0.231 (0.004)	0.695 (0.005)	0.024 (0.004)	0.035 (0.004)	0.005 (0.005)	-0.005 (0.004)
run2015	0.23 (0.012)	0.871 (0.009)	0.8 (0.01)	1.094 (0.007)	0.51 (0.01)	0.375 (0.008)
run2017	0.619 (0.007)	1.95 (0.007)	0.371 (0.005)	0.49 (0.005)	0.09 (0.005)	0.061 (0.005)
run2019	0.255 (0.012)	0.86 (0.015)	0.812 (0.009)	1.075 (0.01)	0.517 (0.012)	0.353 (0.008)
run2021	0.228 (0.011)	0.867 (0.01)	0.802 (0.009)	1.074 (0.006)	0.528 (0.008)	0.357 (0.01)
run2024	0.24 (0.028)	0.836 (0.032)	0.843 (0.023)	1.071 (0.015)	0.6 (0.059)	0.368 (0.055)
run2029	0.565 (0.005)	1.81 (0.005)	0.228 (0.005)	0.323 (0.006)	0.039 (0.005)	0.018 (0.006)
run2031	0.471 (0.007)	1.608 (0.004)	0.625 (0.005)	0.846 (0.004)	0.253 (0.005)	0.184 (0.005)
run2033	0.27 (0.008)	0.999 (0.007)	0.782 (0.005)	1.054 (0.004)	0.476 (0.007)	0.346 (0.007)
run2035	0.283 (0.007)	0.977 (0.006)	0.805 (0.006)	1.048 (0.005)	0.484 (0.006)	0.33 (0.007)
run2037	0.241 (0.005)	0.945 (0.006)	0.782 (0.005)	1.072 (0.004)	0.498 (0.005)	0.361 (0.005)
run2039	0.242 (0.092)	0.953 (0.067)	0.712 (0.085)	1.21 (0.119)	0.531 (0.167)	0.222 (0.159)
run2041	0.288 (0.1)	0.886 (0.068)	0.802 (0.044)	1.087 (0.048)	0.547 (0.061)	0.432 (0.057)
run2042	0.43 (0.006)	1.342 (0.005)	0.101 (0.004)	0.14 (0.004)	0.017 (0.005)	0.009 (0.005)
run2044	0.385 (0.007)	1.331 (0.007)	0.715 (0.007)	0.957 (0.005)	0.365 (0.006)	0.251 (0.006)
run2046	0.576 (0.006)	1.851 (0.006)	0.522 (0.005)	0.697 (0.004)	0.169 (0.006)	0.116 (0.007)
run2048	0.002 (0.006)	0.009 (0.007)	-0.01 (0.006)	0 (0.005)	-0.007 (0.008)	-0.009 (0.009)
run2050	0.239 (0.019)	0.87 (0.02)	0.804 (0.009)	1.09 (0.012)	0.527 (0.013)	0.38 (0.011)
run2052	0.17 (0.022)	0.864 (0.025)	0.778 (0.014)	1.097 (0.01)	0.532 (0.013)	0.409 (0.012)
run2054	0.234 (0.008)	0.916 (0.009)	0.774 (0.01)	1.088 (0.007)	0.491 (0.011)	0.359 (0.011)
run2056	0.249 (0.011)	0.887 (0.012)	0.799 (0.008)	1.081 (0.007)	0.507 (0.009)	0.367 (0.009)
run2061	0.28 (0.032)	0.844 (0.025)	0.814 (0.015)	1.098 (0.018)	0.534 (0.016)	0.338 (0.019)
run2062	0.131 (0.057)	0.917 (0.057)	0.868 (0.058)	1.031 (0.044)	0.596 (0.063)	0.38 (0.05)
run2065	0.158 (0.029)	0.857 (0.024)	0.832 (0.021)	1.022 (0.017)	0.479 (0.018)	0.364 (0.019)

Chapter 4

CALCULATION OF EXPECTED TORQUES

This experiment searched for new physics on top of a well-resolved Newtonian background. We modeled the expected torques for the Newtonian and new-physics potentials; our experimental sensitivities determined the required precision of our calculations. This modeling process consisted of, first, calculating a two-dimensional database of the horizontal force between two cylinders vs. horizontal and vertical separations t and s respectively. For each s in this database, we created a spline interpolation of the horizontal force versus t. Then, for each value of s in our force database, we calculated the harmonic torque amplitudes between arrays of detector and attractor holes at different axial displacements of those arrays, δ, leaving us with a two-dimensional database of the torque amplitudes vs. s and δ. Finally, a two-dimensional interpolation left us with the torque functions

$$\tilde{N}_m(\delta, s) \tag{4.1}$$

for arbitrary δ and s, where m represents the different harmonics of our signal: 21, 42, and 63. Section 6.1 describes how we combine multiple torque functions into one fitting function, to account for the three attractor and two detector hole arrays. The following sections describe the calculation of the functions $\tilde{N}_m$.

4.1 Calculation of Torques

4.1.1 Conventions

We assumed that the detector and attractor rings are perpendicular to the vertical torsion fiber, so that a torque about the fiber axis can only be caused by the component of the force between two holes that is perpendicular to the fiber and tangential to the detector ring, $F_{\mathrm{t}}(t, s)$, where t is the horizontal separation between the centers of the two holes, and s is the distance between the two nearest horizontal surfaces of the two holes. This horizontal force between any two perfectly circular holes is directed along the horizontal projection, t, of the line between their centers, so that the torque exerted on the fiber is

$$N(s) = \sum_{i,j} \vec{R}_i \times \vec{F}_{\mathrm{t}}(|\vec{R}_i - \vec{R}_j|, s) \ , \tag{4.2}$$

where $\vec{R}$ is the horizontal vector from the fiber axis to the center of a hole, i runs over the holes in a detector array, and j runs over the holes in an attractor array. The calculation of $F_{\mathrm{t}}(t, s)$ for the Newtonian and new-physics potentials is described in Section 4.2.

A single hole is referred to as either a detector or attractor hole. An array is one set of 21 holes whose centers share a common radial offset from the center of the ring. A ring refers to all arrays on a particular ring (two for the detector and upper attractor rings, one for the lower attractor ring).

4.1.2 Calculating the Harmonic Torque Database

For the geometry shown in Figure 4.1, the torque about the torsion fiber axis from a single detector/attractor hole pair is

$$\tilde{N}_1(\phi_{\mathrm{d}}, \phi_{\mathrm{a}}, \delta, \phi_\delta, s) = R_{\mathrm{d}}\, F_{\mathrm{t}}(t, s) \frac{t_\perp}{t} \ , \tag{4.3}$$

where $F_{\mathrm{t}}(t, s)$ is the total horizontal force between the holes at a detector-to-attractor vertical separation s; ϕ_d is the angle of the detector hole from some axis; ϕ_a is the angle of that attractor hole from that same axis; δ and ϕ_δ describe the size and direction of the displacement of the attractor rotation axis from the fiber axis; and $t_\perp$ is the component of t perpendicular to R_{d} where

$$\begin{aligned} t_\perp &= R_{\mathrm{a}} \sin(\phi_{\mathrm{d}} - \phi_{\mathrm{a}}) - \delta \sin(\phi_\delta - \phi_{\mathrm{d}}) \\ t &= \sqrt{(R_{\mathrm{a}} \sin\phi_{\mathrm{a}} + \delta \sin\phi_\delta - R_{\mathrm{d}} \sin\phi_{\mathrm{d}})^2 + (R_{\mathrm{a}} \cos\phi_{\mathrm{a}} + \delta \cos\phi_\delta - R_{\mathrm{d}} \cos\phi_{\mathrm{d}})^2} \ . \end{aligned} \tag{4.4}$$

The torque on a detector array from an attractor array at one particular attractor

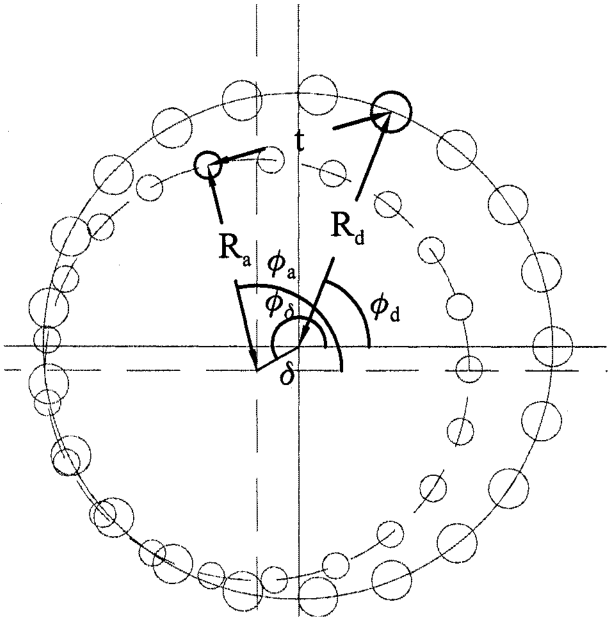

Figure 4.1: Geometry used to calculate the torque on a detector array from a rotating attractor array. The smaller holes are of the attractor array. R_d and R_a are the array radii of the detector and attractor arrays, respectively. ϕ_d, is the angle of the particular detector hole, ϕ_a is the angle of a particular attractor hole which generally includes an overall angle of rotation of the attractor. δ and ϕ_δ indicate the displacement and direction of an axial offset between the detector and attractor arrays, and t is the horizontal separation between the two holes indicated.

rotation angle, ϕ, contains 441 terms,

$$\hat{N}(\phi,\delta,\phi_\delta,s) \equiv \sum_{i=0}^{20}\sum_{j=0}^{20}\tilde{N}_1(\frac{2\pi i}{21},\phi+\frac{2\pi j}{21},\delta,\phi_\delta,s)\ . \tag{4.5}$$

We used a fast Fourier transform of $\hat{N}$ over a $2\pi/21$ interval in ϕ to compute the harmonic torque amplitudes, $\tilde{N}_m(\delta,s)$ at frequencies $m\omega$, for a 10×100 two-dimensional database over δ and s respectively. Figure 4.2 shows the calculated torques on the detector ring from the upper and lower attractor rings for attractor angles between 0 and $\frac{2\pi}{21}$ and a vertical separation of $s = 0.07$ mm. The ranges of the database were chosen to cover the actual range of our data; specifically $0 \le \delta \le 2$ mm, $0.05 \le s \le 13$ mm for the upper attractor ring

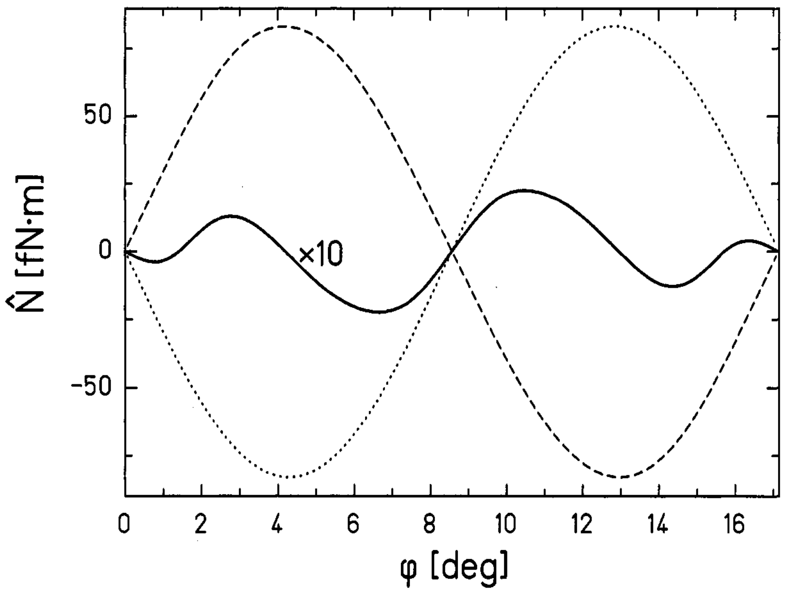

Figure 4.2: Calculated Newtonian torque on the detector arrays at $s = 0.07$ mm ($s = 1.067$ mm for the lower attractor) and $\delta = 0.0$ mm as a function of attractor rotation angle. The dashed and dotted curves are the torques from the upper and lower attractor arrays, respectively. The solid curve is the total torque magnified by a factor of ten.

and $1.047 \leq s \leq 13.997$mm for the lower attractor ring. The tabulated torques were spaced evenly in δ while the points in s were spaced quadratically (closer together near s_{min}) to make the interpolation more accurate where the function was steepest.

We computed the $\tilde{N}_m$ for $\phi_\delta = 0$ and $\phi_\delta = \pi/21$ to determine the sensitivity of the torque to the *direction* of the offset between the two rings; because the results were identical to within 2×10^{-20} N-m, it was sufficient to fix $\phi_\delta = 0$.

4.1.3 Generating Interpolated Torque Functions

We generated torque amplitudes as a function of s and δ by cubic-spline interpolation of the harmonic torque database. Each potential required 12 interpolating functions: one for each of the 4 detector array-attractor ring combinations and 3 for each of the frequencies.

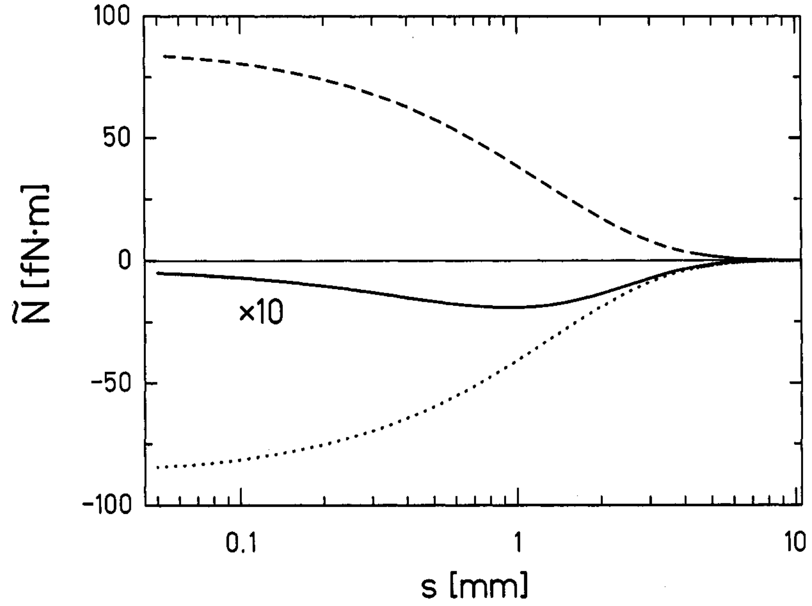

Figure 4.3: Predicted Newtonian 21ω torque on the detector arrays as a function of s. The solid curve shows the total torque multiplied by a factor of 10. The dashed and dotted curves show the torques from the upper and lower disks, respectively.

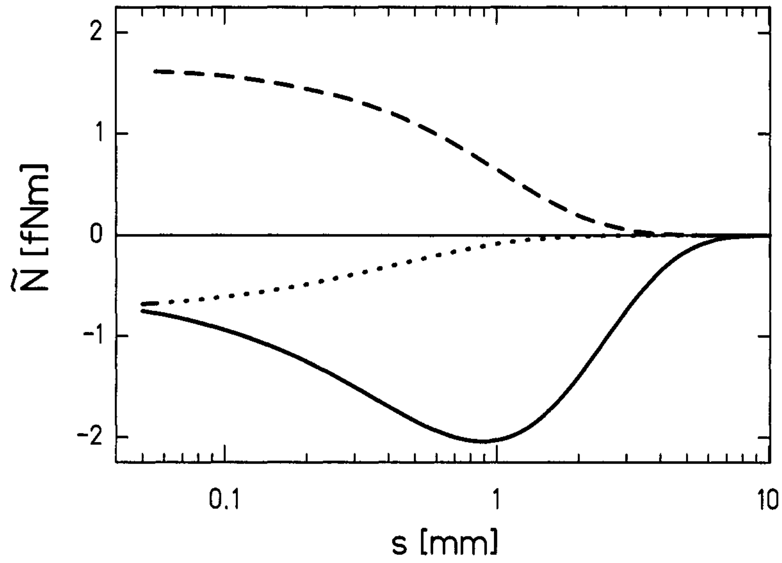

Figure 4.4: The calculated Newtonian torques for $m = 21$ (solid line), $m = 42$ (dashed line) and $m = 63$ (dotted line). Negative value indicates a signal that is in-phase with the lower attractor, while a positive value indicates one that is in-phase with the upper attractor.

We calculated the torque on the inner and outer detector arrays separately to give us the freedom to change the relative position of these two arrays in the fitting function due to a measured deformation of the detector ring; see Section 5.3.4 for a description of this deformation. Figure 4.3 shows the cancelation of the 21ω torque from the two attractor rings for $\delta = 0$ as functions of vertical separation s, while Figure 4.4 shows the calculated torques at 21ω, 42ω, and 63ω as a function of s.

4.1.4 Precision Requirements

We wanted the overall *absolute* precision of the Newtonian torque calculations, $\delta\tilde{N}^G$, to be much better than the statistical uncertainty of the experimental values, which was as good as $\delta N \approx 3 \times 10^{-18}$ N·m (see Table 3.2). The total torque on the detector ring was the sum of four terms, one for each of the detector array-attractor ring combinations. The contributions of these four terms were roughly equal, so that $\delta\tilde{N}^G \approx 2\delta\tilde{N}^G_{\rm d}$, where $\delta\tilde{N}^G_{\rm d}$ is

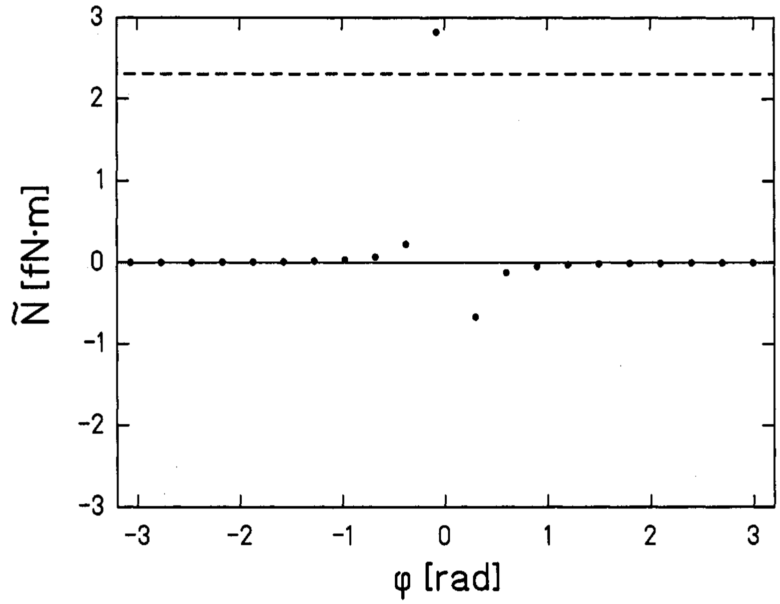

Figure 4.5: The torque on a single detector hole from the holes in a top attractor array at $s = 50\mu$m. Each point is the torque from one attractor hole on one detector hole. The angles were chosen such that one hole produced the maximum torque and are relative to the detector hole. The sum of these torques on the detector hole is shown as the dashed line; the nearest holes dominate this sum. The sum of these torques should be $\approx \frac{1}{42}$ of the closest point for top-ring torque plotted in Figure 4.3. It is not exact due to different arrays having different radii and thus contributing differently to the total torque.

the precision of the calculated torques on a single detector array from one attractor ring. We therefore required

$$\begin{aligned} \delta\tilde{N}^G &<< 3.0 \times 10^{-18}\ \mathrm{N}\cdot\mathrm{m} \\ \delta\tilde{N}^G_{\mathrm{d}} &<< 1.5 \times 10^{-18}\ \mathrm{N}\cdot\mathrm{m}\ . \end{aligned} \tag{4.6}$$

The torque on one detector array from one attractor ring, $\tilde{N}_{\mathrm{d}} = 21\, r\, F^{\mathrm{d}}_{\perp}$, where $r \approx .03$ m and $F^{\mathrm{d}}_{\perp}$ is the sum of torque-producing forces on a single detector hole from the 21 attractor holes in an array. $F_{\perp} = (t_{\perp}/t)F_t$ is the component of F_t that produces a torque and $0 \leq (t_{\perp}/t) \leq 1$ so that $\delta F_{\perp} \leq \delta F_t$. Figure 4.5 shows that the torque on a given pendulum hole is dominated by the torques from the few nearest attractor holes. But, for simplicity,

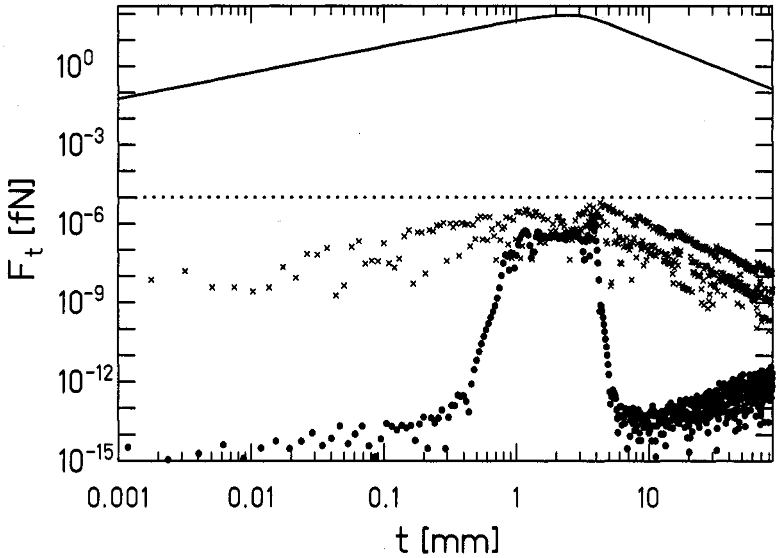

Figure 4.6: A typical Newtonian force calculation. The solid line shows F_t between a detector hole and top-attractor hole at a separation of $s = 50$ μm (the errors decreased with increasing s). The dots shows the integration error, determined by doubling the number of integration steps in evaluating each of the two dimensions of the force integral. The crosses show the error associated with the spline interpolation which we found by comparing the interpolated values halfway between the database points to a direct numerical evaluation of the force integrals. The dotted line shows the precision requirement of Equation 4.8

we can conservatively state $\delta F_{\perp}^{\mathrm{d}} \approx \sqrt{21}\,\delta F_{\perp}$. We satisfy Equation 4.6 if

$$\delta F_{\perp}^{G} \approx \frac{\delta \tilde{N}_{\mathrm{d}}^{G}}{21\sqrt{21}\,r} << 5 \times 10^{-19}\ \mathrm{N} \tag{4.7}$$

and by adopting the requirement

$$\delta F_{\mathrm{t}}^{G} \leq 1 \times 10^{-20}\ \mathrm{N} \tag{4.8}$$

we ensured that we far exceeded our required precision.

In checking the precision of our torque calculation, we had to consider three sources of error.. The first source was the precision of any given point in the force database; this precision was determined by the number of iterations in the numerical integration. The

Table 4.1: Newtonian Torque Calculation Error Budget

Source	$\delta\tilde{\mathrm{N}}$ contribution [N·m]
Force Calculation	$\leq 1.2 \times 10^{-19}$
Force Interpolation in t	$\leq 1.2 \times 10^{-19}$
Torque Interpolation in s	$\leq 5.0 \times 10^{-21}$
Torque Interpolation in δ	$\leq 5.0 \times 10^{-20}$
Total	$\sim 1.8 \times 10^{-19}$

second source was any error accrued from the interpolation of the force database; this error was dependent upon the density of points in t in the force database. The final source was an error accrued from the interpolations of the torque database; this error depended on the density of points in s and δ. Figure 4.6 shows the calculated Newtonian force and the errors associated with the database and its interpolation. The contributions to the error of the Newtonian torque calculations are listed in Table 4.1.

Our calculations of the non-Newtonian forces, $F_{\mathrm{t}}^{\mathrm{X}}$ could be less precise because the size of any resolved signal was of the same order as the size of our Newtonian residuals. Because the fractional uncertainties in the best-fit values of the strengths of non-Newtonian interactions were greater than 0.2, the systematic uncertainties from the corresponding calculations of the forces between the two closest holes (see Fig. 4.5) could be neglected as long as

$$\frac{\delta F_{\mathrm{t}}^{\mathrm{X}}}{F_{\mathrm{t}}^{\mathrm{X}}} << 0.2 \ . \tag{4.9}$$

We computed the non-Newtonian forces with an absolute accuracy good enough to satisfy Equation 4.9 in all cases. For example, the fractional accuracy of the Yukawa force calculation was better than $\sim 1.2 \times 10^{-2}$ at $\lambda = 50$ μm, $\sim 1.9 \times 10^{-3}$ at $\lambda = 100$ μm, and $\sim 4.5 \times 10^{-6}$ at $\lambda = 1$ mm at all values of s.

4.2 Forces Between Cylinders

The generation of the interpolated torque functions, torque databases, and interpolated force functions were routine efforts of geometry, database management and standard inter-

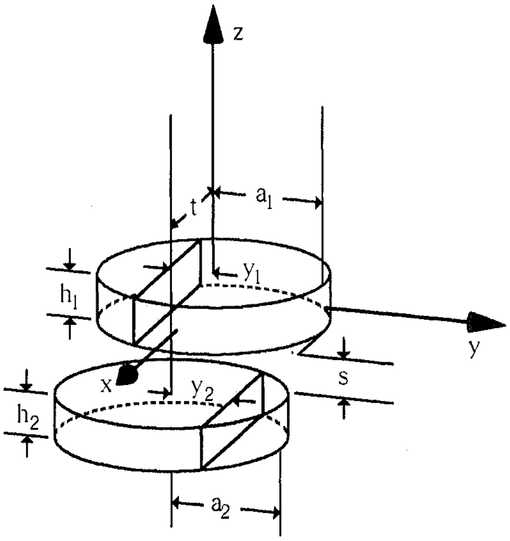

Figure 4.7: Coordinate system used in the force calculations.

polation. These tasks were generic and could be applied to any database of horizontal force vs. t and s. This section describes the calculation of the force between two holes for the Newtonian and new-physics potentials.

4.2.1 Approach

We assumed the test bodies were perfect cylinders with symmetry axes along $\vec{z}$, radii and thicknesses a_1, h_1 and a_2, h_2, and uniform negative densities ρ_1 and ρ_2. Without loss of generality, we can take one cylinder to be centered at the origin and the other at coordinates $(t, 0, s + [h_1 + h_2]/2)$ as shown in Fig. 4.7. For any potential, $\mathcal{V}$, the horizontal component of the force between two cylinders was computed as

$$F_t(t,s) = -G\rho_1\rho_2 \oint_{V_1}\oint_{V_2} dV_1 dV_2 \frac{\partial}{\partial t}\mathcal{V} \tag{4.10}$$

where the integrals extend over the volumes V_1 and V_2 of the two cylinders.

In all cases, the x and z integrals were evaluated first to give the force per unit thickness between two infinitely thin rectangular sheets lying parallel to the $x - z$ plane, as illustrated in Fig. 4.7. Because the force depends only upon the coordinate differences ($x_1 - x_2$, etc.), we transformed coordinates to $x = x_1 - x_2$, $X = x_1 + x_2$, $z = z_1 - z_2$, and $Z = z_1 + z_2$. Then the x integrations gave

$$I_x = \int \frac{\partial \mathcal{V}}{\partial x} dx_1 dx_2 = \int_{t_3}^{t_2} \mathcal{V} dx - \int_{t_0}^{t_1} \mathcal{V} dx \tag{4.11}$$

where $\mathcal{V}$ is one of the potentials described in Sections 4.2.2, 4.2.3, 4.2.4, 4.2.5, and 4.2.6, where

$$\begin{aligned} t_0 &= t - (a_2^2 - y_2^2)^{1/2} - (a_1^2 - y_1^2)^{1/2} \\ t_1 &= t - (a_2^2 - y_2^2)^{1/2} + (a_1^2 - y_1^2)^{1/2} \\ t_2 &= t + (a_2^2 - y_2^2)^{1/2} + (a_1^2 - y_1^2)^{1/2} \\ t_3 &= t + (a_2^2 - y_2^2)^{1/2} - (a_1^2 - y_1^2)^{1/2} \end{aligned} \tag{4.12}$$

Similarly, the z integrations gave

$$\begin{aligned} I_{xz} &= \int dz_1 dz_2 I_x \\ &= \int_{s_0}^{s_1} (z - s_0) I_x dz + \int_{s_1}^{s_3} (s_1 - s_0) I_x dz + \int_{s_3}^{s_2} (s_2 - z) I_x dz \end{aligned} \tag{4.13}$$

where $s_0 = s$, $s_1 = s + h_1$, $s_2 = s + h_1 + h_2$, and $s_3 = s + h_2$. The methods of evaluation of Equations 4.11 and 4.13 were potential dependent.

Finally, we made the substitution $y_i \rightarrow a_i \sin\theta_i$, so that an even spacing in θ would focus our calculation on the sections of the cylinders where the force contribution was greatest. Reflection symmetry about the $x - z$ plane allowed us to integrate one half of one cylinder and double the result, giving the integrals

$$\frac{F_t(t,s)}{G\rho_1\rho_2} = 2a_1a_2 \int_{-\pi/2}^{\pi/2} \int_0^{\pi/2} I_{xz} \cos\theta_1 \cos\theta_2 \, d\theta_1 \, d\theta_2. \tag{4.14}$$

These y integrals were evaluated numerically using a two-dimensional Romberg integration scheme derived from Reference [39]. Because the two y integrals represented the same physical dimension, we wanted them to be treated equally by the integration routine; a repeated one-dimensional integration would have made this difficult. A standard Romberg scheme is to apply Richardson's deferred approach to repeated refinements of the trapezoidal rule [39],

$$\int_{x_0}^{x_1} f(x)dx \approx \Delta x \left[\frac{1}{2}f(x_0) + \frac{1}{2}f(x_1)\right] \tag{4.15}$$

which approximates the function $f(x)$ as a line over a given interval $[x_0, x_1]$. In our case, we approximated the function $f(x, y)$ over a given two-dimensional interval $[x_0, x_1] \cap [y_0, y_1]$ as a plane. This approximation gives

$$\int_{x_0}^{x_1} \int_{y_0}^{y_1} f(x,y)dxdy \approx \Delta x \Delta y \left[\frac{1}{2} f(x_0, y_0) + \frac{1}{2} f(x_1, y_1) \right]. \tag{4.16}$$

We then applied Richardson's deferred approach to repeated refinements of this two-dimensional trapezoidal rule. This allowed us to set one precision goal for the y integrations and avoid considering the precision required for the force between each infinitesimally thin slice of one cylinder and the entire second cylinder.

4.2.2 Newtonian Force Calculation

The Newtonian potential is

$$\mathcal{V}(R) = -\frac{G m_1 m_2}{R} \tag{4.17}$$

where $R = |R_2 - R_1|$ is the distance between infinitesimal volumes in the two cylinders. All four Newtonian x and z integrals were evaluated analytically, yielding

$$\begin{aligned} I_{xz}^{G}\ (\ t, y, s) = & -\frac{1}{2} \sum_{i=0}^{3} \sum_{j=0}^{3} (-1)^{i+j} \\ & \times \left[t_i\, r_{ij} + \frac{t_i}{|t_i|}(y^2 - s_j^2) \ln \left(\frac{|t_i| + r_{ij}}{\sqrt{y^2 + s_j^2}} \right) \right. \\ & \left. - 2 t_i s_j \ln \left(1 + \frac{r_{ij}}{s_j} \right) + 2 y s_j \tan^{-1} \left(\frac{t_i s_j}{r_{ij} y} \right) \right] \end{aligned} \tag{4.18}$$

where $y = y_1 - y_2$ and $r_{ij}^2 = t_i^2 + y^2 + s_j^2$.

4.2.3 Yukawa Force Calculation

The Yukawa potential is

$$\mathcal{V}(R, \lambda) = -\alpha \frac{G m_1 m_2 \exp(-R/\lambda)}{R} \tag{4.19}$$

where $R = |R_2 - R_1|$ is the distance between infinitesimal volumes in the two cylinders, and λ is the length scale of the given Yukawa interaction, and α gives the strength of the interaction relative to newtonian gravity. We performed a separate calculation for each λ. We integrated Equation 4.13 for the Yukawa interaction by parts and made the substitution $p = 1/z$. This left the following x and z integrals, along with the y integrals, to be evaluated numerically

$$I^{Y}_{xz}\ (\ t, y, s, \lambda) = \lambda \left[\int_{t_3}^{t_2} dx - \int_{t_0}^{t_1} dx \right] \times \left[s_0 \int_{1/s_1}^{1/s_0} H dp + (s_1 - s_0) \int_{1/s_1}^{1/s_3} H dp + s_2 \int_{1/s_3}^{1/s_2} H dp \right], \tag{4.20}$$

where

$$H = \exp \frac{-\sqrt{x^2 + y^2 + 1/p^2}}{\lambda}\ . \tag{4.21}$$

4.2.4 Power-law Force Calculation

The power law potentials are

$$\mathcal{V}(R, k) = -\beta_k G m_1 m_2 \left(\frac{r_0}{R} \right)^k \tag{4.22}$$

where $r_0 \equiv 1$ mm and β_k gives the strength relative to Newtonian gravity. We performed four separate calculations for $k = 2 - 5$. These calculations required three numerical integrations. In this case, I_{xz} took the form

$$I^{P}_{xz}\ (\ t, y, s, k) = r_0^{k-1} \sum_{i=0}^{3} (-1)^i \left[\sum_{j=0}^{3} (-1)^j F_{ij}^{(k)} + s_0 \int_{s_1}^{s_0} G_i^{(k)} dz + (s_1 - s_0) \int_{s_1}^{s_3} G_i^{(k)} dz + s_2 \int_{s_3}^{s_2} G_i^{(k)} dz \right]. \tag{4.23}$$

Letting $y = y_1 - y_2$, $r_{ij}^2 = t_i^2 + y^2 + s_j^2$, $\rho_j^2 = y^2 + s_j^2$, and $\rho^2 = y^2 + z^2$, we have

$$\begin{aligned}
F_{ij}^{(2)} &= -\frac{t_i}{2}\ln\left(\frac{r_{ij}}{r_0}\right) + \rho_j \tan^{-1}\left(\frac{t_i}{\rho_j}\right) \qquad (4.24)\\
G_i^{(2)} &= \frac{1}{\rho}\tan^{-1}\left(\frac{t_i}{\rho}\right)\\
F_{ij}^{(3)} &= \ln\left(\frac{t_i + r_{ij}}{r_0}\right)\\
G_i^{(3)} &= \frac{t_i}{\rho^2\sqrt{(t_i^2+\rho^2)}}\\
F_{ij}^{(4)} &= \frac{1}{2\rho_j}\tan^{-1}\left(\frac{t_i}{\rho_j}\right)\\
G_i^{(4)} &= \frac{t_i}{2\rho^2(t_i^2+\rho^2)} + \frac{1}{2\rho^3}\tan^{-1}\left(\frac{t_i}{\rho}\right)\\
F_{ij}^{(5)} &= \frac{t_i}{3\rho_j^2 r_{ij}}\\
G_i^{(5)} &= \frac{t_i}{\rho^4\sqrt{t_i^2+\rho^2}}\left(1 - \frac{t_i^2}{3(t_i^2+\rho^2)}\right) .
\end{aligned}$$

4.2.5 Massive Pseudoscalar Exchange Force Calculation

The massive pseudoscalar potentials are

$$\mathcal{V}(R,\lambda) = -\gamma G m_1 m_2 \left(\frac{{r_0}^2}{R}\right)\left(\frac{K_1(2R/\lambda)}{\lambda}\right). \qquad (4.25)$$

where $r_0 \equiv 1$ mm, $K_1(x)$ is a modified Bessel function, and γ gives the strength relative to Newtonian gravity. In this case, only the integrations leading to Equations 4.11 and 4.13 could be done analytically. The 4 integrations needed to evaluate Equations 4.11, 4.13 and 4.14 were done numerically.

4.2.6 Force Calculation for the Fat-Graviton Scenario

The potential for the fat-graviton scenario of Section 1.1.2 is

$$V_{FG}(r) = G m_1 m_2 \int dr \frac{e^{-(r/\lambda_g)^3}}{r^2} = -G m_1 m_2 \left(\frac{e^{-\frac{r^3}{{\lambda_g}^3}}}{r} + \frac{P(\frac{2}{3},\frac{r^3}{{\lambda_g}^3})}{\lambda_g}\right) \qquad (4.26)$$

where $P(a,x)$ is the incomplete gamma function. Note that, as opposed to a Yukawa coupling, the strength of this additional potential is not arbitrary, but constrained to have the value in Equation 4.26 to achieve the behavior shown in Figure 1.2. As with the massive pseudoscalar exchange calculation, all four integrations after Equations 4.11 and 4.13 were done numerically.

Chapter 5

SYSTEMATIC ERRORS AND EXPERIMENTAL UNCERTAINTIES

Two types of systematic effects must be considered in this experiment: non-gravitational couplings that might produce a false signal, and the sensitivity of our calculated Newtonian signal to uncertainties in key experimental parameters. We directly measured mechanical, magnetic and thermal systematics to exclude their relevance to our experiment, while we modeled the sensitivity of our experiment to variations in these key experimental parameters. If our Newtonian signal was at all sensitive to a particular physical characteristic, we included that characteristic as a parameter in our fit.

5.1 Thermal Noise

The Fluctuation-Dissipation Theorem [40] states that any system that suffers dissipation will exhibit noise associated with that dissipation. Our torsion oscillator was dissipative, as one would expect for any real-world oscillator, and we easily observed this by noting a decay in its amplitude with time (Figure 5.1). To understand the source of this dissipation, we considered two possible sources: viscous drag and internal damping. Viscous drag adds a velocity-dependent friction term to the equation of motion and could be the result of friction between the pendulum and the surrounding gas. The equation of motion, with no driving torque, is then

$$I\ddot{\theta} + 2\alpha\dot{\theta} + \kappa\theta = 0 \tag{5.1}$$

characterizing the drag. Internal damping from losses within the fiber itself gives an imaginary component to the spring constant. The analog to Equation 5.1 for internal damping is

$$I\ddot{\theta} + \kappa(1 + i\phi)\theta = 0 \tag{5.2}$$

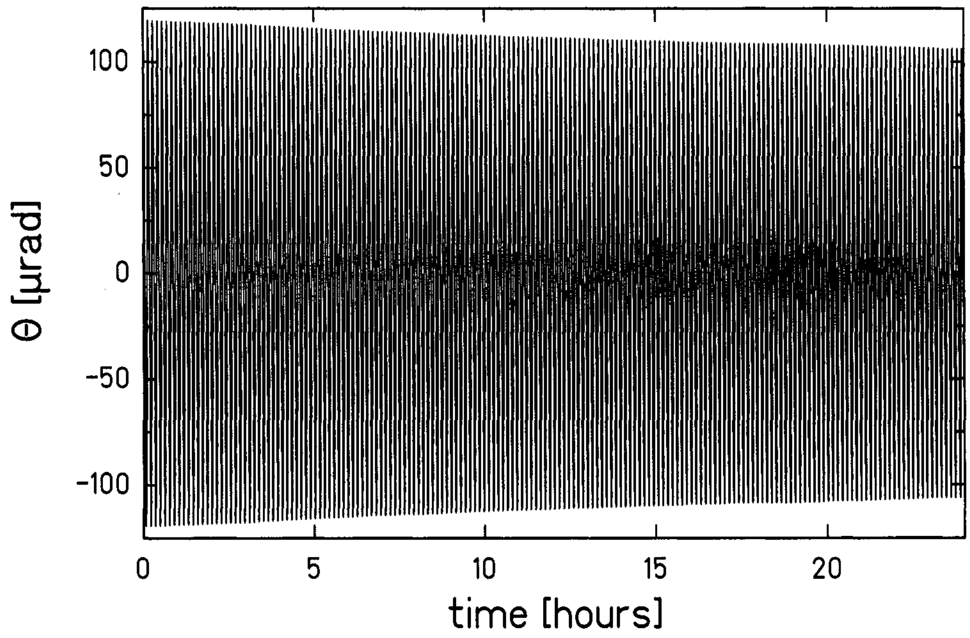

Figure 5.1: The decay of the amplitude over one day. A much larger amplitude was used here to mask smaller disturbing effects, for instance small kicks from a pressure spike. Linear and quadratic drift as a function of time has been subtracted from this data. The Q during our data set was ≈ 3000.

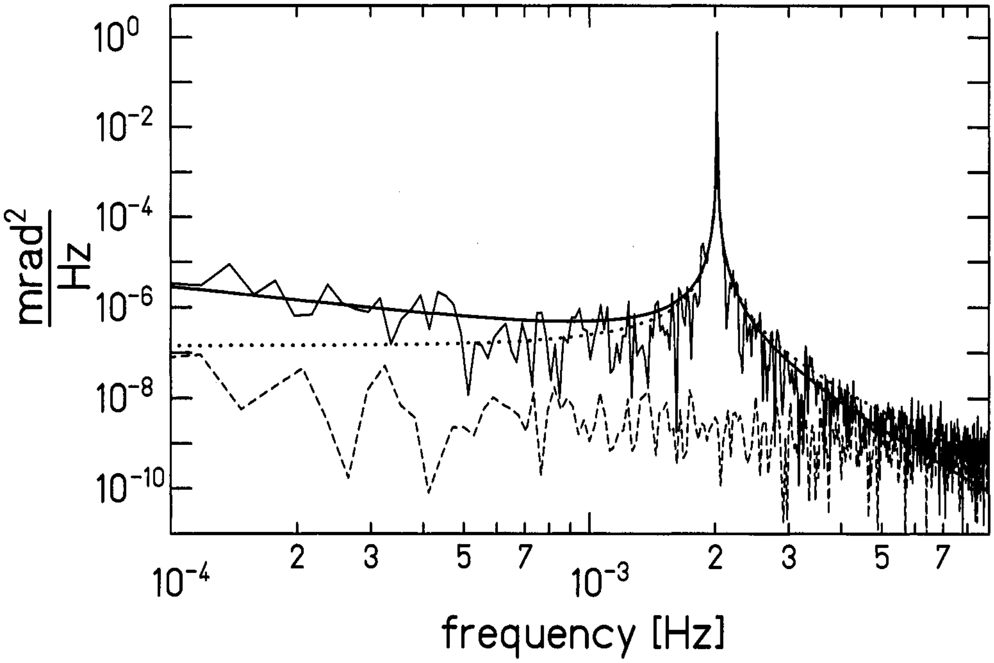

Figure 5.2: Power spectral density for a damped harmonic oscillator (DHO). The jagged solid line is data from our torsion pendulum. The dotted and dashed smooth lines are theoretical predictions for a DHO with velocity-dependent and internal damping respectively with $Q = 3000$. The low-frequency "$\frac{1}{f}$" noise of the internal damping scenario agrees well with our data. At higher frequencies, our signal becomes contaminated with readout noise, shown as the dashed jagged line.

The solution to both of these equations now has the form $\theta(t) = Ae^{-i\Omega t}e^{-t/\tau}$, where τ is the decay time of the oscillator. These two dissipation mechanisms produce noise with different frequency-dependences [41]. At frequencies low relative to the resonance, viscous damping noise power shows no dependence on frequency, while internal damping noise power is characterized by a "$\frac{1}{f}$" slope. Figure 5.2 shows the power spectral density (PSD) in θ from our pendulum, which indicates that our noise originates within the fiber itself. The PSD of an oscillator governed by Equation 5.2 is [41]

$$\theta^2(\omega) = \frac{4k_bT\kappa}{Q\omega[(\kappa - I\omega^2)^2 + \frac{\kappa^2}{Q^2}]} \tag{5.3}$$

where k_b is Boltzmann's constant and $Q = \pi\tau/\tau_0$, where τ_0 is the natural period of oscillation, is the standard quality factor of an oscillator, which in our case is

$$Q = \frac{1}{\phi}. \tag{5.4}$$

5.1.1 Observed Amplitude Noise

Figures 5.3 and 5.4 show that at small vertical separations between our detector ring and the conducting membrane, our noise departs from the expectation of pure thermal noise. One possibility is that this increased noise was due to an electrostatic interaction between the detector ring and the membrane. Some correlation between the pendulum's motions (in all modes) and an electrostatic potential might have contributed to this noise.

For each data run and each signal frequency, ω_m, we calculated an equivalent noise power, P_m, given the observed scatter of the twist signal, $\delta\theta_m$, such that

$$P_m = \delta\theta_m^2 \Delta t \tag{5.5}$$

where Δt is the length, in seconds, of the portion of the data run used to calculate $\delta\theta_m$. The $\delta\theta_m$ used were the actual angular noise, without any filters or other corrections applied, to correspond to the units of Figure 5.2. This calculation normalized all the runs, which had different lengths, and it accounted for parts of runs being discarded for outside disturbances. We fit all of these equivalent powers to curves

$$f_m(z) = a_m + b_m \mathrm{e}^{-z/\beta} \tag{5.6}$$

where z is the vertical separation between the ring and the screen, a_m is the average of P_m for $z > 0.5$ mm and β is common to all four frequencies. This fit was mainly heuristic, but the best fit value for β was 8±2 μm. Figure 5.4 shows the results of these fits. We observed an increased noise at all signal frequencies, though the noise at frequencies higher than the natural resonance diminished more rapidly with increasing z.

5.2 False Effects

We considered three possible couplings to the pendulum: thermal, magnetic and mechanical.

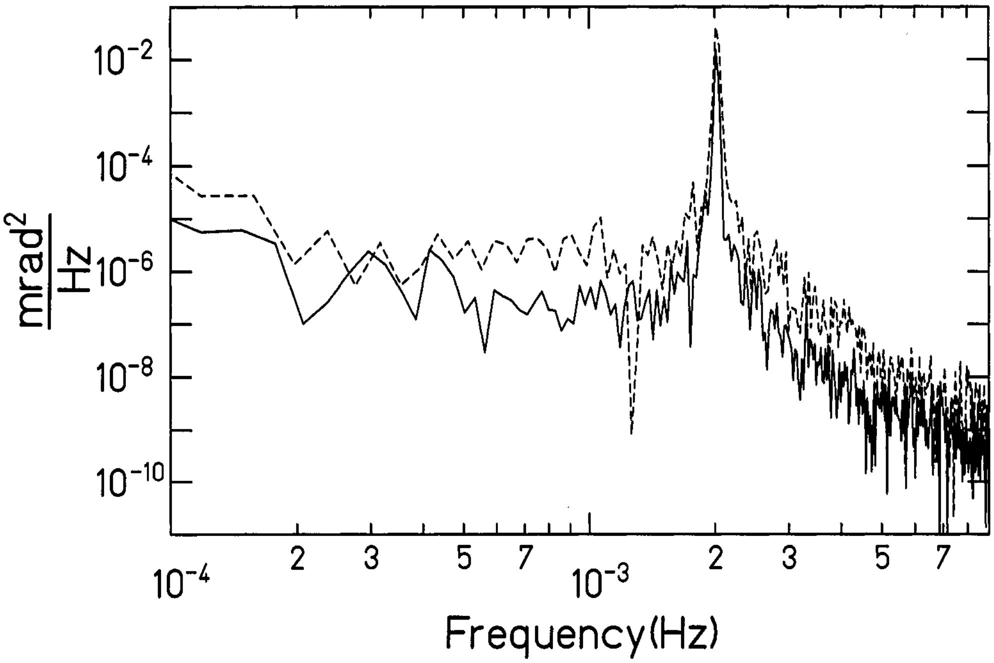

Figure 5.3: PSD of the natural resonance of our oscillator at 2.5 mm (solid line) and 50 μm (dashed line) above the conducting membrane, which shows an increased noise over all frequencies at small vertical separations.

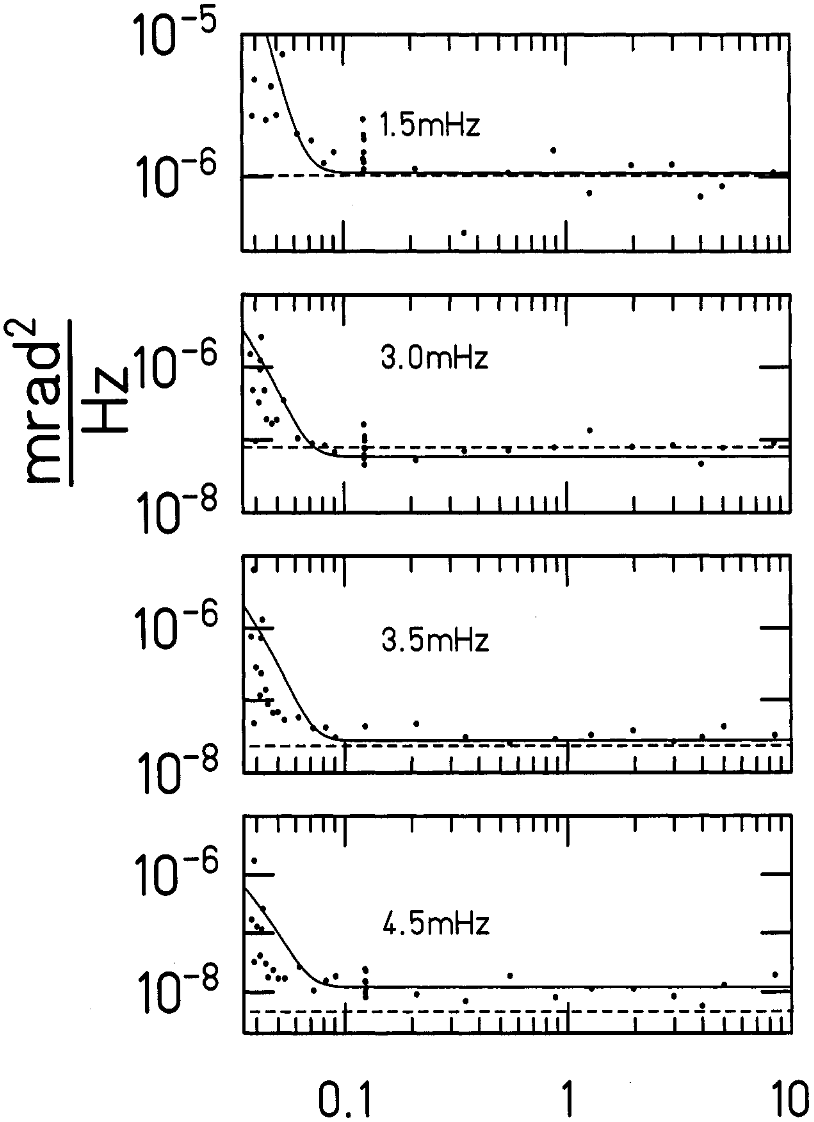

Figure 5.4: The observed angular noise in our data vs. z for the four different signal frequencies : (from top) $f_{21} \approx 1.5$ mHz, $f_{42} \approx 3.0$ mHz, $f_{cal} \approx 3.5$ mHz, and $f_{63} \approx 4.5$ mHz. The natural resonance of our pendulum is $f_{tor} \approx 2$ mHz. Noise at all four frequencies increased at small z. The solid lines are the results of the fits described in Section 5.1.1, while the dashed lines are the expectations from an internally damped oscillator with $Q = 3000$ as shown in Figure 5.2. There are several points omitted at 3.5 mHz because part of the data set had a different calibration frequency.

5.2.1 Thermal False Effects

A possible false effect might have come from a temperature variation at one of our signal frequencies. The temperature of our stepper motor varies with rotation angle, while our torsion fiber's equilibrium angle is sensitive to temperature changes. We averaged the temperature variation of a sensor mounted to the same copper plate as the attractor motor over our entire data set. We observed 20±15 μK, 16±7 μK, and 10±6 μK amplitudes at our three short-range signal frequencies, f_{21}, f_{42}, and f_{63} respectively.

We tested the response of our fiber to temperature variations by deliberately modulating the set-point of our Neslab water chiller to apply an exaggerated temperature variation to the apparatus. We modulated the temperature at $f_{mod} = 10^{-5}$ Hz and at 3.3×10^{-4} Hz and observed twist-to-temperature feed-throughs of 12.9 nrad/mK and 8.4 nrad/mK, respectively. The thermal time constants of our apparatus prevented us from achieving significant temperature modulations at higher frequencies; our slowest signal frequency, $f_{21} = 1.5$ mHz. This temperature effect must attenuate with higher frequencies because we are comparing a response of the pendulum to a "drive" signal on a temperature sensor on the vacuum vessel: the fiber is thermally decoupled from the rest of the vacuum vessel because it is surrounded by a heavy copper tube that has a weak thermal connection to the vessel. Thus, the drive and response have a weak thermal connection, which has a characteristic time constant. We can see that, even using these low-frequency numbers, the largest false angular effect we could have had, given the observed temperature variation of the apparatus, was 0.25±0.2nrad.

5.2.2 Mechanical False Effects

We could isolate a mechanical effect by rotating the pendulum and measuring deflection from another of its mirrors. If the signal changed phase with the pendulum rotation, it was likely due to a magnetic or spurious gravitational coupling. If the signal did not change phase, the effect was probably not a real twist of the pendulum, but a movement of the optical path relative to the pendulum, although one could imagine a complicated scenario where a mechanical vibration that varied at the rotation frequency coupled indirectly to the pendulum through an electrostatic interaction with the vibrating membrane.

We reduced the 1ω mechanical signal from ≈ 200 nrad to 50 nrad by adding a stiffening ring to the spider that held the rotating attractor mechanism and elements of the optical angle-readout and by placing small rubber feet between the motor and the vacuum vessel. There were no resolved signals at our signal frequencies.

5.2.3 Magnetic False Effects

The stepper motors driving the two attractors in this experiment were bound to have some of their magnetic field escape as they rotated. To test if this could give us a false signal, we placed a flux-gate magnetometer in the position of our pendulum and rotated the attractor holder. We measured a signal of 2.0 ± 0.8 μGauss in the horizontal plane at f_{21}. We repeated this measurement with the outer magnetic shield in place and this signal dropped to 0.02 ± 0.01 μGauss. With this outer shield in place, magnetic signals at all signal frequencies in all directions were ≤ 0.03 μGauss. These measurements were taken before an additional magnetic shield was added to the apparatus (the upper part of the Faraday cage surrounding the pendulum.)

To understand what effect an 0.03 μGauss variation might have on the pendulum twist, we placed two large coils near the experiment and modulated their current at the same frequency as our normal 21ω short-range signal to produce a ≈ 0.5 Gauss field modulation. With the outer and inner magnetic shields in place, we measured 6 nrad of induced twist. Without the outer shield, we measured 89 nrad. The shielding factor of the inner shield was measured to be ≈ 15 (the same as the outer shield), giving $\approx$2 nrad of twist per mGauss of drive. The induced pendulum twist from an 0.03 μGauss drive is several orders of magnitude below our statistical noise.

5.3 Measured Uncertainties

Our torque calculation was a function of measured experimental quantities that characterized the physical dimensions and relative displacements of our active mass rings. We either fixed these quantities in our calculation or included them as parameters that were free to vary in the fit. This section describes these parameters and how we determined their role in the torque calculation.

5.3.1 Attractor Phase Uncertainty

We measured the in- and out-of-phase components of the angular oscillations of our pendulum. The phase of our data was some arbitrary angle, ϕ_0 , relative to our calculated torques. Our calculated attractor rotation angle was defined as

$$\phi_c = n_s \frac{360}{480000} \text{ [degrees]} \tag{5.7}$$

where 480000 is the number of motor steps per revolution and n_s is the number of steps sent to our stepper motor since an earlier time when we defined $\phi_c = 0$.

During a data run, we noted the value of ϕ_c when the once-per-revolution index mark occurred, and recorded the value, ϕ_{ref}, which was the difference between ϕ_c and the closest multiple of 360.

With a perfect rotation drive, we would expect the recorded values of ϕ_{ref} to all be zero. There were several reasons this was not the case. We only recorded during which subsample of data ϕ_{ref} crossed. The period of a full revolution was $\approx$ 13900 seconds, while a subsample was $\approx$ 0.2 seconds long. This sampling granularity gave us a resolution in ϕ of $\approx$ 0.005 degrees. We saw deviations greater than 0.005 degrees due to our friction clutch. Our first stretch of data runs, with only the top attractor in place, showed a distinct modulation of ϕ_{ref} at one half the motor rotation frequency. The ball bearings of the rotating assembly move at half the rotation frequency, so this effect was likely due to the leaf springs of the friction clutch responding to a varying friction in the ball bearings. For the later stretch of data, we replaced the leaf springs in the friction clutch with weaker ones. We fit the distributions of ϕ_{ref} to two Gaussians, separated by 2δ and with widths σ. For the top-attractor-only runs, we found $\delta = 0.02$ degrees and $\sigma = 0.005$ degrees, while for the two-attractor runs, we found $\delta = 0.02$ degrees and $\sigma = 0.017$ degrees. Figure 5.5 shows the results of these measurements and the fits.

We extracted from these distributions the uncertainty of the mean of the ϕ_{ref}s in a given run. We calculated the variance of the distributions shown, μ_2, and noting that any given

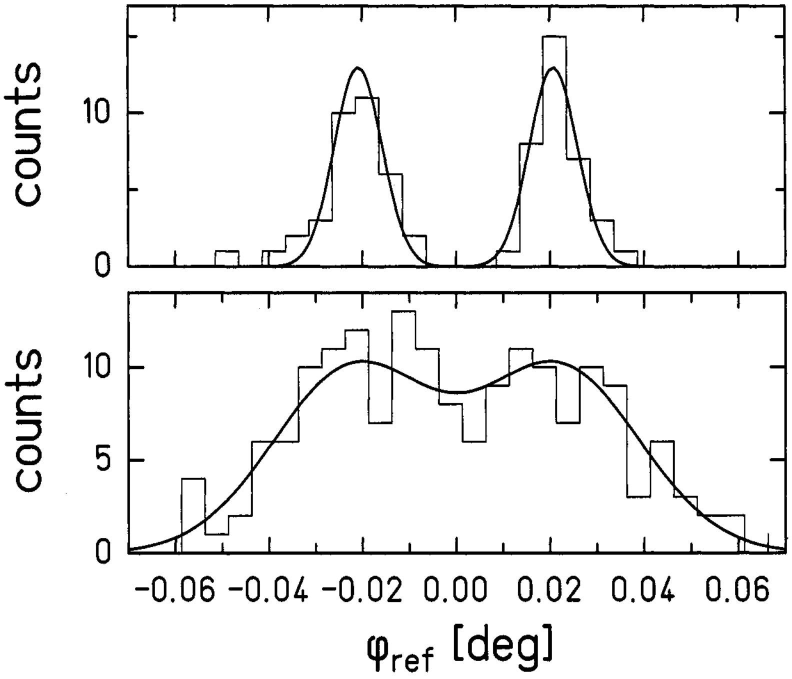

Figure 5.5: The scatter in the values of ϕ_{ref} for the top-only data runs (top frame) and the two-attractor data runs (bottom frame). Also shown are fits to two displaced Gaussians.

run had 4 or 5 ϕ_{ref} recordings, we calculated

$$\delta\phi_{ref} \approx \sqrt{\mu_2/4} \tag{5.8}$$

giving the values 0.006 and 0.012 degrees for the top-only and two-attractor data sets respectively. We included an uncertainty in the actual attractor phase as a fit parameter for each run in our data set, using these values of δ_ϕ as constraints.

5.3.2 Missing Masses, Hole Radii, and Ring Thicknesses

As described in more detail in Section 6.1, our torque calculation has the general form

$$\tilde{N}_m = \left(\frac{m_d}{\pi r_d^2 h_d}\right)\left[\left(\frac{m_u}{\pi r_u^2 h_u}\right)\tilde{N}_m^{\mathrm{u}} + \left(\frac{m_l}{\pi r_l^2 h_l}\right)\tilde{N}_m^{\mathrm{l}}\right] \tag{5.9}$$

where $\tilde{N}_m^{\mathrm{u}}$ and $\tilde{N}_m^{\mathrm{l}}$ are the calculated torques at harmonics, m, on the detector ring from the upper and lower attractors respectively. The multiplying factors are the densities of the (from left) detector, upper, and lower rings, which are determined by the missing masses, m, the hole radii, r, and the ring thicknesses h (see Section 2.2 for measurement details.) The relative densities of the attractor rings were important to determine the exact cancelation between the two attractors, while the detector ring density (along with our absolute calibration) set the torque scale of the experiment.

The simplest parameterization of these quantities would have been as densities, but we learned through a previous measurement that the different harmonics of our torque depended differently on the size of our holes. One can understand this by considering that the characteristic angular scale for a given harmonic, m, is $2\pi/m$. A small change in a hole radius, δr, results in a difference of subtended angle, $\delta r/R$, where R is the radius of the hole array. The fractional importance of this small change in angle is then $\frac{m\delta r}{2\pi R}$. A small variation in the angular scale over which our missing mass is distributed varied the harmonic content of our torque, while varying the missing masses scaled all harmonics identically. Thus, we included both the masses and the hole radii as fit parameters. The ring thicknesses, h, would have been degenerate with the masses as fit parameters, so they are fixed quantities in our calculation. The thickness of the upper attractor ring was an exception, in that it also determined the relative vertical position of the lower attractor. Another fit parameter, the gap, accounted for this relative position.

5.3.3 *Vertical positions: the gap and z_0*

The dependence of our torque on the relative vertical displacements of the three rings can be seen from

$$\tilde{N}_m(z - z_0) = \rho_d \left[\rho_u \tilde{N}^{\mathrm{u}}_m(z - z_0) + \rho_l \tilde{N}^{\mathrm{l}}_m(z - z_0 + g)\right] \tag{5.10}$$

where z is the vertical micrometer reading, z_0 is the vertical micrometer reading where the detector surface would just touch the top attractor, g is the vertical gap between the two attractor rings, and the densities from Equation 5.9 have been abbreviated as ρ. The cancelation of the two terms in the torque was sensitive to the relative positions of the two attractors (given by g), while the slope of the torque was greatest at small separations, a characteristic which correlated z_0 with any potential new-physics signal, which we anticipated to be of short-range. z_0 and g were both included as variable fit parameters.

5.3.4 *Detector Ring Curvature, ψ*

After our data set was complete, we took more detailed and comprehensive measurements of the linear dimensions of the rings with a coordinate measuring machine (see Section 2.2.) During this process, we noted that the detector ring, as mounted on the pendulum, was curved as shown schematically in Figure 5.6. If our capacitance measurement, which determined our vertical separations, and the torque measurements were sensitive in different ways to this curvature, our model of torque versus separation would not have accurately described our data. We did not account for this curvature in our finite-element calculation of the capacitance vs. height above the conducting membrane because we relied on the 21-fold symmetry of our geometry to simplify (and make possible) the calculation.

The capacitance between two plates where one plate is curved, is, to first-order,

$$C(d) = \epsilon_0 \int_0^{\nu_{max}} \frac{\mathcal{DA}(\nu)}{d + \nu} d\nu \tag{5.11}$$

where $\mathcal{DA}(\nu)$ is the area per unit height for a given height, ν, above the lowest point on the surface of the curved plate, and ν_{max} is the total amount of vertical deflection in the

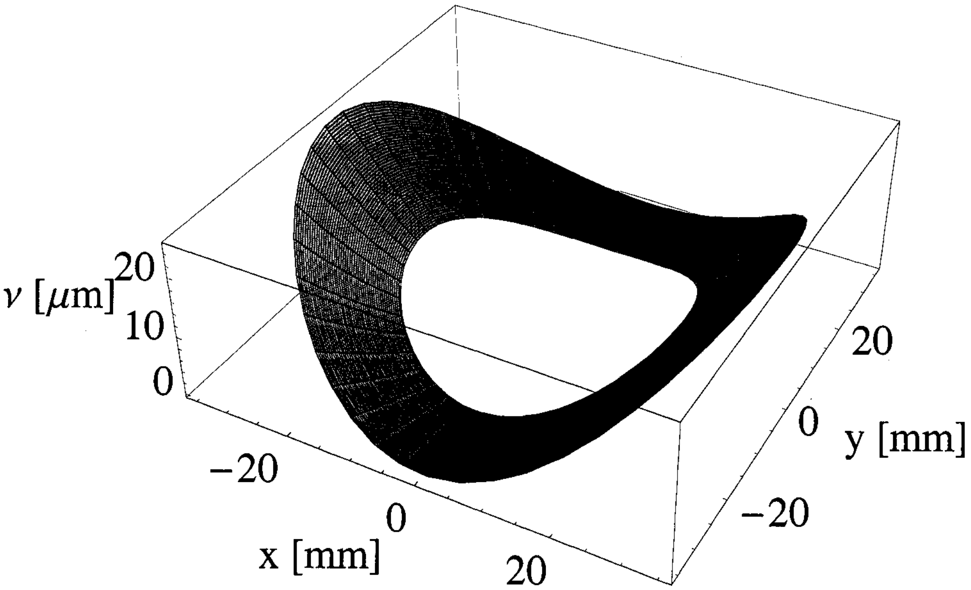

Figure 5.6: A schematic of the detector ring curvature as the ring was mounted on the pendulum. Note the units of the vertical scale are μm.

curvature (in our case 25 μm.) The case of a flat plate can be retrieved from Equation 5.11 by setting $\mathcal{DA}(\nu) = \mathrm{A}\delta(\nu)$, where A is the total area of the ring and $\delta(\nu)$ is a delta function. Figure 5.7 compares $C(d)$ for $\nu_{max} = 25$ μm to $\nu_{max} = 0$ μm.

We calculated the quantity

$$\delta z(d) = (\epsilon_0 A/C(d)) - d \tag{5.12}$$

to indicate the relative discrepancy between the curved and flat case in units of vertical separation. One can interpret $\delta z(d)$ as follows: given a measured capacitance C_m, we inferred some membrane-to-ring separation, $d = \epsilon_0 A/C_m$, which is actually the distance from the membrane to $\delta z(d)$ above the lowest point on the detector ring. Figure 5.8 shows the result of this calculation. The curvature of the detector ring shifted the capacitance curve up by ≈ 8 μm, such that, when we determined the vertical separation between the upper attractor and the detector rings, we were actually determining the distance to a point ≈ 8 μm above the lowest point on the detector ring.

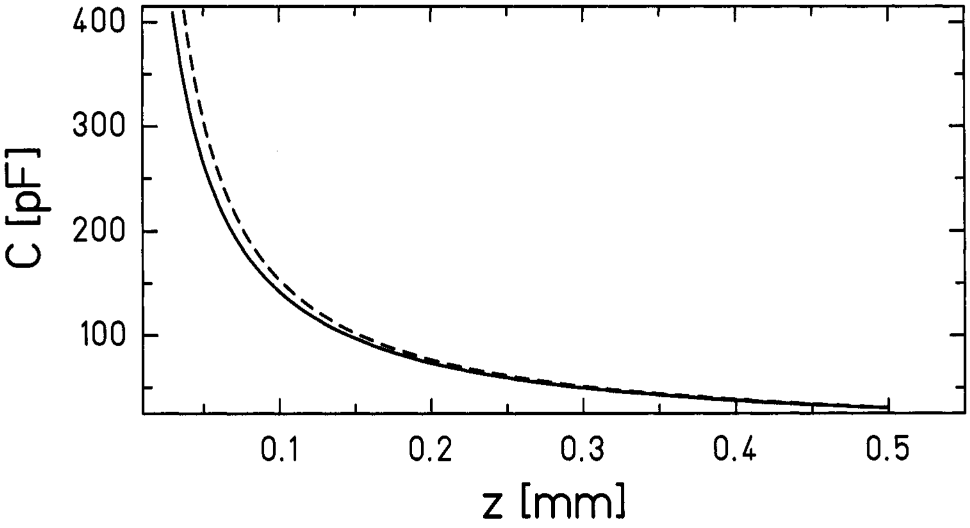

Figure 5.7: The effect of the detector ring curvature on capacitance. The solid line is calculated with Equation 5.11 with $\nu_{max} = 25\ \mu$m, while the dashed line is the ideal flat plate calculation.

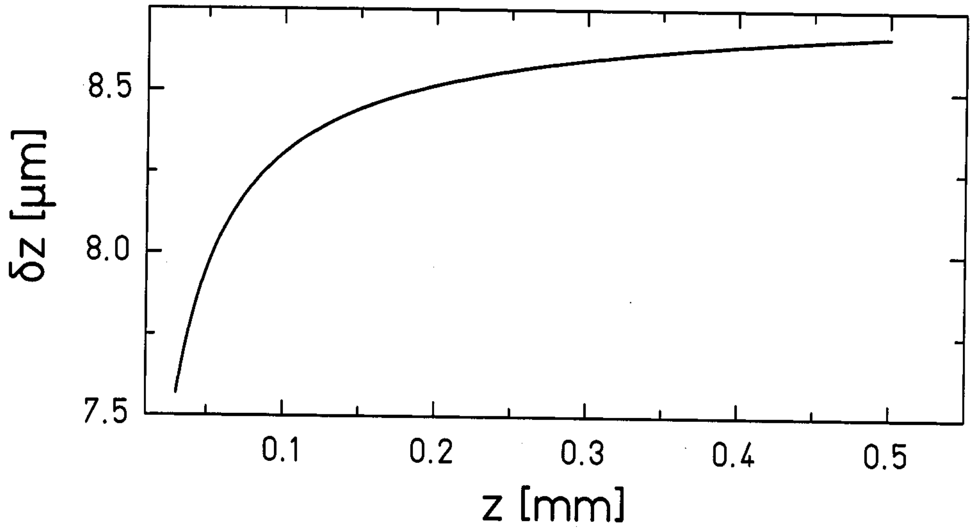

Figure 5.8: The apparent z-shift, δz due to the curvature of the detector ring. δz varies by $\approx 1\mu$m over the range where we measured capacitance to tell us the separation. This variation was small enough for us to consider δz a constant because the uncertainty in our micrometer read-out is of this order.

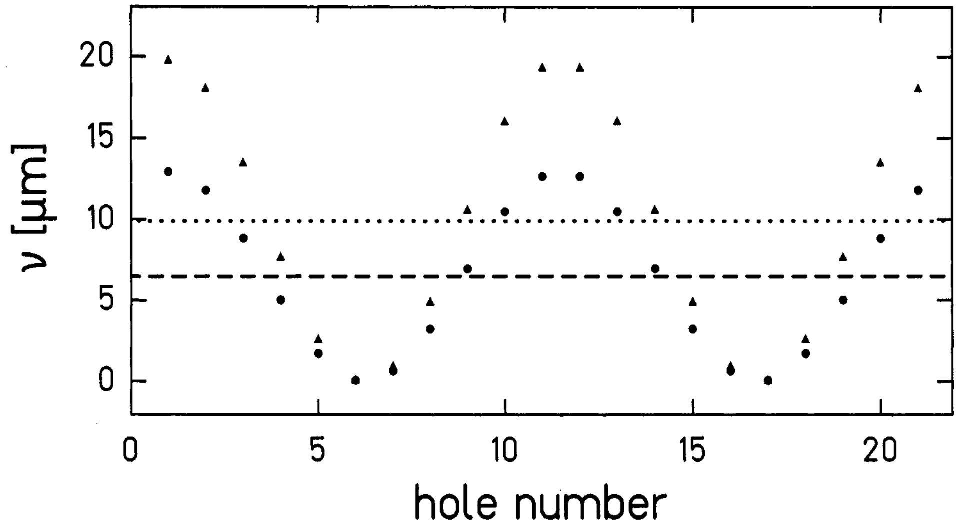

Figure 5.9: The vertical positions of the centers of holes in the detector ring above the lowest point on the ring. The outer and inner hole positions are shown as triangles, and circles, respectively. The average position of the inner holes (dashed line, $\nu = 6.5$ μm) and outer holes (dotted line, $\nu = 10.0$ μm) differ by 3.5 μm.

To understand how this curvature affected our measurement of torque vs. separation, s, we needed to understand the curvature's effect on our Newtonian torque. Figure 5.9 shows the vertical placement of the holes in the detector ring. There were two effects we needed to consider: how the torque on one array (inner or outer) of the detector ring changed given the spread in ν and how the total torque changed given the different average vertical separation of the two arrays.

We compared the torque calculation, $\tilde{N}_{21}(s)$, for the ideal case where all holes in one array were at the same s to the calculated torque accounting for the spread in the positions shown in Figure 5.9. Figure 5.10 shows the effect of the bend on the torque,

$$B_{21}(s) = \left| \tilde{N}_{21}(s) - \frac{1}{21} \sum_i \tilde{N}_{21}(s + \nu_i - \overline{\nu}) \right| \qquad (5.13)$$

as a function of s for both the outer and inner arrays of the detector ring, where ν_i is the vertical position of the ith hole above the lowest point on the ring, and $\overline{\nu}$ is the mean position of all the holes in that array above the lowest point. The effect is negligible compared to our observed torque noise, and we can use the average height of the holes as the calculated value for each hole array on the detector ring.

While the average height of a given array sufficed for our calculation, the fact that the two arrays on the detector ring had *different* average heights was a more significant effect. Figure 5.11 shows the effect on our calculation of the two arrays having vertical positions that differed by 3.5 μm. This effect was large compared to our statistical errors and we introduced a parameter, ψ, to account for this in our fitting function. The average height of *all* the holes in the detector ring was within 1 μm of the height inferred from the capacitance measurement, z, so we defined ψ such that the outer array was positioned at $z + \psi$ and the inner array was positioned a $z - \psi$, with the nominal value for ψ of 1.75 μm.

5.3.5 Hole array radii

As discussed in Section 2.2, we measured the radii of all the holes in each ring at one time on the coordinate measuring machine. For each hole, we fit the center position and the radius. We then fit all of these center positions to a best-fit circle. The residuals of the measured positions of the hole centers to this best-fit can be seen in Figures 2.3 and 2.4.

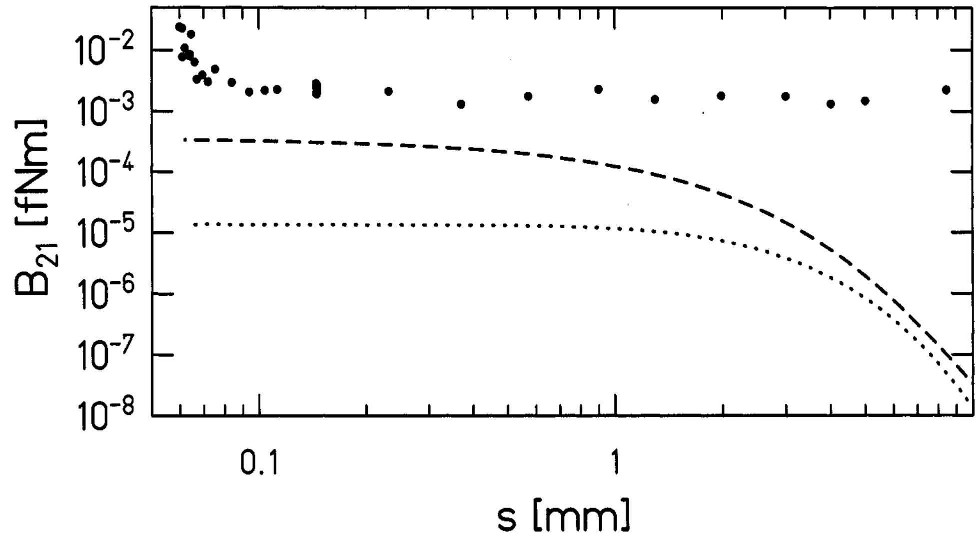

Figure 5.10: The difference between calculated torques for a flat plate and a curved detector ring (Equation 5.13.) The dotted and dashed lines are for the outer and inner hole arrays, respectively. For reference, the observed torque uncertainties are shown as the circles.

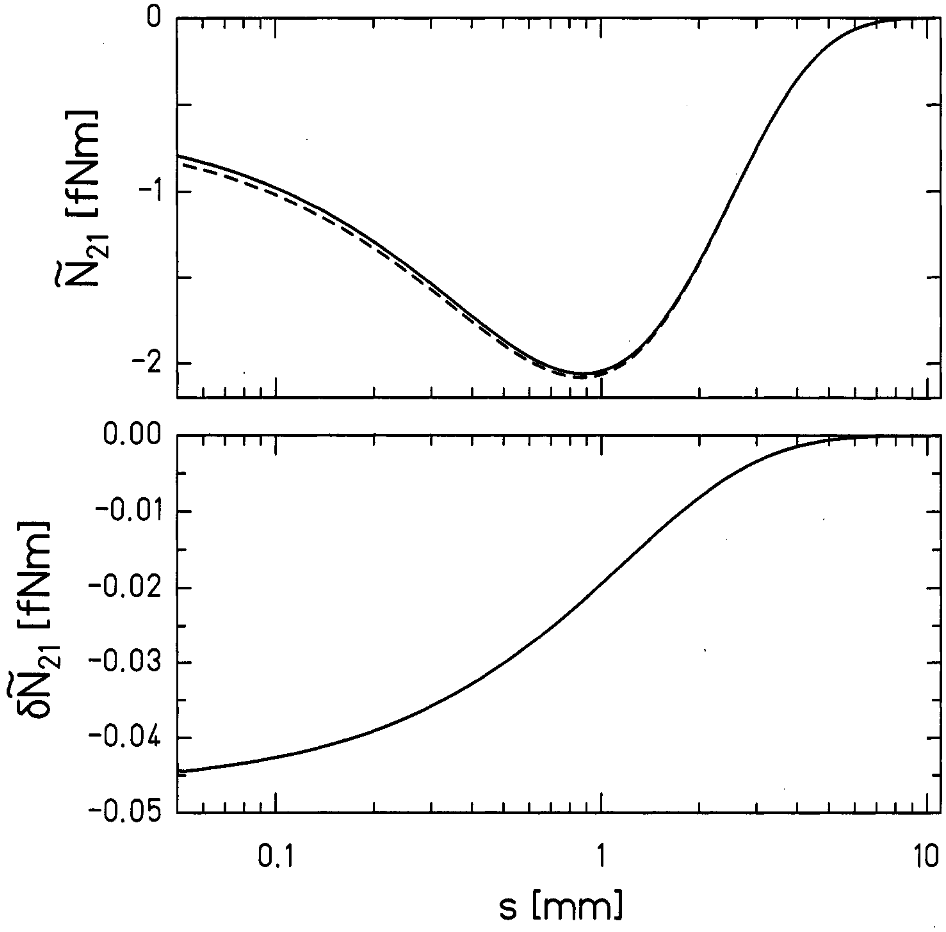

Figure 5.11: A comparison of calculated torque for a flat and bent detector ring. In the upper panel, the solid line shows the torque for the two arrays at the same vertical position, while the dashed line shows the torque for the outer and inner arrays shifted ±1.75 μm, respectively. The bottom panel shows the difference between these two calculations.

We checked that it was appropriate to use the best-fit value for the hole array radii, rather than account for the scatter around the best fit-value directly by calculating :

$$\delta\tilde{N}_{21}(R) = \left|\tilde{N}_{21}(R) - \frac{1}{2}\left(\tilde{N}_{21}(R+\Delta) - \tilde{N}_{21}(R-\Delta)\right)\right| \tag{5.14}$$

where we took $\Delta = 3\ \mu$m. This calculation was a worst-case representation of the actual distributions of the hole positions, by placing half the holes at the maximum deviation and the other half at the minimum. We used this worst-case approximation in the interest of calculation time. The greatest value of $\delta\tilde{N}_{21}$ at any height, varying any of the six hole array radii, was 6×10^{-4} fNm : we safely approximated the distribution of hole placements by the best-fit value of the hole array radii.

There was also an error associated with the best-fit radii: we measured the repeatability of the coordinate measuring machine to be $\delta = 0.75\ \mu$m. We calculated the quantity

$$\delta\tilde{N}_{21}(R) = \left|\tilde{N}_{21}(R+\delta) - \tilde{N}_{21}(R)\right| \tag{5.15}$$

to see what effect a variation in our average array radii would have. The top attractor hole radii were the least sensitive to this variation : $\delta\tilde{N}_{21}$ changed up to 2.3×10^{-3} fNm. The total torque was more sensitive to the relative placement of the detector and bottom ring array radii. Varying any one of the radii of the detector or bottom attractor rings changed the torque by up to 1.2×10^{-2} fNm at the closest separations, on the order of our statistical noise. We did not include any of these radii as fit parameters, because their effects were completely correlated with the gap. Changing the array radii of the bottom ring changes the average separation between the bottom ring holes and the detector holes. But, a slight vertical compensation more than balances this effect. For example, a $0.5\ \mu$m change in the lower array radius is nearly exactly compensated by an $0.13\ \mu$m change in the gap. Our measurement error on the gap was $\approx 2\ \mu$m, so the gap parameter can easily accommodate these uncertainties in the array radii.

5.3.6 Hole Array Concentricity

Section 2.5.3 noted that the hole arrays of the attractor rings were misaligned with the rotation axis of the bearing assembly by $\approx 10\ \mu$m. The attractor holes were then rotating about the bearing axis in some distribution of radii within ±10 μm of the measured radius of the array. This is the same effect as described by Equation 5.14, except with $\Delta = 10\ \mu$m. This effect was also small and degenerate with the gap.

Chapter 6

FITTING AND RESULTS

We tested the ISL by comparing our measured torques, $N_m(\vec{\zeta_j}) \pm \delta N_m(\vec{\zeta_j})$ at frequencies $m\omega$, to our model of the torque $\tilde{N}_m(\vec{\zeta_j}, \vec{\eta})$, where $\vec{\zeta_j} = (x_j, y_j, z_j)$ is the indicated pendulum position for the jth data run, and $\vec{\eta}$ is an array of instrumental parameters, described below in Section 6.1. We fit our complete data set by minimizing

$$\chi^2 = \sum_j \sum_m \left[\frac{N_m(\vec{\zeta_j}) - \tilde{N}_m(\vec{\zeta_j}, \vec{\eta})}{\Delta N_m(\vec{\zeta_j})} \right]^2 + \sum_n \left[\frac{\eta_n^{\mathrm{exp}} - \eta_n}{\delta \eta_n^{\mathrm{exp}}} \right]^2 , \tag{6.1}$$

where $\eta_n^{\mathrm{exp}} \pm \delta\eta_n^{\mathrm{exp}}$ were our independently measured values for our experimental parameters and where

$$\Delta N_m(\vec{\zeta_j}) = \sqrt{(\delta N_m(\vec{\zeta_j}))^2 + \left(\delta s_j \frac{\partial \tilde{N}_m}{\partial s_j} \right)^2} . \tag{6.2}$$

accounted for the uncertainty in our measurement of the detector ring's vertical position, δs_j, for each run by adding, in quadrature, the corresponding uncertainty in the fitting function, $\left(\delta s_j \frac{\partial \tilde{N}_m}{\partial s_j}\right)$, to the experimental statistical errors. The second term of Equation 6.1 was our method of accounting for uncertainties in our *a priori* knowledge of our key instrumental parameters. Our inclusion of these measurements in our determination of χ^2 assumes that these measurement errors are normally distributed.

We minimized Equation 6.1 using a non-linear least-squares Levenberg-Marquardt method as described in Reference [39].

6.1 Fitting Functions and Instrumental Parameters

The calculated torque functions of Equation 6.1, $\tilde{N}_m(\vec{\zeta_j}, \vec{\eta})$, were total calculated torque harmonics for a given position, $\vec{\zeta_j}$, and set of instrumental parameters, $\vec{\eta}$, and were combinations of the individual array torque functions, $\tilde{N}_m(\delta, s)$,of Equation 4.1. For our fitting functions, we considered four different $\tilde{N}_m(\delta, s)$:

- $\tilde{N}_m^1(\delta, s)$: the torque between the upper attractor arrays and the outer detector array.
- $\tilde{N}_m^2(\delta, s)$: the torque between the upper attractor arrays and the inner detector array.
- $\tilde{N}_m^3(\delta, s)$: the torque between the lower attractor arrays and the outer detector array.
- $\tilde{N}_m^4(\delta, s)$: the torque between the lower attractor arrays and the inner detector array.

By treating the torque calculations for the two detector arrays separately, we were able to account for the detector ring curvature, as described in Section 5.3.4. The inner and outer holes of the upper and lower attractor arrays were calculated at the same vertical position, because, once the upper attractor ring was glued to the thicker lower attractor ring, it had no observable curvature.

Our fitting function for the Newtonian potential was

$$\begin{aligned} \tilde{N}_m(\vec{\zeta}_j, \vec{\eta}) = G\frac{m_d}{\pi a_d^2 h_d} \times \qquad (6.3) \\ \left\{ \frac{m_u}{\pi (a_u)^2 h_u} T(\phi_0 + \pi_j) \left[\tilde{N}_m^1\left(a_d, a_u, \delta_j, s_j + \psi\right) \right. \right. \\ \left. + \tilde{N}_m^2\left(a_d, a_u, \delta_j, s_j - \psi\right) \right] \\ + \frac{m_l}{\pi (a_l)^2 h_l} T(\phi_0 + \pi_j + \vartheta) \left[\tilde{N}_m^3\left(a_d, a_l, \delta_j, s_j + \psi + h_u + g\right) \right. \\ \left. \left. + \tilde{N}_m^4\left(a_d, a_l, \delta_j, s_j - \psi + h_u + g\right) \right] \right\} \end{aligned}$$

where $\delta_j = \sqrt{(x_j - x_0)^2 + (y_j - y_0)^2}$ and $s_j = z_j - z_0$. $T(\theta)$ is a rotation operator that rotates the components of $\tilde{N}_m(\delta, s)$ by $m\theta$.

$\tilde{N}_m\left(a_1, a_2, \delta, s\right)$ of Equation 6.3 is related to $\tilde{N}_m\left(\delta, s\right)$ of Chapter 4 in the following way. We measured the holes radii $a_1 \pm \delta a_1$ ($a_2 \pm \delta a_2$) of the detector (attractor) holes. We calculated $\tilde{N}_m\left(\delta, s\right)$ for each of the four combinations $(a_1 \pm \sigma_1, a_2 \pm \sigma_2)$ where we have chosen $\sigma = 2.5\ \mu$m for all holes, while δa is typically $\leq 1\ \mu$m (Table 2.1.) $\tilde{N}_m\left(a_1, a_2, \delta, s\right)$ is a bilinear interpolation over the four calculated $\tilde{N}_m\left(\delta, s\right)$ to a particular value of (a_1, a_2). This interpolation allowed our fitting function to treat the hole radii as variable fit parameters.

When we fit to an additional new-physics potential, we added to this fitting function a second term, identical in form, but whose preceding factor was an additional adjustable parameter and whose $\tilde{N}_m(\delta, s)$ were computed for one of the new-physics potentials.

Our instrumental parameters were defined as

- $m_d,\ m_u,\ m_l$: The total missing mass of the holes for the detector, upper attractor, and lower attractor respectively. (Section 2.2). The fractional uncertainty in m_d was combined with the calculated fractional uncertainty in the calibration torque, N_c as these two uncertainties were degenerate.

- $a_d,\ a_u, a_l$: The average hole radii for the detector, upper attractor, and lower attractor respectively. (Section 2.2)

- g : The gap. The vertical separation between the upper surface of the lower attractor and the lower surface of the upper attractor. This was measured by comparing the sum of the two measured thicknesses of the attractor rings to the combined thickness after gluing them together.

- $x_0,\ y_0,\ z_0,\ x_0',\ y_0',\ z_0'$: The pendulum position (x_0, y_0, z_0) is defined to be the one when the pendulum would have been coaxial with the attractors and its lowest surface would have just touched the upper surface of the upper attractor. $(x_0',\ y_0',\ z_0')$ is the same quantity, but for the data runs where the lower attractor was not used.

- $\phi_0,\ \phi_0'$: An arbitrary rotation of our calculation. Physically, this is the angle between our once-per-revolution index mark on the attractor and the angular position where the pendulum and upper attractor holes are aligned. ϕ_0' is the same quantity, but for those runs where the lower attractor was not used.

- ψ : The detector ring was curved, placing the outer array, on average, at a slightly higher z value than the upper array. ψ is one half the difference between the average heights of the two arrays. See Section 5.3.4 for a detailed description of this curvature.

- ϑ : The angle between the upper attractor arrays and the lower attractor array; this angle was nominally $\frac{\pi}{21}$.

- $\vec{\pi}$,$\vec{\pi}'$: In each data run, the actual phase of the attractor could deviate slightly from the phase calculated by counting pulses sent to the attractor drive motor (Section 5.3.1.) $\vec{\pi}$ is a vector of phase deviations, one for each data run, that could be adjusted to fit the data, within the uncertainties discussed in Section 5.3.1. $\vec{\pi}'$ is the same quantity, but for the data runs with only the upper attractor.

6.2 Results of Newtonian Fit

By fitting our data to the Newtonian fitting function, we obtain $\chi^2 = 363.9$ with ν=342 degrees of freedom (DOF) and $Q(\chi^2,\nu)$=0.20 is the probability that a χ^2 as large as this could arise by chance. This data consisted of 54 runs where we measured the in- and out-of phase components of the first three torque harmonics (324 DOF). There were six runs where we chose the frequency of our calibration turntable poorly so that the highest harmonic was subject to a beating effect between different frequencies. In these six runs, we analyzed only the first two harmonics (+24 DOF). In addition there were 78 instrumental parameters (60 of which are $\vec{\pi}$ and $\vec{\pi}'$), 72 of these 78 parameters were independently measured (-6 DOF), leaving us with 342 DOF. Table 6.1 shows our measured and fitted parameters for the Newtonian fit. Figure 6.1 shows the fitted values for the phases $\vec{\pi}$ and $\vec{\pi}'$.

Figure 6.2 shows the results of the fit and the residuals for the data runs where only the upper attractor was in place. Figure 6.3 shows the results of the fit and the residuals for the centering data for the data runs where both attractors were in place, which were measured at $s \approx 150$ μm. Figure 6.4 shows the results of the fit and the residuals for the data runs where both attractors were in place. Figure 6.5 is another plot of the residuals from 6.4, zoomed in on the data points with small s. Only the in-phase components of these data runs are shown as we rotated the data to place the signal almost entirely in one component: any interesting new-physics signal should occur in-phase with the Newtonian signal (i.e. it couples to mass). The out-of-phase component *was* included in the fit of the data.

Table 6.1: The measured and fitted values for our instrumental parameters. The fitted values of a_d, and z_0 are more than 2σ from the measured values.

Parameter	Measured			Fitted			Units
m_d	0.1833	±	0.0004	0.1825	±	0.0003	g
m_u	0.081634	±	0.000003	0.081634	±	0.000003	g
m_l	1.6027	±	0.0003	1.6027	±	0.0003	g
a_d	2.3813	±	0.0008	2.3831	±	0.0002	mm
a_u	1.5865	±	0.0008	1.5880	±	0.0005	mm
a_l	3.1720	±	0.0009	3.1721	±	0.0008	mm
g	−0.0008	±	0.002	−0.0005	±	0.0008	mm
x_0	N/A			−0.4267	±	0.0015	mm
y_0	N/A			−0.3120	±	0.0017	mm
z_0	−0.022	±	0.002	−0.0295	±	0.0013	mm
ϕ_0	N/A			0.00077	±	0.00005	rad
x'_0	N/A			−0.505	±	0.010	mm
y'_0	N/A			1.429	±	0.005	mm
z'_0	−0.202	±	0.003	−0.199	±	0.002	mm
ϕ'_0	N/A			0.00004	±	0.00003	rad
ψ	1.8	±	0.1	1.8	±	0.1	μm
ϑ	0.1496	±	0.0005	0.149567	±	0.000001	rad
$\vec{\pi}$	0.0	±	0.0002	See Figure 6.1			rad
$\vec{\pi}'$	0.0	±	0.0001	See Figure 6.1			rad

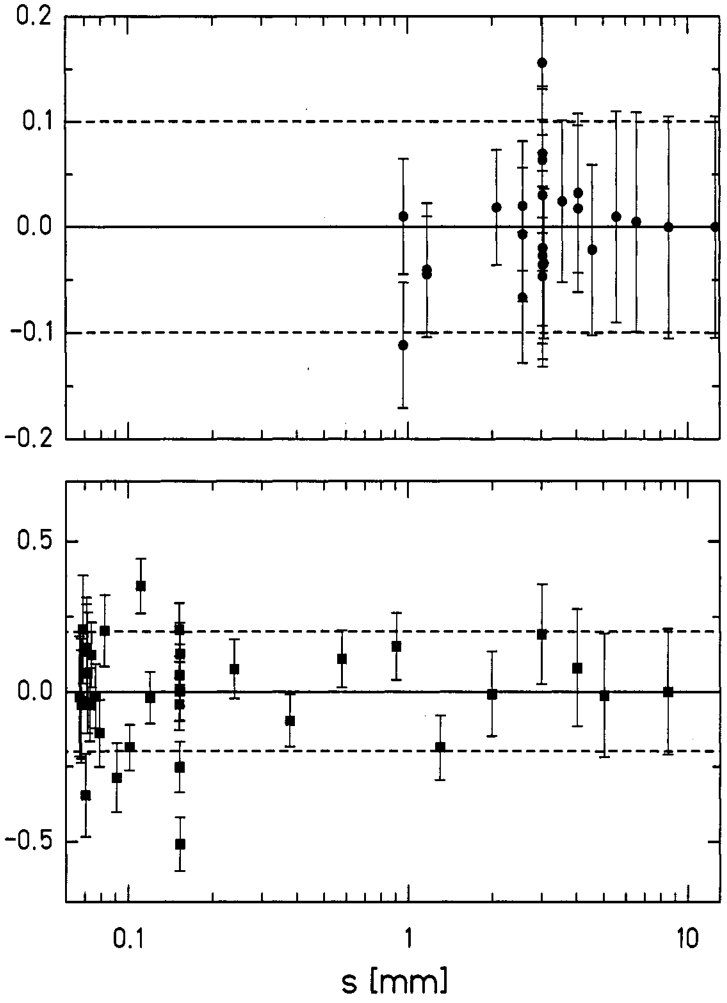

Figure 6.1: The results of the Newtonian fit for the phases $\overline{\pi}$ and $\overline{\pi}'$. The dashed lines show the constraints put on these values from Section 5.3.1. We observe no systematic variation of phase with s. The points at $s \approx 3$ mm in the upper panel and $s \approx 150$ μm in the lower panel are centering runs, where the equilibrium position of our pendulum changed with horizontal displacement. This slight change was due to either an electrostatic interaction or an optical misalignment, and these parameters were able to account for this change in our fit.

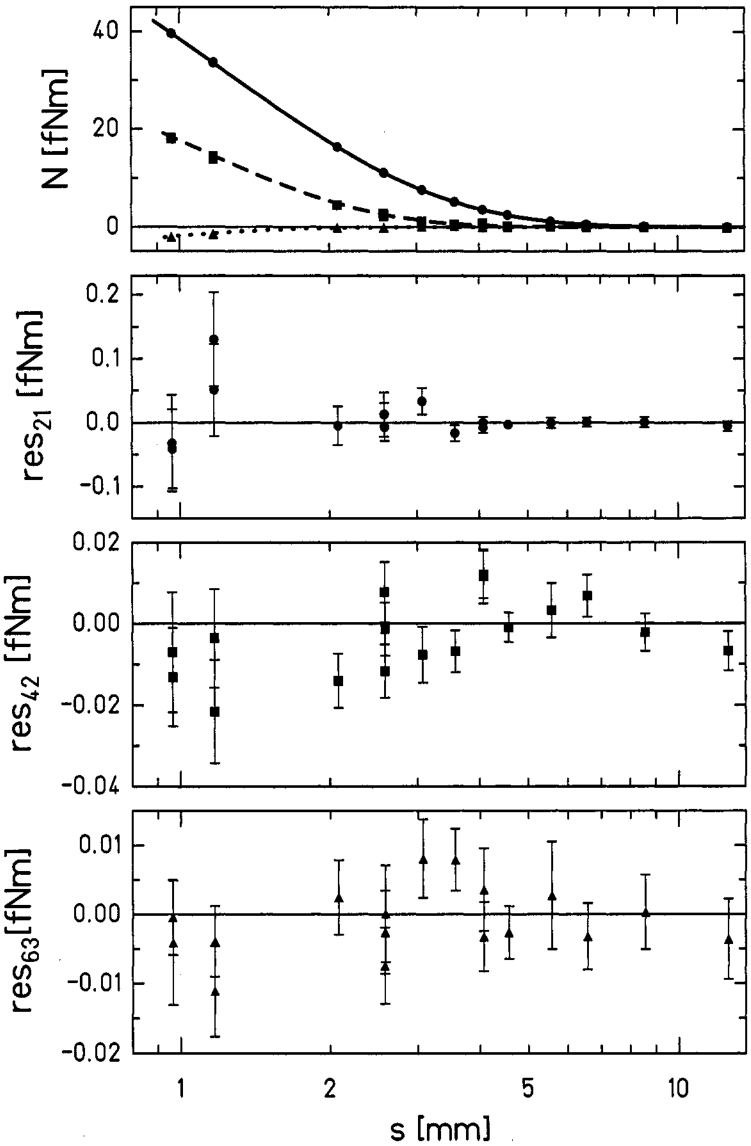

Figure 6.2: The upper panel shows the data and fit for the upper-attractor-only data runs vs. s. $m = 21$ torques are indicated with circles and a solid line; $m = 42$ torques are indicated with squares and a dashed line; $m = 63$ torques are indicated with triangles and a dotted line. In the upper panel the $m = 42$ ($m = 63$) torques have been scaled by a factor of 30 (20) to appear on the same scale. The fit residuals for the three harmonics are shown in the lower panels. The errors for $m = 21$ torques increase at small s because of the second term in Equation 6.2

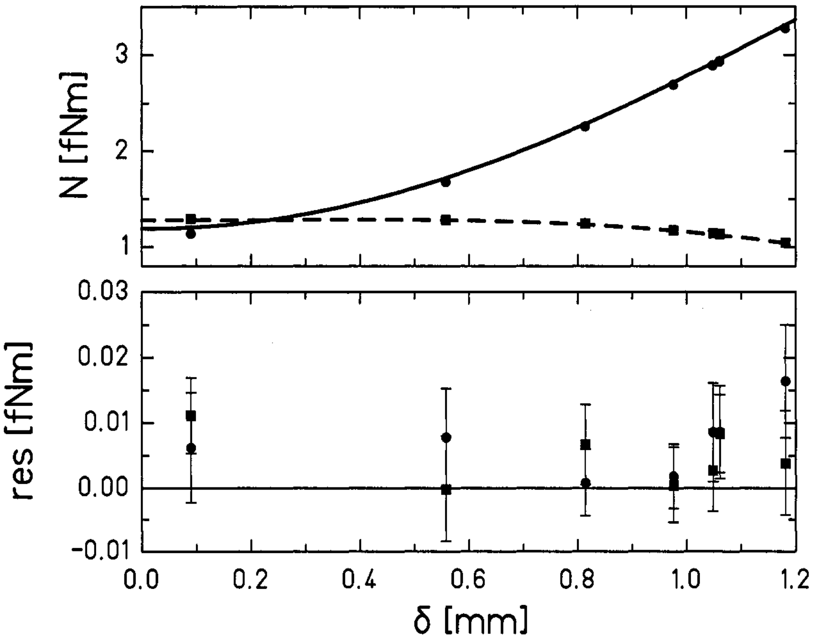

Figure 6.3: The upper panel shows the data and fit for the two-attractor data runs vs. axial displacement, δ. $m = 21$ torques are indicated with circles and a solid line; $m = 42$ torques are indicated with squares and a dashed line; $m = 63$ torques were not fit for these centering runs. In the upper panel, $m = 21$ torques have been multiplied by -1 to simplify the display. The fit residuals for the two harmonics are shown in the lower panel.

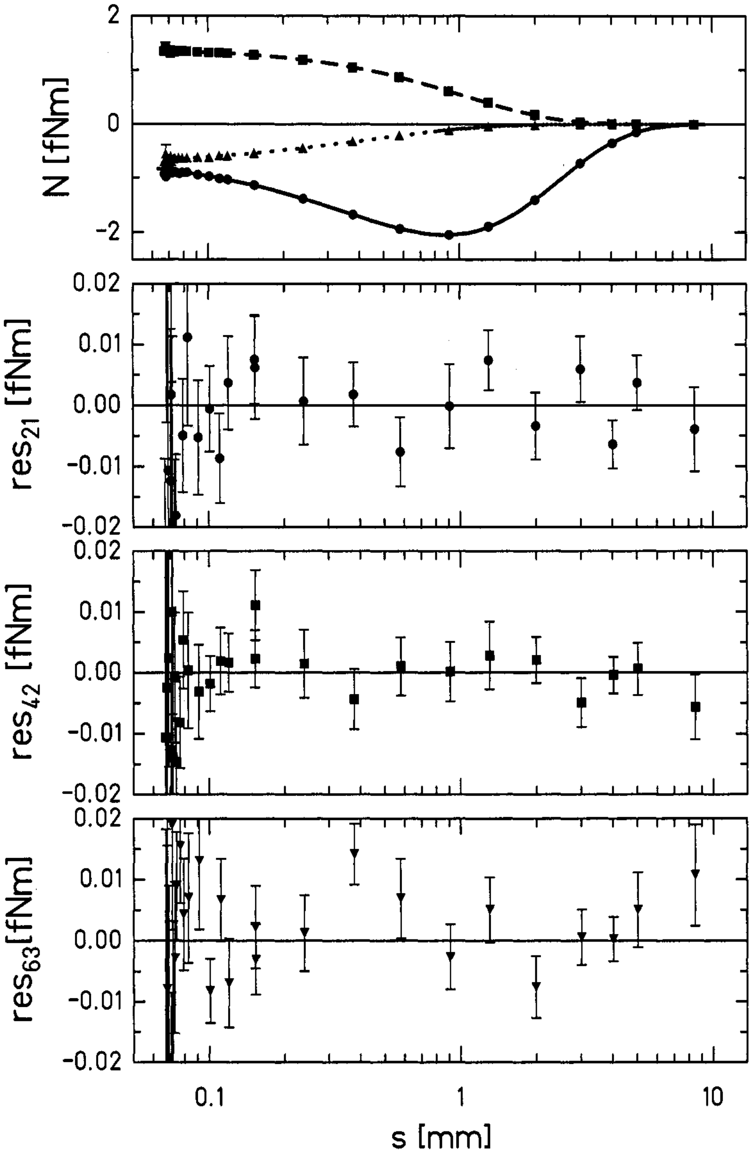

Figure 6.4: The upper panel shows the data and fit for the two-attractor data runs vs. s. $m = 21$ torques are indicated with circles and a solid line; $m = 42$ torques are indicated with squares and a dashed line; $m = 63$ torques are indicated with triangles and a dotted line. The fit residuals for the three harmonics are shown in the lower panels. The full scale of the residuals is not shown to highlight the residuals at large s. Figure 6.5 shows the same residuals, but highlighting those data points at small s.

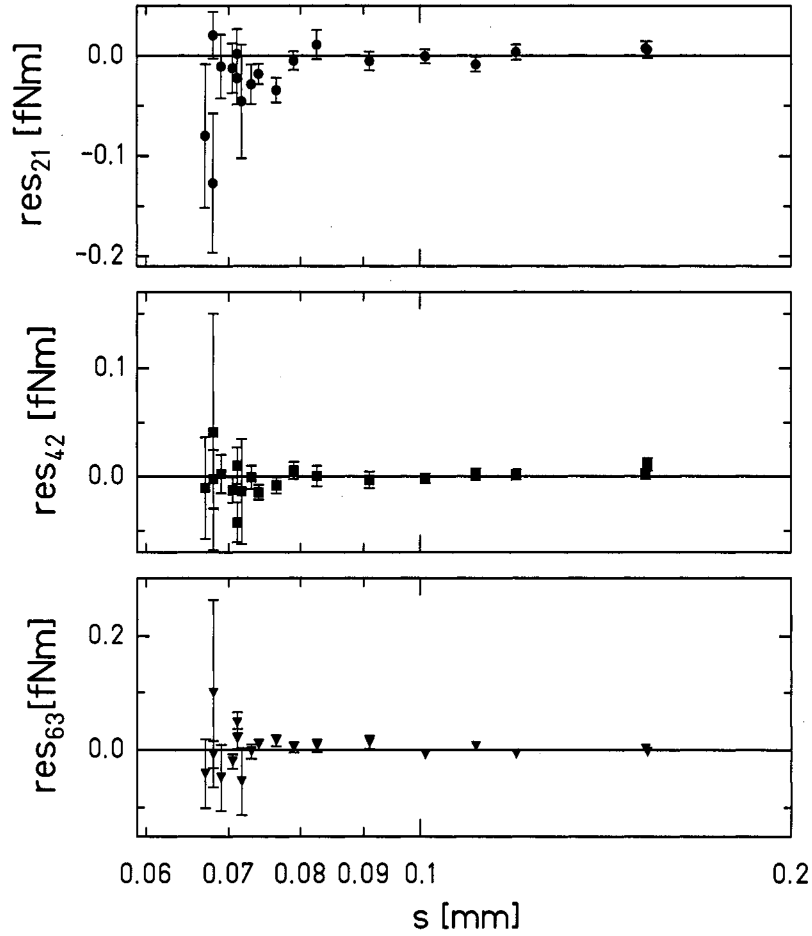

Figure 6.5: The same residuals as in Figure 6.4, but plotted with different ranges to highlight data points with small *s*. The data points with obvious large uncertainties are for run2039 and run2012, at $s = 0.068$ mm; only six and five subcuts, respectively, survived our rejection criteria in these runs, and the large error bars reflect this low number - a typical number of subcuts for a data run at large *s* was ~ 25.

6.3 Results of Fits Including Non-Newtonian Contributions

We fit our data with the Newtonian model plus an additional term due to each of the new-physics potentials discussed in Chapters 1 and 4. Our data revealed a resolved (> 95% confidence) non-Newtonian contribution to our torques.

6.3.1 Experimental Sensitivity and Exclusion vs. Inclusion Confidence Intervals

The following analysis provides several different measures of our data. We discuss those measures here in the context of a Yukawa interaction, though these definitions apply to the other non-Newtonian potentials as well. This discussion follows Chapter 15 of Reference [39].

We defined the *sensitivity*, $S(\lambda)$, of our experiment to a given Yukawa length scale, λ, as follows. We fit our data to Newtonian gravity plus a Yukawa term of length scale, λ, as shown in Equation 1.1, and extracted $\alpha_{bf} \pm \sigma$, the best-fit strength of the Yukawa violation and its 68% uncertainty; we defined $S(\lambda) \equiv 2\sigma$. This sensitivity indicated at what level we *could have* set a 95% confidence region, had our result been entirely inconsistent with a non-Newtonian contribution. The uncertainty $\sigma = \sqrt{C_{\alpha\alpha}}$, where $C_{\alpha\alpha}$ is the diagonal element of our covariance matrix which corresponds to α; because our errors are Gaussian, this is equivalent to looking for the points around α_{bf} where χ^2 increased by 1 when fixing α to a new value and refitting our data. We used this measure of sensitivity only to understand our results through Monte Carlo simulations, as discussed in Section 6.3.3.

The 95% (65%) *exclusion* confidence interval is indicated as $|\alpha_{95}|$ ($|\alpha_{68}|$). We can state with 95% (68%) confidence that our data is inconsistent with a Yukawa violation where $|\alpha| > |\alpha_{95}|$ ($|\alpha_{68}|$). We calculate these intervals separately for each λ by finding the best fit value of α and then finding the values of $|\alpha_{95}|$ ($|\alpha_{68}|$) that satisfy

$$0.95\ (0.68) = \int_{-|\alpha_{95}|\ (-|\alpha_{68}|)}^{+|\alpha_{95}|\ (+|\alpha_{68}|)} N(\alpha_{bf}, \sigma) d\alpha \tag{6.4}$$

where $N(x_0, \sigma)$ is the normal distribution centered at x_0 with width, σ. These exclusion limits are independently calculated for each value of λ and satisfy the theorist's inquiry : "I have a theory that predicts a length scale, λ. What strengths are inconsistent with experiment?" The answer is $|\alpha| > |\alpha_{95}|$ ($|\alpha_{68}|$) at the 95% (68%) confidence level. We can provide these numbers despite our resolved signal, because our resolved signal, α_{bf} is always below these limits.

To calculate *inclusion* confidence intervals, we can no longer treat each λ separately. We know there is a best-fit $(\alpha_{bf}, \lambda_{bf})$, which gives the lowest value of $\chi^2 = \chi^2_{min}$; we want to calculate the boundary in the 2-dimensional (α, λ)-space that represents our 95% (68%) confidence interval. We run our fit, by freezing (α,λ) at various values, and search for those values where the returned $\chi^2 = \chi^2_{min} + 2.3$ (6.17) for the 95% (68%) boundaries. These boundaries serve as 2-dimensional error bars on our measurement of a violation of Newtonian gravity.

6.3.2 Yukawa Potentials

Table 6.2 shows the results from fitting an additional Yukawa potential, as in Equation 4.19. There is a resolved strength, α, at nearly every λ, with the best fit occuring at $(\alpha, \lambda) = (-62.1, 30\ \mu\text{m})$. Table 6.2 contains the 95% *exclusion* constraints, $|\alpha_{95}|$ and are shown in Figure 6.6. Because we had a resolved signal, we were able to calculate *inclusion* limits, where we have calculated a boundary in (α, λ) space representing the 68% and 95% confidence regions. Table 6.3 and Figure 6.7 show these inclusion constraints.

Table 6.2: Constraints on α from Equation 1.1, showing the best-fit value and its uncertainty; the 68% and 95% confidence limits on $|\alpha|$; and the χ^2 and the Q from that best fit.

λ [mm]	α_{bf}	±	σ	$\|\alpha_{68}\|$	$\|\alpha_{95}\|$	χ^2	Q
0.005	-1.1×10^9	±	5.5×10^8	1.4×10^9	2.0×10^9	358.9	0.24
0.010	−173000	±	55300	199000	264000	354.0	0.30
0.015	−5170	±	1460	5860	7570	351.9	0.33

continued on following page

Table 6.2 continued.

λ [mm]	α_{bf}	$\pm$	σ	$\lvert\alpha_{68}\rvert$	$\lvert\alpha_{95}\rvert$	χ^2	Q
0.020	−683	±	182	769	983	350.8	0.35
0.025	−173	±	45	194	247	350.4	0.35
0.030	−62.1	±	16.2	69.7	88.8	350.4	0.35
0.035	−27.6	±	7.3	31.0	39.6	350.7	0.35
0.040	−14.1	±	3.8	15.9	20.4	351.1	0.34
0.045	−8.01	±	2.22	9.05	11.66	351.7	0.33
0.050	−4.88	±	1.39	5.54	7.17	352.3	0.32
0.055	−3.15	±	0.92	3.58	4.67	353.0	0.32
0.060	−2.13	±	0.64	2.43	3.19	353.6	0.31
0.065	−1.49	±	0.47	1.70	2.25	354.3	0.30
0.070	−1.07	±	0.35	1.23	1.64	354.9	0.29
0.075	−0.79	±	0.27	0.92	1.23	355.4	0.28
0.080	−0.60	±	0.21	0.70	0.94	355.9	0.28
0.090	−0.36	±	0.13	0.43	0.58	356.9	0.27
0.095	−0.29	±	0.11	0.34	0.47	357.3	0.26
0.100	−0.23	±	0.09	0.28	0.38	357.6	0.26
0.125	−0.09	±	0.04	0.11	0.16	359.1	0.24
0.150	−0.046	±	0.023	0.057	0.084	360.0	0.23
0.175	−0.026	±	0.014	0.033	0.049	360.6	0.22
0.200	−0.016	±	0.009	0.021	0.032	361.0	0.22
0.250	−0.008	±	0.005	0.011	0.017	361.4	0.21
0.500	−0.0020	±	0.0014	0.0026	0.0042	361.8	0.21
1.000	−0.0022	±	0.0012	0.0028	0.0042	360.8	0.22
1.500	−0.0047	±	0.0020	0.0057	0.0080	358.2	0.25
2.000	−0.008	±	0.003	0.010	0.013	355.4	0.28

continued on following page

Table 6.2 continued.

λ [mm]	α_{bf}	$\pm$	σ	$\|\alpha_{68}\|$	$\|\alpha_{95}\|$	χ^2	Q
2.500	−0.010	±	0.003	0.011	0.015	354.3	0.30
3.000	−0.010	±	0.003	0.012	0.016	354.4	0.30
3.500	−0.010	±	0.003	0.011	0.015	355.0	0.29
4.000	−0.009	±	0.003	0.011	0.015	355.7	0.28
4.500	−0.008	±	0.003	0.010	0.014	356.7	0.27
5.000	−0.009	±	0.003	0.011	0.014	355.8	0.28
5.500	−0.009	±	0.003	0.010	0.014	356.2	0.28
6.000	−0.008	±	0.003	0.010	0.013	356.8	0.27
7.000	−0.008	±	0.003	0.009	0.013	357.6	0.26
10.000	−0.008	±	0.003	0.009	0.013	356.9	0.27

6.3.3 Monte Carlo Simulations

We conducted several Monte Carlo studies of our experiment to confirm the combined behavior of our data and our fitting function. For these studies, we randomly chose a set of instrumental parameters that were part of a Gaussian distribution around our nominal measured parameters, $\vec{\eta}$, where the measured uncertainties in these parameters, $\delta\vec{\eta}$, set the width of the Gaussian for each parameter. From these parameters and the same pendulum positions of our real data set, we created simulated data sets; the simulated data sets included both centering runs and data runs where we ran with just the upper attractor. We added Gaussian noise to the z-positions of our fake data runs to simulate the uncertainty due to our micrometer readout; we also added an uncertainty to the phase of each run, to simulate the effect covered by the parameters $\vec{\pi}$ and $\vec{\pi}'$. We queried our fitting function for torque components given the simulated positions and instrumental parameters, and added to these components the same noise we observed in the real data. Each study repeated this procedure many times, producing many simulated data sets.

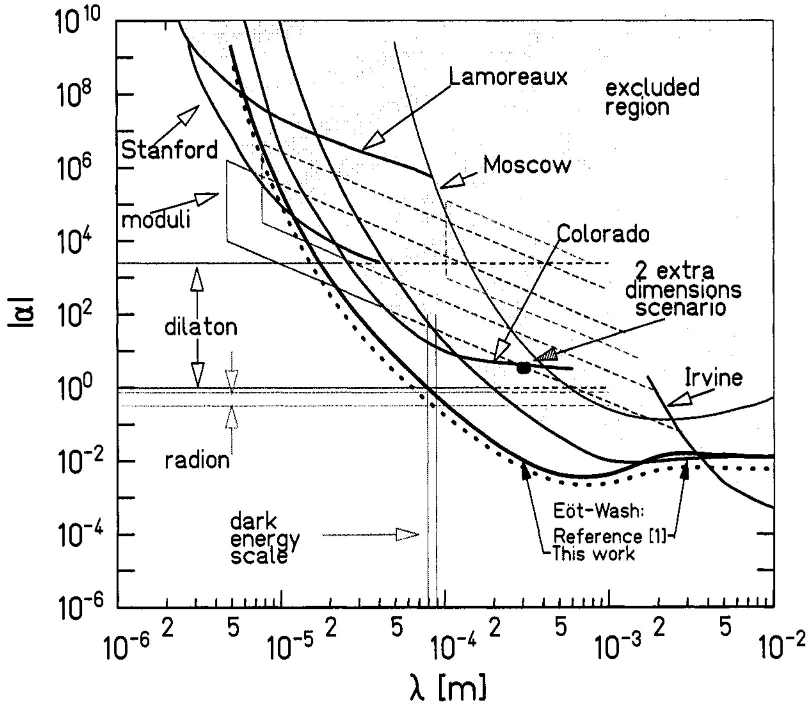

Figure 6.6: Shown as the solid line are the 95% exclusion limits on $|\alpha|$. The dotted line is our sensitivity, $S(\lambda)$, as defined in Section 6.3.1, and is included to show the sensitivity of this experiment (had the results been null), and as a common reference for further figures. The difference between the two lines is the effect of our resolved signal on these exclusion limits. Even our sensitivity decreases beyond $\lambda \approx 1$ mm, as long range Yukawa potentials are canceled by our lower attractor.

Table 6.3: Inclusion Constraints on α at the 68% and 95% confidence level, calculated by looking for a rise in χ^2 of 2.3 and 6.17 above the minimum ($\chi^2_{min} = 350.4$), respectively, in this parameter space. Those λ where the minimum χ^2 does not meet this constraint do not appear in this table. Some λ are included at the 95% confidence level, but all χ^2 at that λ are above $\chi_{min} + 2.13$.

λ	$-\alpha_{95}$	$-\alpha_{68}$	$+\alpha_{68}$	$+\alpha_{95}$
0.010	−267000	N/A	N/A	−86400
0.015	−8440	−6470	−3860	−2000
0.020	−1130	−933	−428	−237
0.025	−285	−241	−102	−57.1
0.030	−102	−86.6	−36.8	−20.5
0.035	−45.2	−37.9	−16.9	−9.28
0.040	−23.0	−18.9	−9.22	−4.99
0.045	−12.8	−10.2	−5.75	−2.98
0.050	−7.72	−5.70	−4.02	−1.95
0.055	−4.88	N/A	N/A	−1.36
0.060	−3.22	N/A	N/A	−0.992
0.065	−2.19	N/A	N/A	−0.760
0.070	−1.52	N/A	N/A	−0.607
0.075	−1.08	N/A	N/A	−0.501
0.080	−0.809	N/A	N/A	−0.390
2.000	−0.011	N/A	N/A	−0.005
2.500	−0.015	N/A	N/A	−0.005
3.000	−0.015	N/A	N/A	−0.005
3.500	−0.014	N/A	N/A	−0.006
4.000	−0.013	N/A	N/A	−0.006
5.000	−0.012	N/A	N/A	−0.006
5.500	−0.012	N/A	N/A	−0.006

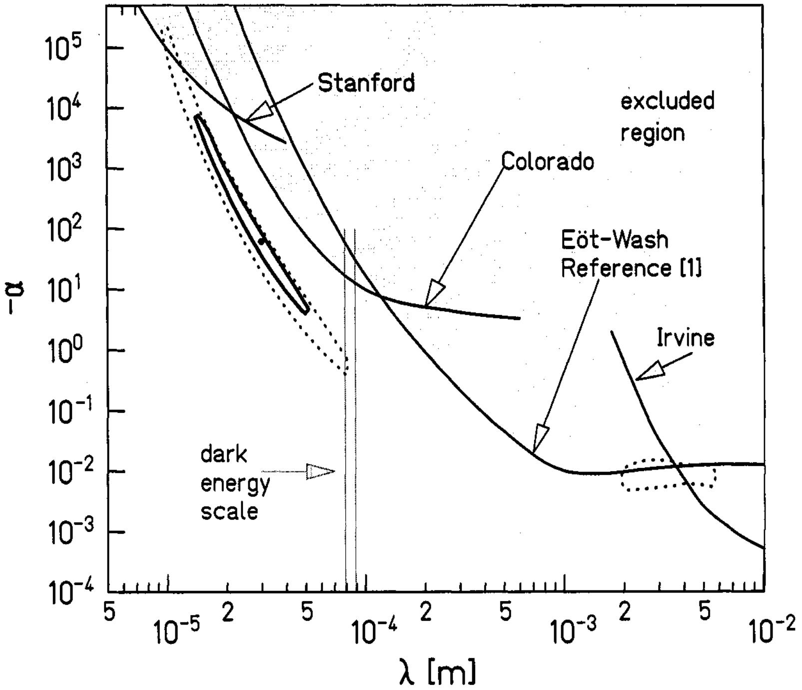

Figure 6.7: Shown are the 68% (solid line) and 95% (dotted line) confidence intervals for a Yukawa violation. Theoretical predictions which require an attractive additional term ($\alpha > 0$) are not shown on this plot. The constraints shown from previous experiments are the quoted 95% limits on $|\alpha|$. The best fit is shown as the filled circle.

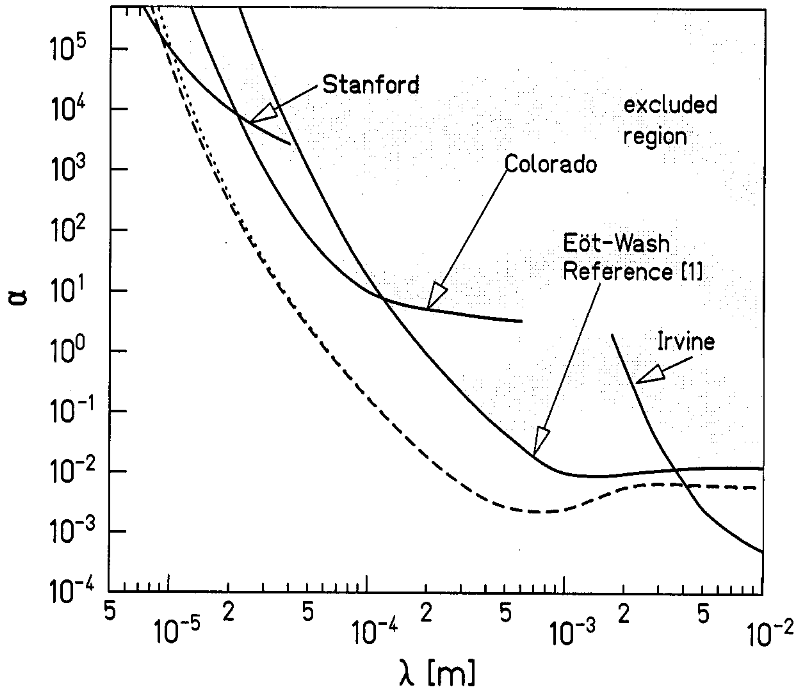

Figure 6.8: A comparison of our observed sensitivity (dotted line) with the average sensitivity of 100 simulated data sets (dashed line.) Beyond $\lambda = 50$ μm, the curves are indistinguishable.

We conducted our first study to check the observed sensitivity of our experiment. We simulated 100 data sets with only a Newtonian input signal. For each of these simulated data sets, we fit to each of the calculated Yukawa potentials; this gave us a distribution of best-fit strengths, $\alpha \pm \sigma$, for each λ. By averaging the results from all of these simulations, the most resolved signal was at $\lambda = 5.5$ mm with $\alpha = (4.0 \pm 3.0) \times 10^{-4}$; our fit did not inherently prefer any new signal. We compared the average sensitivity (2σ) of these 100 data sets to our observed sensitivity. Figure 6.8 shows that this study agreed gratifyingly well with our observed sensitivity, $S(\lambda)$.

We next wanted to understand the size and shape of our inclusion boundaries. We simulated 100 data sets with an input of $(\alpha, \lambda) = (-60, 30$ μm$)$ on top of our Newtonian

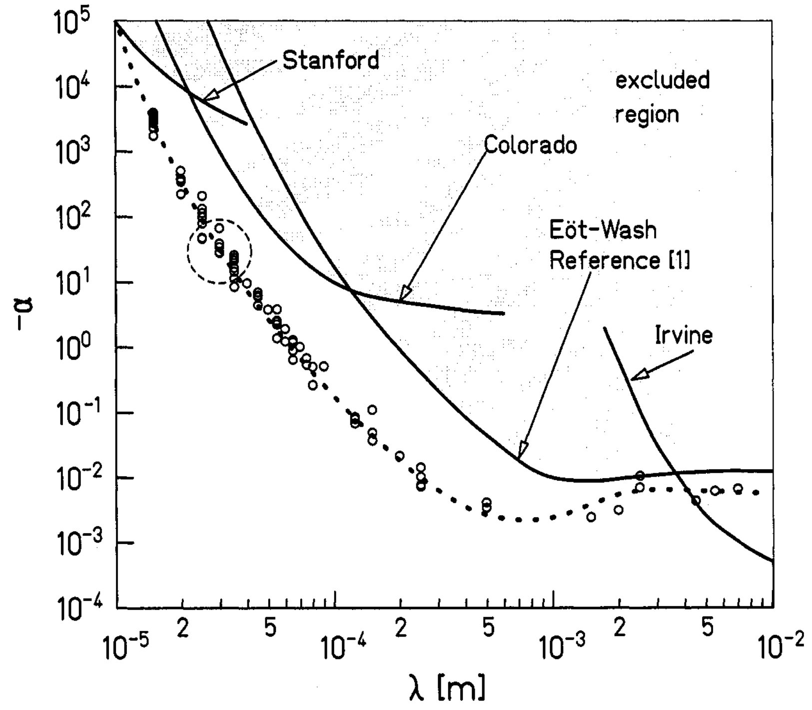

Figure 6.9: A Monte Carlo simulation of our data with 100 simulated data sets, created with a Newtonian model plus a Yukawa coupling with $(\alpha, \lambda) = (-30, 30\ \mu\text{m})$ (the input value is at the center of the dotted circle.) Each circle shows the best-fit Yukawa for one simulated data set. This distribution is very broad in λ because the input Yukawa coupling was close to our sensitivity (the dotted line).

signal, similar to the (α, λ) that gave us our best χ^2 for a Yukawa interaction. For each of these simulated data sets, we recorded the best-fit value of (α, λ). The distribution of these best-fit values is shown in Figure 6.10; we observe that the simulated distribution has a similar shape to our actual observed inclusion boundaries. We speculated that our inclusion boundaries were so extensive because the resolved signal was so close to our experimental sensitivity. To test this, we simulated 100 data sets with an input of $(\alpha, \lambda) = (-300, 30\ \mu\text{m})$ and 100 data sets with an input of $(\alpha, \lambda) = (-30, 30\ \mu\text{m})$ on top of our Newtonian signal; Figures 6.9 and 6.11 show that the inclusion boundary becomes broader the closer the input signal is to our sensitivity.

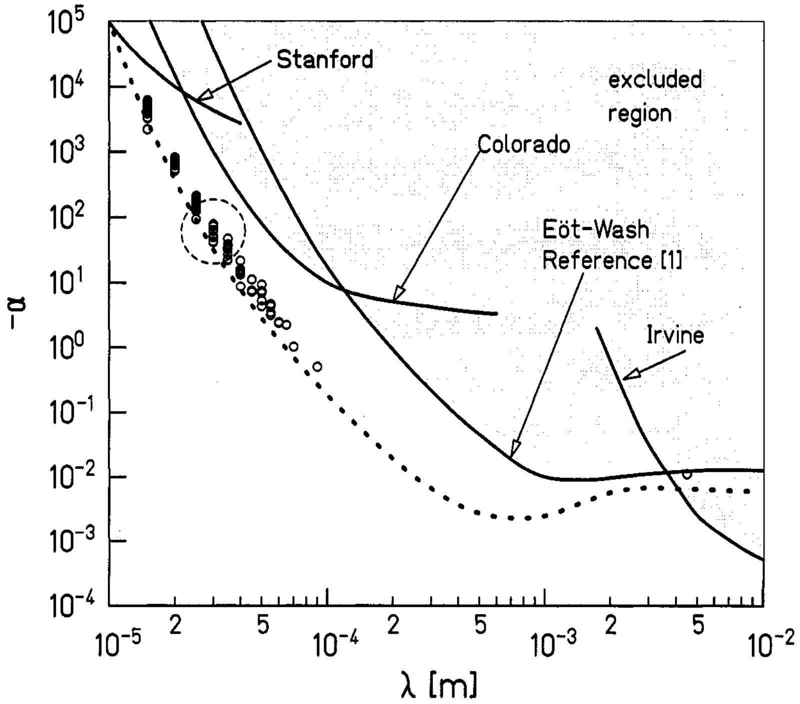

Figure 6.10: A Monte Carlo simulation of our data with 100 simulated data sets, created with a Newtonian model plus a Yukawa coupling with $(\alpha, \lambda) = (-60, 30\ \mu\text{m})$. Each circle shows the best-fit Yukawa for one simulated data set. The dotted line is our observed sensitivity, and the input value is at the center of the dotted circle.

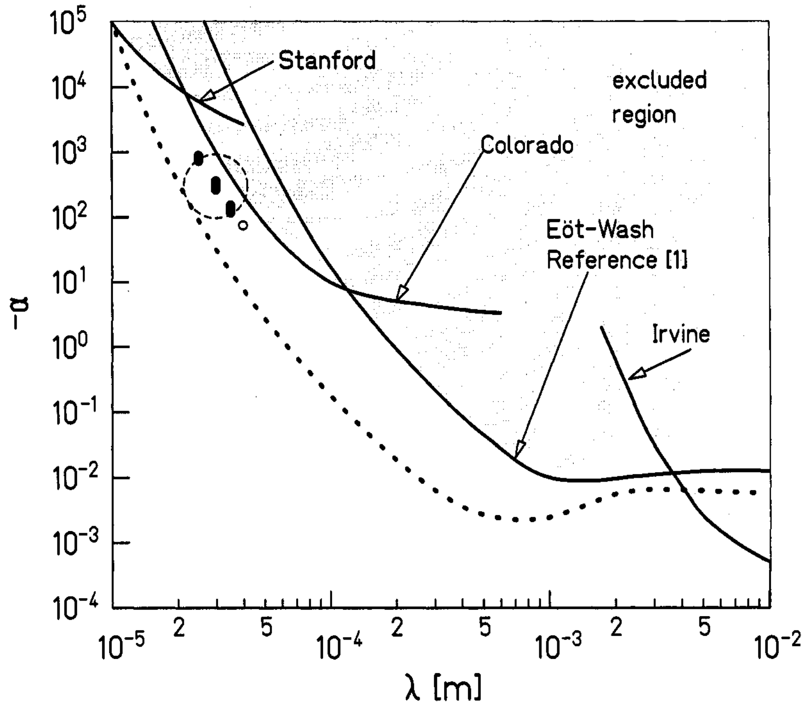

Figure 6.11: A Monte Carlo simulation of our data with 100 simulated data sets, created with a Newtonian model plus a Yukawa coupling with $(\alpha, \lambda) = (-300, 30\ \mu\text{m})$. Each circle shows the best-fit Yukawa for one simulated data set. The dotted line is our observed sensitivity, and the input value is at the center of the dotted circle.

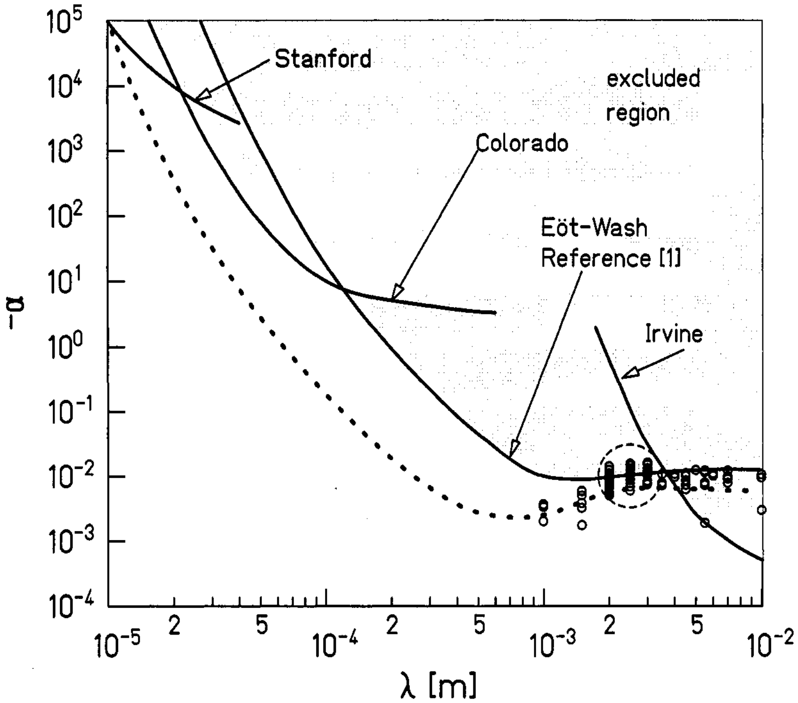

Figure 6.12: A Monte Carlo simulation of our data with 100 simulated data sets, created with a Newtonian model plus a Yukawa coupling with $(\alpha, \lambda) = (-0.01, 2.5 \text{ mm})$. Each circle shows the best-fit Yukawa for one simulated data set. The dotted line is our observed sensitivity, and the input value is at the center of the dotted circle.

Finally, because there was a smaller region of (α, λ)-space centered at $(-0.01, 2.5\text{mm})$, we simulated 100 data sets with this Yukawa signal on top of our Newtonian signal. Figure 6.12 shows that this input value of (α, λ) unambiguously prefers the input range, while our data has an allowed region more comparable to our best-fit value as shown in Figure 6.10.

These Monte Carlo studies were meant only to understand the combined behavior of our data and fitting function and were not used in any other way for our analysis.

Table 6.4: Constraints on β_k from Equation 1.13, showing the best-fit value and its uncertainty; the 68% and 95% confidence limits on $|\beta_k|$; and the χ^2 and the Q from that best fit.

k	β_{BF}	$\pm$	σ	$\lvert\beta_{68}\rvert$	$\lvert\beta_{95}\rvert$	χ^2	Q
2	−0.00082	±	0.00044	0.00102	0.00153	360.5	0.22
3	−0.00033	±	0.00017	0.00041	0.00061	360.2	0.23
4	−0.00017	±	0.00007	0.00020	0.00029	358.7	0.24
5	−0.00007	±	0.00002	0.00009	0.00011	355.2	0.29

6.3.4 Power-Law Potentials

Table 6.4 shows the results from fitting an additional power law potential, as in Equation 4.22.

6.3.5 Massive Pseudoscalar Potentials

Table 6.5 shows the results from fitting an additional massive pseudoscalar potential, as in Equation 4.25. The interpolated best fit for these potentials is $\lambda \approx 0.06$ mm ($mc^2 = 3.3$ meV).

6.3.6 Fat Graviton Potentials

Figure 6.13 shows the results from fitting an additional fat-graviton potential, as in Equation 1.9. Unlike the Yukawa interaction, the strength of this new potential is fixed to be identically opposite to Newtonian gravity, and there is only one degree of freedom, λ_g. Figure 6.13 shows how χ^2 varies with λ_g, giving an interpolated best fit of $\lambda_g = 0.142$ mm with $\lambda_g \in [0.133, 0.149]$ mm at the 68% confidence level and $\lambda_g \in [0.123, 0.155]$ mm at the 95% confidence level.

Table 6.5: Constraints on γ from Equation 4.25, showing the best-fit value and its uncertainty; the 68% and 95% confidence limits on $|\gamma|$; and the χ^2 and the Q from that best fit.

λ [mm]	mc^2 [meV]	γ_{BF}	±	σ	$\lvert\gamma_{68}\rvert$	$\lvert\gamma_{95}\rvert$	χ^2	Q
0.020	9.85	−692	±	217	793	1049	352.9	0.32
0.030	6.57	−25.8	±	7.5	29.3	38.2	352.6	0.32
0.040	4.93	−5.04	±	1.33	5.66	7.23	350.2	0.32
0.050	3.94	−1.70	±	0.44	1.91	2.42	349.8	0.36
0.075	2.63	−0.289	±	0.074	0.323	0.410	349.9	0.36
0.100	1.97	−0.133	±	0.035	0.149	0.191	350.9	0.36
0.200	0.985	−0.020	±	0.006	0.022	0.030	353.9	0.30
0.500	0.394	−0.0028	±	0.0012	0.0033	0.0047	358.6	0.25
1.000	0.197	−0.0011	±	0.0005	0.0013	0.0020	360.1	0.24
2.000	0.0985	−0.0007	±	0.0004	0.0009	0.0013	360.6	0.22
3.000	0.0657	−0.0007	±	0.0004	0.0008	0.0012	360.6	0.22
5.000	0.0394	−0.0006	±	0.0003	0.0008	0.0012	360.5	0.22
10.000	0.0197	−0.0006	±	0.0003	0.0008	0.0012	360.5	0.22

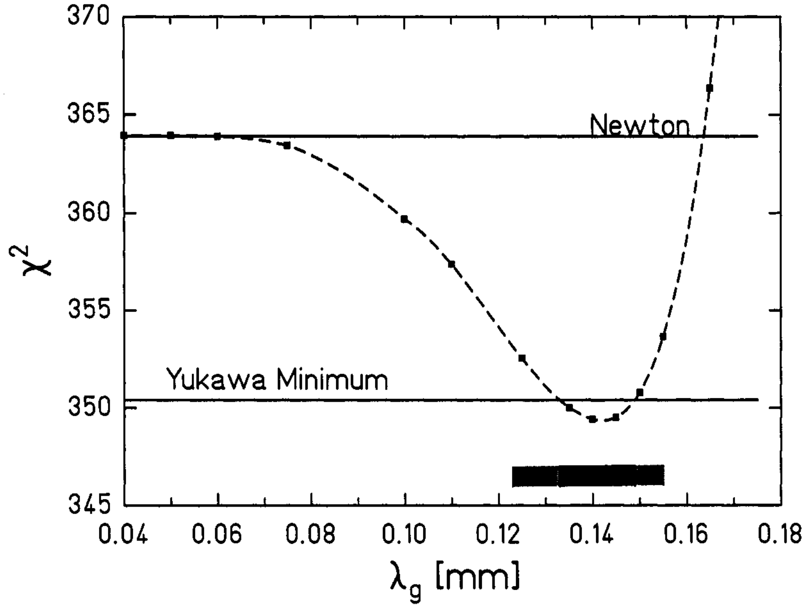

Figure 6.13: χ^2 as a function of λ_g, the fat graviton length scale. The Newtonian χ^2 and the best-fit Yukawa χ^2 are shown as the labeled horizontal lines. The dark and light shaded regions indicate the 68% and 95% confidence regions in λ_g, respectively.

Chapter 7

CONCLUSIONS

This experiment measured a signal above the Newtonian background. Further measurements are clearly required to establish whether this signal is "new physics" or whether there is some other cause for this discrepancy. Chapter 5 details the systematics we considered in this experiment and none of these is able to explain our observed signal. This chapter discusses first, the theoretical implications of this signal as if it were "new physics" and the constraints placed by our exclusion limits, which assume this signal is not due to a new interaction; the second half discusses the limitations of this experiment and plans for the future.

7.1 Theoretical Implications

Our results from fitting additional potentials along with our Newtonian model from Chapter 6 can be interpreted in the theoretical frameworks discussed in Chapter 1.

7.1.1 Yukawa Violations

Except for the exchange of vector gauge bosons, the Yukawa couplings discussed in Chapter 1 are responsible for *attractive* potentials, those with the same sign as Newtonian gravity. Our signal indicates a *repulsive* force, whose strength relative to gravity, α, does not appear to agree well with the vector gauge boson prediction (Reference [18]) that $\alpha \geq 10^6$ for masses in the meV range ($\lambda \in [10, 100]$ μm), as shown in Figure 6.7. We interpret our results for these models by setting constraints on these models, given our exclusion limits, $|\alpha_{95}|$.

Extra Dimensions

From Equations 1.2 and 1.3, we can limit the size of the single largest extra dimension, for which we expect an *attractive* interaction with $\alpha = 8/3$ to be $R_* \leq 63\ \mu$m. If two extra dimensions were large and had the same size, our results require that $R_* \leq 53\ \mu$m, which then requires that the new unification scale $M_* \geq 2.4$ TeV.

New Boson-Exchange Forces

We can constrain a radion-mediated force by comparing Equation 1.11 to our 95% exclusion limits. For 2 extra dimensions, the radion is expected to mediate a force with strength 1/2 that of gravity, and we can constrain the unification mass $M_* \geq 5.1$ TeV. For six extra dimensions, the radion mediates a force with strength 3/4 times that of gravity and we constrain $M_* \geq 5.3$ TeV.

If the dilaton had its smallest predicted coupling, $\alpha = 1$, we constrain its mass to be ≥ 2.5 meV; for a large coupling, $\alpha = 1000$, its mass must be ≥ 9.9 meV.

Coupling to Baryon and Lepton Number

Up to this point, we have assumed that an additional coupling between our detector and attractor rings couples to mass, like Newtonian gravity, but there are other possibilities. Baryon number and lepton number are two quantities that appear to be conserved in nature, yet have no known force associated with them. Equivalence principle tests, like Reference [42], search directly for these sorts of interactions. Our experiment is also sensitive to these interactions which are of the form

$$V(r) = -\frac{Gm_1m_2}{r}\left(1 + \alpha_5\,[q_5]_1\,[q_5]_2\,e^{-r/\lambda}\right) \tag{7.1}$$

where the subscripts 1 and 2 refer to the detector and one attractor, α_5 is the strength of the new interaction, and q_5 is the charge to which the interaction couples. For baryon-number-coupled interactions $q_5 = B/\mu \approx 1$, where B/μ is the number of baryons per atomic mass unit; our constraints on α_5 for these interactions are the same as for α in Section 6.3.2. When $q_5 = L/\mu$, where L is lepton number, $\alpha = (0.4378)^2\,\alpha_5$, where we

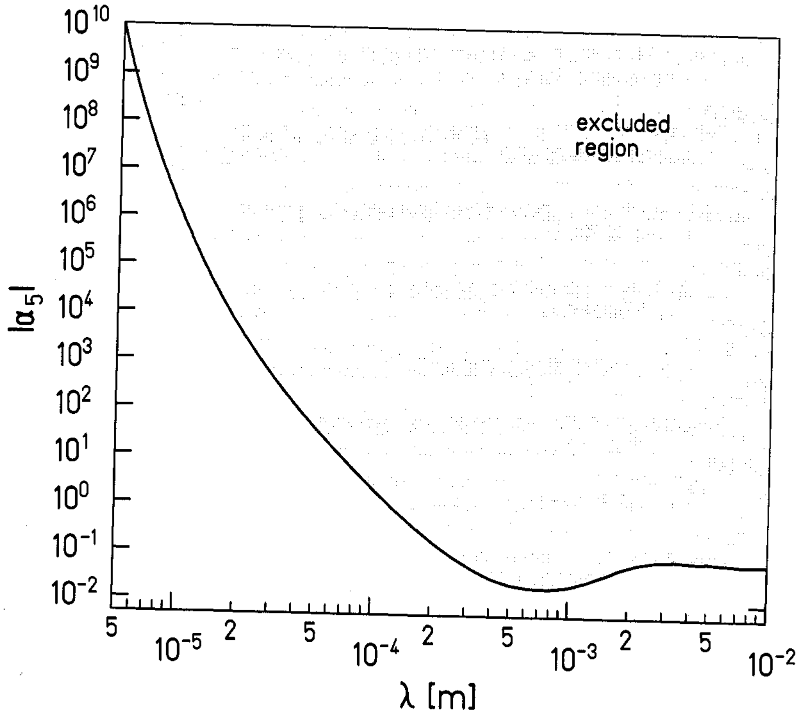

Figure 7.1: Our 95% exclsuion limits on $|\alpha_5|$ for coupling to lepton-number density. These constraints differ from those shown in Figure 6.6 predominantly by the multiplicative factor $[L/\mu]_{\mathrm{Mo}}[L/\mu]_{\mathrm{Mo}}$; at longer ranges, the different lepton-number density of the lower attractor makes a minor difference.

have put in the value for L/μ for a molybdenum attractor and detector. This equality only holds for $\lambda \lesssim 1.0$ mm, the thickness of our moybdenum upper attractor; beyond that range, we must consider the different lepton-number densities for molybdenum and tantalum. To account for this, we weighted the Yukawa strengths of the two attractors in our fit, so that the lower attractor always couples with strength 0.921× that of the upper attractor. ($[L/\mu]_{\mathrm{Ta}} = 0.921 \times [L/\mu]_{\mathrm{Mo}} = 0.4034$.) Figure 7.1 shows our 95% exclusion limits while Figure 7.2 shows our inclusion confidence boundaries from this procedure. Our results are consistent with a vector interaction coupled to lepton number.

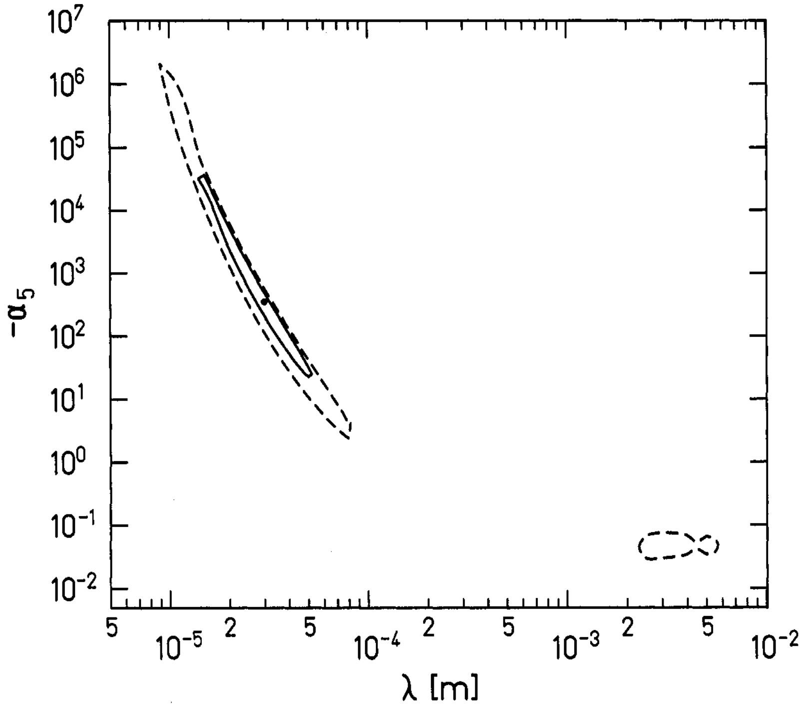

Figure 7.2: Our 68% (solid line) and 95% (dotted line) inclusion limits on α_5 for coupling to lepton-number density. These constraints differ from those shown in Figure 6.7 predominantly by the multiplicative factor $[L/\mu]_{\mathrm{Mo}}[L/\mu]_{\mathrm{Mo}}$; at longer ranges, the different lepton-number density of the lower attractor makes a minor difference.

7.1.2 Pseudoscalar Constraints

We can constrain the γ_5 couplings of massless pseudoscalars to baryons by using a variant of our constraints on β_3 from Table 6.5, as discussed in Reference [1]. Our two attractor rings were made of different materials, which complicates the interpretation of β_3 in this way. Because our new signal was apparently of a range smaller than the thickness of our upper attractor ring, we assumed that the exchange of pseudoscalars was due to the upper ring alone. Our new limits are shown in Figure 7.3.

One can create a figure, similar to Figure 7.3 for any given mass of a massive pseudoscalar. For simplicity, we provide here a scaling factor as a function of pseudoscalar mass by which one should multiply the constrints from Figure 7.3 to obtain the appropriate bounds; this scaling factor is shown in Figure 7.4.

7.1.3 Fat Graviton Constraints

The fat graviton scenario predicts that Newtonian gravity turns off below a length scale, λ_g. If our data were interpreted in this model $\lambda_g = 142 \pm 8$ μm, where λ_g is defined in Equation 1.9

7.2 Other Considerations

We are currently investigating whether there are components of the Casimir Effect that are not shielded by our conducting membrane and are possibly repulsive, as described in References [43] and [44]. The geometry of our experiment, along with the interposition of our conducting membrane, is more complex than those of typical Casimir Effect calculations, and the scale of these effects remains to be seen. We can repeat these tests with lower density materials (probably aluminum); if the effect is gravitational, it will scale with the densities of our test masses, but if the effect is electromagnetic, like the Casimir Effect, it will differ with the different electrical properties of molybdenum and aluminum.

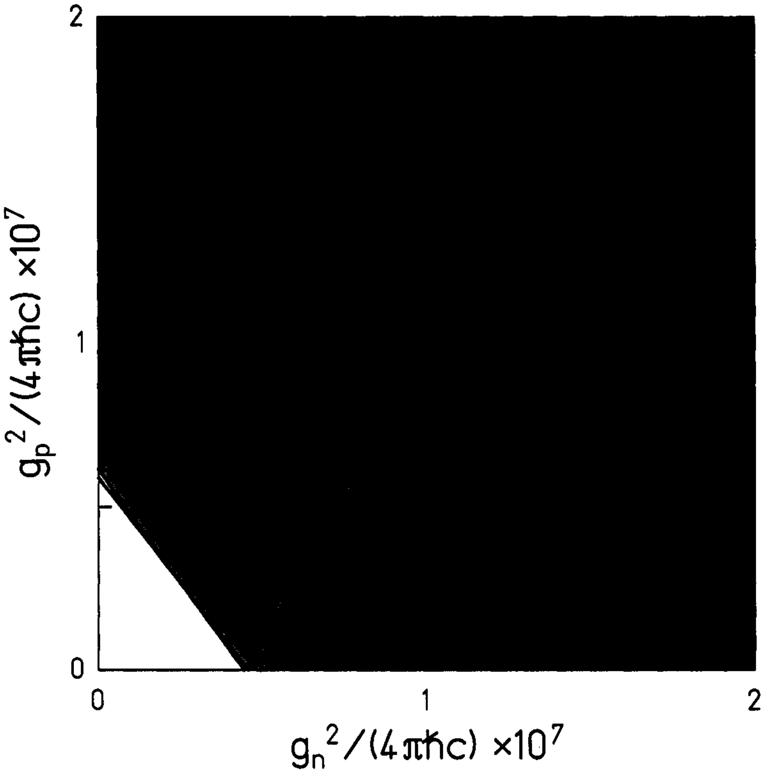

Figure 7.3: Our 68% confidence constraints on g_p^2 and g_n^2, the couplings of a massless pseduoscalar to protons and neutrons, respectively. The dashed line is the limit from Reference [1], the curved solid lines are from Reference [42], while the straight solid line is the limit from this work. There are atually two lines from this work, one assuming our attractor rings were both molybdenum and the other assuming both were tantalum; the lines are nearly indistinguishable. The excluded region is shaded.

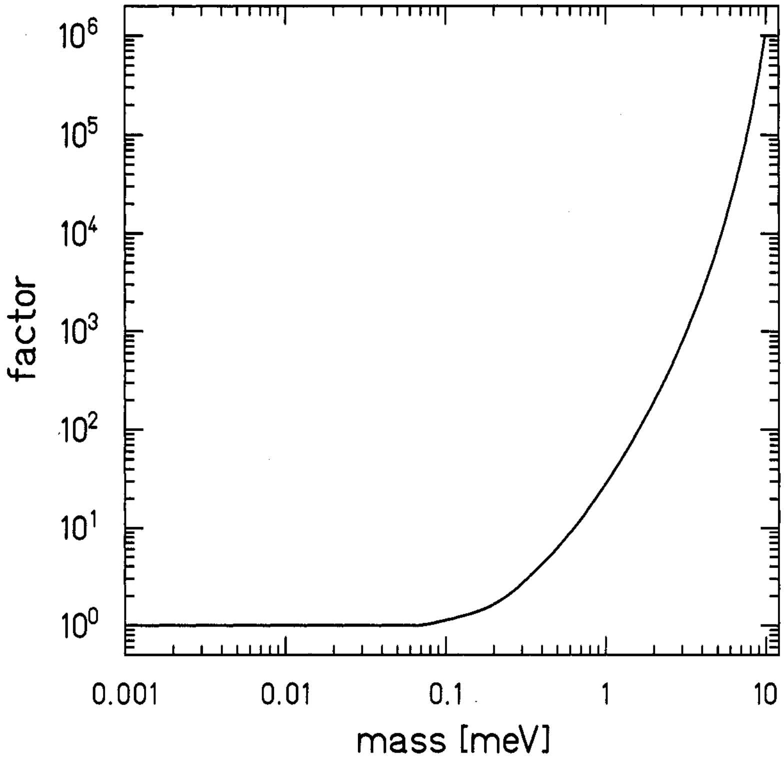

Figure 7.4: Factor by which the constraints of Figure 7.3 should be multiplied to obtain constraints on g_p^2 and g_n^2 for a massive pseudoscalar exchange plotted as a function of the pseudoscalar's mass.

7.3 Future Work

If this signal is from new physics, which we have not established here, our results are indeed interesting. Clearly, the next step is to test the nature of these results with further measurements. We plan to rerun this experiment, after making several improvements to our apparatus.

- New Torsion Fiber

  We have replaced our 20 μm diameter tungsten fiber with an 18 μm fiber. This simple change will improve our thermal torque noise by a factor of 1.3. It is unknown if or how this change will affect our increased noise at small separations.

- Detector Curvature

  As discussed in Section 5.3.4, our detector ring was curved by ≈ 25 μm. We believe that we have accounted for this curvature in this analysis, but as it was not part of our design, we attempted to improve upon it. We were able to reduce this curvature by carefully bending the ring, such that its lower surface varies $\leq \pm 4$ μm from its average value.

- Lower Attractor Thickness

  We designed our experiment such that the 21ω torque would be exactly zero at some accessible length scale; that is, the torque changed phase from in-phase with the lower attractor to in-phase with the upper attractor at some particular vertical separation. The true density of our lower attractor was higher than the nominal density we used in our design, and our 21ω torque was in-phase with the lower attractor at all separations. After this work was completetd, we have subsequently had the lower attractor lapped again, so that it is 140 μm thinner. This small change in thickness will change the cancelation of the two plates enough so that our 21ω torque does cross zero; the 21ω torque will have a different characteristic shape because of this change.

- Gap Measurement

In this experiment, we measured the gap between our attractor rings by measuring the two thicknesses with a handheld micrometer and measuring the combined thickness of the two rings once glued together. This measurement produced the unphysical result that the plates were spaced -0.8 ± 2.0 μm apart. After our data runs, we remeasured the linear dimensions of each of our rings on the Coordinate Measuring Machine (CMM); unfortunately, while attempting to measure the combined thickness of the two attractor rings, the glue between them gave way and we had to rely on our previous measurement. We have since abandoned the manual micrometer for the CMM for all measurements of this sort.

- Calibration Turntable Improvements

  For these measurements, our calibration turntable sat on the floor of our thermal enclosure. We moved the turntable manually, and read dial indicators to record its position. We have added a new bracket to support the turntable that attaches to the same cylcotron magnet yoke as the rest of our experiment. The cartesian axes of the turntable are now motorized and electronically indicated so that we can change the turntable position without opening our thermal enclosure.

We have completed each of these improvements and are set to repeat our measurement.

We are also planning a next-generation experiment with greater sensitivity that will be the thesis project of Ted Cook. The experiment described in this work used machining procedures of reasonable cost to produce parts that could be characterized and modeled at or near the micron level. We could conduct a more sensitive experiment merely by replacing our rings with denser material, but the uncertainties in our Newtonian model due to uncertainties in our characterization also grow with these densities. Our next generation experiment will reduce the Newtonian background so that we are less sensitive to uncertainties in the dimensions of our active masses. The Newtonian signal, because of its infinite range, decreases as the symmetry, m, of our active masses increases. An interaction whose range is $< 2\pi R/m$ where R is some characteristic radius of a ring, does not get washed out with a higher symmetry. Figure 7.5 shows a possible design for our next-generation

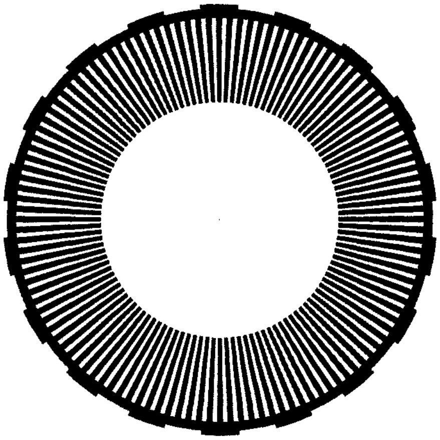

Figure 7.5: A top-view of the geometry for our next-generation design. The higher symmetry makes the design less sensitive to Newtonian gravity, while the long edges of the cutouts increase the sensitivity to a short-range interaction. the notches on the outer edge are less sensitive to a new-physics signal and will help search for systematic problems.

experiment.

BIBLIOGRAPHY

[1] C.D. Hoyle et al. Sub-Millimeter Tests of the Gravitational Inverse-Square Law. *Phys. Rev. D*, 70, 2004, hep-ph/0405262.

[2] C.L. Talmadge and E. Fischbach. *The Search for Non-Newtonian Gravity.* Springer Verlag, October 1998.

[3] E.G. Adelberger, B.R. Heckel, and A.E. Nelson. Tests of the Gravitational Inverse Square Law. *Annu. Rev. Nucl. Part. Physics*, 53, 2003, hep-ph/0307284.

[4] A.G. Riess et al. Observational Evidence from Supernovae for an Accelerating Universe and a Cosmological Constant. *Astron. J.*, 116, 1998, astro-ph/9805201.

[5] S. Perlmutter et al. Measurements of Ω and Λ from 42 High-Redshift Supernovae. *Astrophys. J.*, 517, 1999, astro-ph/9812133.

[6] C.L. Bennet et al. First Year Wilkinson Microwave Anisotropy Probe Observations:Preliminary Maps and Basic Results. *Astrophys. JS*, 148, 2003, astro-ph/0302207.

[7] N. Arkani-Hamed, S. Dimopoulos, and G. Dvali. The Hierarchy Problem and New Dimensions at a Millimeter. *Phys. Lett. B*, 429, 1998, hep-ph/9803315.

[8] DØCollaboration. Search for Large Extra Dimensions in the Monojet + Missing E_T Channel at DØ. *Phys. Rev. Lett.*, 90, 2003, hep-ex/0302014.

[9] L. Randall and R. Sundrum. A Large Mass Hierarchy from a Small Extra Dimension. *Phys. Rev. Lett*, 83, 1999, hep-ph/9905221.

[10] L. Randall and R. Sundrum. An Alternative to Compactification. *Phys. Rev. Lett*, 83, 1999, hep-th/9906064.

[11] S.M. Carroll. The Cosmological Constant. *Living Rev.Rel.*, 4 [Online Article], 2001, http://www.livingreviews.org/lrr-2001-1 and astro-ph/0004075.

[12] S.R. Beane. On the Importance of Testing Gravity at Distances Less than 1cm. *Gen.Rel.Grav.*, 29, 1997, hep-ph/9702419.

[13] R. Sundrum. Fat Gravitons, the Cosmological Constant, and Sub-Milllimeter Tests. *Phys.Rev. D*, 69, 2004, hep-th/0306106.

[14] I. Antoniadis, K. Benakli, A. Laugier, and T. Maillard. Brane to Bulk Supersymmetry Breaking and Radion Force at Micron Distances. *Nucl.Phys. B*, 662, 2003, hep-ph/0211409.

[15] S. Dimopoulos and G.F. Giudice. Macroscopic Forces From Supersymmetry. *Phys. Lett. B*, 379, 1993, hep-ph/9602350.

[16] S. Dimopoulos and A.A. Geraci. Probing Sub-Micron Forces by Interferometry of Bose-Einstein Condensed Atoms. *Phys. Rev. D*, 68, 2003, hep-ph/0306168.

[17] D.B. Kaplan and M.B. Wise. Couplings of a Light Dilaton and Violations of the Equivalence Principle. *JHEP*, 08, 2000, hep-ph/0008116.

[18] N. Arkani-Hamed, S. Dimopoulos, and G. Dvali. Phenomenology, Astrophysics and Cosmology of Theories with Sub-Millimeter Dimensions and TeV Scale Quantum Gravity. *Phys. Rev. D*, 59, 1999, hep-ph/9807344.

[19] E.G. Adelberger, E. Fischbach, D.E. Krause, and R.D. Newman. Constraining the Couplings of Massive Pseudoscalars Using Gravity and Optical Experiments. *Phys. Rev. D*, 68, 2003.

[20] M. Bordag, U. Mohideen, and V.M. Mostepanenko. New Developments in the Casimir Effect. *Phys. Rept.*, 353, 2001, quant-ph/0106045.

[21] T. Ederth. Template-Stripped Gold Surfaces with 0.4nm Roughness Suitable for Force Measurements : Application to the Casimir Force in the 20-100nm Range. *Phys. Rev. A*, 62, 2000, quant-ph/0008009.

[22] V.M. Mostepanenko and M. Novello. Constraints on Non-Newtonian Gravity from the Casimir Force Measurements Between Two Crossed Cylinders. *Phys. Rev. D*, 63, 2001, hep-ph/0101306.

[23] B.W. Harris, F. Chen, and U. Mohideen. Precision Measurement of the Casimir Force Using Gold Surfaces. *Phys. Rev. A*, 62, 2000, quant-ph/0005088.

[24] E. Fischbach, D.E. Krause, V.M. Mostapanenko, and M. Novello. New Constraints on Ultrashort-Ranged Yukawa Interactions from Atomic Force Microscopy. *Phys. Rev. D*, 64, 2001, hep-ph/0106331.

[25] S.K. Lamoreaux. Demonstration of the Casimir Force in the 0.6 to 6μm Range. *Phys. Rev. Lett.*, 78, 1997.

[26] J.C. Long, H.W. Chan, and J.C. Price. Experimental Status of Gravitational-Strength Forces in the Sub-Centimeter Regime. *Nucl. Phys. B*, 539, 1999, hep-ph/9805217.

[27] H. Abele, S. Baeßler, and A. Westphal. Quantum States of Neutrons in the Gravitational Field and Limits for Non-Newtonian Interaction in the Range Between 1μm and 10μm. *Lect. Notes Phys*, 631, 2003, hep-ph/0301145.

[28] J. Chiaverini, S.J. Smullin, A.A. Geraci, D.M. Weld, and A. Kapitulnik. New Experimental Constraints on Non-Newtonian Forces Below 100μm. *Phys. Rev. Lett.*, 90, 2003, hep-ph/0209325.

[29] J.C. Long, H.W. Chan, A.B. Churnside, E.A. Gulbis, M.C.M. Varney, and J.C. Price. New Experimental Limits on Macroscopic Forces Below 100 Microns. *Nature*, 421, 2003, hep-ph/0210004.

[30] J.K. Hoskins, R.D. Newman, R. Spero, and J. Schultz. Experimental Tests of the Gravitational Inverse-Square Law for Mass Separations from 2 to 105 cm. *Phys. Rev. D*, 32, 1985.

[31] V.P. Mitrofanov and O.I. Ponomareva. Experimental Test of Gravitation at Small Distances. *Sov. Phys. JETP*, 67, 1988.

[32] A. Cornaz, B. Hubler, and W. Kündig. Determination of the Gravitational Constant at an Effective Interaction Distance of 122m. *Phys. Rev. Lett*, 72, 1994.

[33] A.J. Romaides, R.W. Sands, E. Fischbach, and C.L. Talmadge. Final Results from the WABG Tower Gravity Experiment. *Phys. Rev. D*, 55, 1997.

[34] A. Shirata, T. Shiromizu, N. Yoshida, and Y. Suto. Galaxy Clustering Constraints on Deviations from Newtonian Gravity at Cosmological Scales. *Phys. Rev. D*, 71, 2005; astro-ph/0501366.

[35] C.D. Hoyle. *Sub-Millimeter Tests of the Gravitational Inverse-Square Law.* PhD thesis, University of Washington, 2001.

[36] C. D'Urso and E.G. Adelberger. Translation of Multipoles for a 1/r Potential. *Phys. Rev. D*, 55, 1997.

[37] L. Carbone, A. Cavalleri, R. Dolesi, C.D. Hoyle, M. Hueller, S. Vitale, and W.J. Weber. Upper Limits on Stray Force Noise for LISA. *Class. Quantum Grav.*, 21, 2004.

[38] Z.-K. Hu, J. Luo, and H. Hsu. Nonlinearity of Tungsten Fiber in the Time-of-Swing Method. *Phys. Lett. A*, 264, 1999.

[39] W.H. Press, S.A. Teukolsky, W.T. Vetterling, and B.P. Flannery. *Numerical Recipes in C.* Cambridge University Press, 1996.

[40] H.B. Callen and R.F. Greene. On a Theorem of Irreverisble Thermodynamics. *Phys. Rev.*, 86, 1952.

[41] P.R. Saulson. Thermal Noise in Mechanical Experiments. *Phys. Rev. D*, 42, 1990.

[42] G.L. Smith et. al. Short-Range Tests of the Equivalence Principle. *Phys. Rev. D*, 61, 1999.

[43] L.H. Ford. Spectrum of the Casimir Effect and the Lifshitz Theory. *Phys. Rev. A*, 48, 1993.

[44] T. Varpula and T. Poutanen. Magnetic Field Flucutations Arising from Thermal Motion of Electric Charge in Conductors. *J. Appl. Phys.*, 55, 1984.

VITA

Dan Kapner was born in Valparaiso, Indiana on May 2, 1976 and grew up outside of Memphis, TN. He graduated from Cornell University with a B.A. in Physics in May, 1998. He began work with the Eöt-Wash Gravity group in July, 1999 and entered the University of Washington Ph.D. program in September of that same year.